Implementation and Calibration of a $k_\perp$ Jet Finding Algorithm For Use in $p\bar{p}$ Collisions at $\sqrt{s} = 1.8$ TeV at the DØ Collider Detector

By

Katherine Chiyoko Frame

A DISSERTATION

Submitted to
Michigan State University
in partial fulfillment of the requirements
for the degree of

DOCTOR OF PHILOSOPHY

Department of Physics and Astronomy

1999

ABSTRACT

Implementation and Calibration of a $k_\perp$ Jet Finding Algorithm For Use in $p\bar{p}$ Collisions at $\sqrt{s} = 1.8$ TeV

By

Katherine Chiyoko Frame

Jets are widely used as probes of the fundamental parton collisions in Quantum Chromodynamics. Jets, which are believed to represent the energies and directions of the emerging partons, are viewed by the experimenter as collimated distributions of hadrons. The momenta and angles of these hadrons must be combined to form the parent jet. Because of measurement resolutions and the unavoidable presence of backgrounds, a jet is thus dependent on the precise nature of the combination algorithm. This thesis studies a new type of jet algorithm and, in particular, investigates its dependence on the energy and pseudorapidity scales of the DØ detector.

For my parents, Eleanor O. Frame and William V. Frame.

ACKNOWLEDGEMENTS

It is with great pleasure that I take this opportunity to acknowledge some of the people who have contributed to this work. I owe most of my understanding of the current theory to C.-P. Yuan. His patience in explaining very complex ideas to me has been exemplary. I have also learned a great deal in conversations with Mike Seymour, Walter Giele and James Stirling. I would also like to thank all the individuals and institutions involved in the building and running of the DØ experiment. The QCD and $k_\perp$ groups at DØ have provided much feedback and constructive criticism. In particular, I thank Rob Snihur and Daniel Elvira. A special thanks is needed for Rich Astur and Bernard Pope. Rich took me under his wing in my early days at DØ and Bernard has been like a second advisor to me. I am extremely fortunate to have had the benefit of their guidance and support.

I would like to take a moment to acknowledge those who have influenced me outside of the academic arena. First and foremost, I thank my family for their love and support throughout my life. Joanna Guttmann, Linda Tartof and Shojiro Sugiyama taught me the virtues of commitment and discipline. My friendships with Todd Cruz, Lenny Apanasevich, Elizabeth Haywood, Ken Johns and Sal Fahey have brought me much laughter and joy, and I have learned much of human virtue by their examples. Elizabeth Gallas provided an infinite wealth of wisdom and advice for which I am extremely grateful. I have also had the good fortune to have befriended

Steve Jerger, Tom Rockwell, Joelle Murray, Mike Wiest, Dan Owen, Gian Diloreto, Tina Hebert, Florencia Cannelli, and Lisa Oravecs. I would also like to thank the guys at the Fermilab gym who taught me how to play basketball (especially the members of the gray team) and lift weights: Rick Jesik, Ryan Hagler, Noah Wallace, Carl Penson, Walsh Brown, Chet Shaw, Ben Fonseca, Ray Fonseca and Wayne Waldon.

Most Importantly, I must thank my advisor, Harry Weerts. His strong sense of honor and duty is inspirational. He has been an unending source of guidance, patience and wisdom throughout the years. None of this work would have been possible without his hand. Thank you, Harry.

Contents

1 Introduction **1**

1.1 Fundamental Constituents of Matter 1

1.2 The Thesis 7

2 The Standard Model **9**

2.1 Electroweak Interactions 11

2.2 Quantum Chromodynamics 15

2.3 The Running of the Couplings 16

2.4 Cross Sections 18

2.5 Renormalization and the Strong Coupling, α_s 21

3 Jet Production in $p\bar{p}$ Collisions **25**

3.1 $p\bar{p}$ Collisions 26

3.2 $p\bar{p}$ Event Variables 29

3.3 Monte Carlo Event Generators 30

3.4 Jets 33

3.5 R_{32} 34

4 The Tevatron and The DØ Detector **37**

4.1 The Fermilab Tevatron Collider 37

4.2 The DØ Detector 40

4.2.1 The Level Zero Detector 41

4.2.2 The Tracking System 43

4.2.3 The Calorimeter 44

4.2.4 The Muon Spectrometer 48

4.2.5 The DØ Trigger System 49

4.2.6 Offline Reconstruction 50

5 The $k_\perp$ and Cone Jet Algorithms **52**

5.1 The Fixed Cone Jet Algorithm 54

5.2 Clustering Algorithms for e^+e^-Collisions 58

5.3 Adaptation of the $k_\perp$ Algorithm for $p\bar{p}$ Collisions 60

5.4 $k_\perp$ Jets at DØ 62

5.4.1 Monte Carlo Event Jet Rates 66

6 Introduction to $k_\perp$ Jet Momentum Calibration **69**

6.1 General Overview of $k_\perp$ Jet Momentum Calibration 70

7 $k_\perp$ Jet Offset Correction 72

7.1 Monte Carlo Data With Overlay 74

7.2 The Method 75

7.3 Verification of the Overlay Method 79

7.4 Offsets for the $k_\perp$ Algorithm 83

7.4.1 Offset Due to Noise, Pile-Up and Multiple Interactions 83

7.4.2 Offset Due to Physics Underlying Event 89

8 $k_\perp$ Jet Response Correction 96

8.1 The Missing E_T Projection Fraction Method 97

8.1.1 The Energy Estimator, E' 99

8.2 γ-Jet Data 100

8.2.1 Photon Event Requirements 100

8.2.2 Cone Jet Requirements 102

8.2.3 Additional considerations for $k_\perp$ Jets 103

8.3 Cryostat Factor Correction 104

8.4 $E' \rightarrow P_{kt}$ Mapping 105

8.5 Response vs. P_{kt} 107

8.6 ICR Correction 110

8.7 Jet-Jet Data . . . 110

8.7.1 Measurement of F_η . . . 113

8.8 The Low E_T Bias . . . 120

8.9 Low P_{kt} Jet Response . . . 121

8.10 The Jet Response Errors . . . 126

8.10.1 Errors and Correlations of the R_{jet} Fit . . . 126

8.10.2 Low Momentum Errors . . . 127

8.10.3 η Dependent Correction Errors . . . 129

9 $K_\perp$ Jet MPF Closure **133**

9.1 The Data . . . 134

9.2 Monte Carlo Jet Corrections . . . 134

9.2.1 Monte Carlo Underlying Event Offset . . . 134

9.3 Monte Carlo Jet Response . . . 135

9.3.1 Monte Carlo Cryostat Factor . . . 135

9.3.2 Jet Response vs. $k_\perp$ Jet Momentum . . . 137

9.4 Monte Carlo Closure . . . 137

10 $k_\perp$ Momentum Calibration Summary **144**

10.1 Summary Plots of Corrections and Errors . . . 146

11 R_{32} Preliminary Results **152**

A Photon and Jet Triggers **154**

A.1 Photon Triggers 154

A.2 Jet Triggers 156

B Cone Jet Offset Comparison **159**

B.1 Smeared Versus Unsmeared Quantities 160

B.2 Dependence of the Offset on E_T 165

B.3 Dependence of the Offset on Luminosity 171

C Showering Effects on the Jet Response **172**

List of Tables

2.1 The Standard Model Quarks. 9

2.2 The Standard Model Leptons. 10

2.3 The Standard Model Vector Bosons and their respective forces. 10

2.4 The Scalar Higgs Boson. 10

2.5 Summary of α_s measurements [15]. 23

7.1 Availability of E_T , luminosity and η for overlayed Monte Carlo data. 75

8.1 Cryostat corrections applied to the energy in the calorimeter cryostats introduced for the DØFIX environment. 104

8.2 Fit parameters for E' to P_{kt} mapping. 107

8.3 Fit parameters for hadronic response correction. 110

8.4 Triggers and thresholds 112

8.5 Correlation matrix for error band in hadronic jet response correction for $k_\perp$ jets. 129

8.6 Residuals 130

9.1 Herwig v5.9 underlying event energy density. 135

9.2 Fit parameters for R_{jet} vs. P_{kt} in Monte Carlo data. 137

A.1 Triggers used in the photon event selection. 155

A.2 Triggers used in jet event selection. 157

List of Figures

2.1 Feynman diagram for $e^- u \to \nu_e d$ by W exchange 14

2.2 Feynman loop diagrams 17

2.3 Factorization of the $p\bar{p}$ matrix element. 20

2.4 Feynman diagrams for qg→qg via gluon exchange 21

2.5 Summary of α_s measurements. 24

3.1 Feynman diagram for $qg \to qg$ by gluon exchange. 27

3.2 $qg \to qg$ (before). 27

3.3 $qg \to qg$ (after). 28

3.4 An event as seen by the DØ detector. 29

3.5 An example of $\mathcal{O}(\alpha_s^3)$ Feynman diagram contributions 32

4.1 Overview of the Fermilab Tevatron. 38

4.2 Cutaway view of the DØ detector. 42

4.3 The four detectors which comprise the tracking system. 43

4.4 Cutaway view of the DØ calorimeter detector. 45

4.5 Schematic view of a liquid argon readout cell. 46

4.6 One quadrant of the DØ calorimeter. 47

4.7 Block diagram of the DØ trigger system. 49

5.1 Lego plot of a 2 jet event 53

5.2 Fixed cone jet. 54

5.3 $k_\perp$ jet clustering. 57

5.4 Jet Clustering in e^+e^-Collisions 59

5.5 $k_\perp$ Jet Rates as a function of f_{cut} in Herwig v5.8 Monte Carlo Data. . 68

7.1 Separation of overlayed and non-overlayed $k_\perp$ jets. 77

7.2 E_T differences between noise overlayed and non-overlayed $k_\perp$ jets. . . 77

7.3 Ranking of overlayed $k_\perp$ jets compared matched to non-overlayed jets. 78

7.4 Distribution of reconstructed E_T for $k_\perp$ jets without noise overlay. . . 79

7.5 0.7 cone jet occupancy vs. jet η for jets found in minimum bias data. 80

7.6 0.7 cone jet occupancy vs. jet η for jets found in Monte Carlo with minimum bias overlay data. 81

7.7 Measured O_{zb} vs. $k_\perp$ jet E_T at $\mathcal{L}$=0.1×10^{30}cm^{-2}sec^{-1}. 84

7.8 Measured O_{zb} vs. $k_\perp$ jet E_T at $\mathcal{L}$=5×10^{30}cm^{-2}sec^{-1}. 85

7.9 Measured O_{zb} vs. $k_\perp$ jet η at various luminosities. 86

7.10 Measured O_{zb} vs. $k_\perp$ jet η at $\mathcal{L}$=5 and 30<E_T <50 GeV. 87

7.11 Parametrization of O_{zb} vs. $k_\perp$ jet η for jets with 30<E_T <50 GeV, for various luminosities. 88

7.12 O_{zb} correction vs. $k_\perp$ jet E_T 90

7.13 O_{zb} correction vs. $k_\perp$ jet η 91

7.14 Measured O_{ue} vs $k_\perp$ jet E_T 92

7.15 Measured O_{ue} vs $k_\perp$ jet η 94

7.16 O_{ue} correction vs $k_\perp$ jet η. 95

8.1 Response versus E'. Open symbols are from the full γ-jet data sample and solid symbols are from the smaller sample reconstructed with $k_\perp$ jets. The additional DØFIX cryostat corrections were removed from $k_\perp$ jets. 106

8.2 $k_\perp$ jet P versus E'. Straight lines were fit to the CC and EC separately.108

8.3 Response versus P_{kt} 109

8.4 Response fit versus jet P_{kt}. $R_{jet}(P_{kt}) = a + b \cdot \ln(P_{kt}) + c \cdot \ln(P)^2$. . . 111

8.5 Response versus η >0.0 for jet-jet data. 114

8.6 Response versus η <0.0 for jet-jet data. 115

8.7 Correction factor F_η 116

8.8 Correction factor F_η 117

8.9 Response versus η after η dependent corrections. 118

8.10 Response fit versus jet E with and without the ICR correction. $R_{jet}(E) = a + b \cdot \ln(E) + c \cdot \ln(E)^2$. The two curves are virtually identical. . . . 119

8.11 $\Delta\phi_{\gamma\ jet}$ distribution 122

8.12 Et distribution of first 4 objects 123

8.13 Low momentum jet response 125

8.14 Error correlations for $k_\perp$ jet response fit. 128

8.15 The fractional difference between R_{meas} and R_{calc} for partially corrected jets. $\Delta R = (R_{meas} - R_{calc}) \ / \ R_{calc}$. 131

8.16 The distributions of fractional differences between R_{meas} and R_{calc}. . 132

9.1 Monte Carlo Cryostat Factor 136

9.2 R_{jet} vs. P_{kt}in Monte Carlo data. 138

9.3 Monte Carlo Closure in CC 140

9.4 Monte Carlo Closure in EC 141

9.5 Monte Carlo Closure in EC 142

9.6 $k_\perp$ algorithm dependent correction, R_{kt}. Errors are shown as dotted lines. 143

10.1 Corrections and Errors for η_{Ktjet} =0.0, $\mathcal{R}$ =0.7. 147

10.2 Corrections and Errors for η_{Ktjet} =1.2. 148

10.3 Corrections and Errors for η_{Ktjet} =2.0. 149

10.4 Corrections and Errors versus η_{Ktjet}, Jet $P_T = 20$ GeV. 150

10.5 Corrections and Errors versus η_{Ktjet}, Jet $P_T = 100$ GeV, $R_{cone} = 0.7$. 151

11.1 R_{32}, vs. H_{T3} 153

B.1 The 0.7 cone jet offset density, D_{zb}, as obtained by selecting the leading jets either in the $z5$ (full boxes) or in the xx sample (full circles). The open circles are from CAFIX 5.1. 161

B.2 Unsmeared D_{zb} offset vs. E_T in five η ranges for 0.7 cone jets. The cut in E_T is applied either to the raw xx jets (stars), or to $z5$ jets (full circles) weighed to a flat distribution in E_T . The result from CAFIX5.1 (open box) is shown for comparison on the left, but no E_T is associated with it. 163

B.3 The smeared (open circles) and unsmeared (full circles) D_{zb} offset for 0.7 cone jets. Both sets of points differ only by the weight assigned to the generated jets. The open box shows for reference the result from the JES D0Note. 164

B.4 Dependence of D_{ue} on E_T for cone jets. The result from CAFIX5.1 is shown for reference 166

B.5 Jet energy dependence of occupancy for zero bias luminosity 5 and $R = 0.7$ cone jets. 167

B.6 Dependence of $m0$-xx on E_T for cone jets 169

B.7 Dependence of zb-xx on E_T for cone jets. The dependence is the same as in the previous figure, and cancels when getting D_{ue} by taking the difference 170

B.8 The unsmeared offset D_{zb} (stars) at different luminosities for $30<E_T<50$ Gev jets (our result depends on jet energy). Full circles are from CAFIX5.1, for comparison. 171

C.1 Showering effects in the MPF method. (a) A photon is balanced by three particles, 1, 2, and 3, in the transverse plane. $E_1 > E_2, E_3$ and $R_1 > R_2, R_3$. (b) The 2nd and 3rd particles are deflected away from the jet axis in the calorimeter. 173

"When the objects of an inquiry, in any department, have principles, conditions, or elements, it is through acquaintance with these that knowledge, that is to say scientific knowledge, is attained. For we do not think that we know a thing until we are acquainted with its primary conditions or first principles, and have carried our analysis as far as its simplest elements. Plainly therefore in the science of Nature, as in other branches of study, our first task will be to try to determine what relates to its principles."

Aristotle's *Physics*

Chapter 1

Introduction

Throughout our history and in our individual lives, humans have endeavored to attain some understanding of the human condition. Academic institutions are divided into disciplines which focus on various aspects of this. Since we inhabit a physical universe and are physical beings ourselves, it follows that we have the various branches of physical science. In particular, Elementary Particle Physics is the study of the fundamental building blocks of matter and the forces which govern their behavior.

At present, four forces are believed to dictate all physical interactions: gravity, electromagnetism, the weak force and the strong force. The current Standard Model theory encompasses all but gravity.

1.1 Fundamental Constituents of Matter

In Aristotle's day, all matter was believed to be made up of four elements: earth, wind, fire and water. In Medieval times, a few of the Chemical elements were recog-

nized. By the 19th century, about 30 chemical elements were identified and it was discovered that the combinations of these elements could account for the profuse number of chemical compounds found in nature. In the early 1800's, John Dalton proposed that the chemical elements are composed of units (atoms) of matter which could be characterized by their weight.

Throughout most of the 1800's, the atom was considered to be the fundamental unit of matter. By the turn of the century, the electron had been discovered and believed to be an essential part of atomic structure, but classical theories proved inadequate to describe this structure. In 1900, Max Planck introduced the idea of quantized radiation and quantum theory was born [1, 2].

The years that followed saw huge advances in both theoretical and experimental physics. In 1905, Albert Einstein put forth his theory of special relativity and proposed a quantum of light behaving like a particle [4] (later to be named *photon*). This was received with much skepticism, but in 1916, Millikan published his results on the photoelectric effect confirming Einstein's photon theory [5]. Doubt still lingered, but in 1923, Compton observed shifts in wavelengths in light scattering experiments which could only be explained using a photon theory of light. In the same spirit, de Broglie considered the possibility that if something previously thought to have only wave attributes could also behave as a particle, than perhaps particles could behave like waves. Shortly after Compton's experiments, de Broglie proposed the wave property of matter and a couple of years later Schroedinger developed wave mechanics for describing quantum systems for bosons.

Meanwhile, physicists were also making progress in their understanding of atomic

structure. Hans Geiger and Ernest Marsden (under the supervision of Ernest Rutherford), performed experiments in 1909 scattering alpha particles off a gold foil. The large scattering angles they observed suggested a small, dense, positively charged nucleus in atoms. It wasn't until a decade later that Rutherford was able to find the first evidence of the existence of the proton. In 1913, Niels Bohr constructed a quantum theory of atomic structure, and then, several years later, in 1925, Pauli formulated the exclusion principle for electrons in atoms.

In 1930, there were believed to be three elementary particles: photons, electrons and protons. However, theoretical and experimental developments implied otherwise, and the next few decades proved to be one of the most exciting periods in particle physics history. A plethora of new particles were predicted and/or experimentally observed and some of the most fundamental building blocks of the current Standard Model theory were established, namely, the Dirac equation and the theories of weak and strong interactions.

In 1928, Dirac was able to describe electrons combining quantum mechanics and special relativity. After a few years, he realized that his equation implied the existence of a new particle that is identical to the electron except that it is positively charged. He called it a *positron*. No one had ever conceived of an antiparticle before and this turned out to be an important discovery. The positron was later experimentally observed in cosmic ray experiments in 1932.

The continuous energy spectrum seen in beta decay experiments in the late 1920's led Pauli to suggest that an additional particle, a neutrino, carried away the missing energy. Following that, Fermi introduced the weak interaction to describe beta decay

using Pauli's neutrinos. This was another notable moment in our history because this was the first theory to imply particle flavor changes (e.g. neutron changing to a proton plus electron plus neutrino).

The road to our current understanding of strong interactions was not so smooth. In 1931, Chadwick discovered the neutron, but as more was learned about nuclear structure, the mechanisms of nuclear binding became more obscure. Around 1934, Yukawa put forth a theory combining relativity and quantum theory to describe the strong interactions in the nucleus. He introduced a mediator particle called the *pion* and estimated its mass to be about 200 times that of the electron. In 1937, a particle with approximately this mass was discovered in cosmic ray experiments. Of course, it was thought to be the pion, but it was much later (1946) that it was actually discovered to be a *muon*. The muon was quite unexpected as it is the first time a second generation of matter was observed, and the famous phrase was uttered, "Who ordered that?" (by I. I. Rabi). Soon after the muon was revealed, however, the pion was also observed in cosmic rays.

In the following decade, a proliferation of particles was observed, and in electron-nuclei scattering experiments in the mid 1950's, a charge density distribution was seen in protons and neutrons suggesting an internal structure to nucleons. In 1964, Gell-Mann and Zweig theorized the existence of three elementary particles called *quarks* [6, 7]. The up, down and strange quarks are fermions with charges of $+\frac{2}{3}$, $-\frac{1}{3}$ and $-\frac{1}{3}$ respectively. Many new particles could be described as combinations of these quarks. For example, the proton is composed of two up quarks and one down quark and the neutron is composed of two down quarks and one up quark. The third

quark, strange, was used to build some of the more exotic particles.

In experiments at the Stanford Linear Accelerator Center (SLAC) in the late 1960's, electrons scattered off protons appeared to be bouncing off of hard cores inside protons. Bjorken and Feynman used a constituent particle model to interpret the data [3]. Although they did not refer to the constituent particles as quarks (but as partons), this provided supporting evidence that the proton is a composite particle and supported the quark theory.

Meanwhile, Schwinger, Bludman and Glashow independently came up with the idea that the weak interactions are mediated by charged heavy particles (later named the W^+ and W^-), and in 1967, Weinberg and Salam (again independently) developed a theory that unified the electromagnetic and weak interactions. They suggested the existence of a neutrally charged vector boson, Z^0, which (in addition to the W^+, W^-) acts as a mediator of weak interactions. In an effort to explain the masses of the vector bosons, they also introduced a massive scalar boson called the Higgs, H. The W^+, W^-, and Z^0 bosons were all observed in 1983, but the Higgs has yet to be observed and remains a major missing piece of the current theory.

At this point, the current electroweak theory was pretty well developed, but the theory describing strong interactions needed some modification. Because the leptons appeared in pairs, e and ν_e and μ and ν_μ, it was theorized that the quarks would behave in a similar manner and the charm quark ($+\frac{2}{3}$ charge) was introduced to be paired with the strange (the other pair being the up and down). Fritzsch and Gell-Mann put forth the theory of quantum chromodynamics (QCD). This theory is similar to electroweak theory. Where electroweak has the photon, $W^\pm$ and Z^0

as its mediators, QCD has the gluons. Evidence for gluons was first experimentally observed in 1979 in electron positron collisions.

In 1974, the J/Ψ was discovered at Brookhaven/SLAC by Ting/Richter [8, 9]. The J/Ψ is composed of a charm and an anti-charm. The addition of the charm quark implied the existence of a group of new particles which were subsequently observed. The charm quark, itself, was observed in 1976.

With the success of the 2 generation theory, the possibilities of there existing a third generation of quarks and leptons was theorized, and, sure enough, the Tau lepton was discovered in 1976 at SLAC and the bottom and top quarks were observed at Fermilab in 1977 and in 1995 respectively [10].

Today, the tau neutrino, ν_τ, and the Higgs boson, H, are the only particles of the Standard Model theory that have not been experimentally observed. Strong evidence for the existence of the Tau neutrino exists while the Higgs remains somewhat more elusive.

For the past 20 years the Standard Model theory has proven itself to be remarkably stable. No experimental measurement to date contradicts it. However, the theory is not complete for it cannot account for the masses of the fermions and it does not accommodate gravity. It is defined by 18 parameters making it somewhat unwieldy, and only the electromagnetic and weak interactions are unified. Several theoretical models are being developed with a view toward completeness and unification of the 4 forces, electromagnetic, weak, strong and gravitational.

As mentioned above, the parameters of the Standard Model theory are not com-

pletely nailed down. Perhaps, as our measurements become more precise and we are able explore regions of phase space previously unavailable, we will see phenomena inconsistent with the current theory and this will guide us in a new direction.

1.2 The Thesis

Most of today's particle physics experiments are similar in principle to Rutherford's experiment scattering alpha particles off of a gold foil. Particles are collided at high energies (either using two colliding beams or a beam focused on a fixed target) and the interactions are studied by examining the outcome.

This thesis involves data from an experiment in which protons and antiprotons are collided at extremely high energies. The high energy is needed in order to study the constituent quarks and gluons that make up the proton and antiproton. When the pair collide, typically, 2 or 3 *jets* of particles emerge and are detected. Whether there are 2 or 3 jets detected is closely related to the strength of the strong interaction. The original intent of this thesis was to perform a measurement of the ratio of events with 3 jets to 2 jets, R_{32}. This would give us a better understanding of the nature of the strong force. We are able to look at interactions with center of mass energies much higher than what has previously been looked at.

To make an experimental measurement of R_{32}, a tool had to be developed and calibrated. This task, while meritorious in itself, has diverted much effort away from the intended measurement and, therefore, that analysis is left outstanding. What is presented here is the work done developing and calibrating the $k_\perp$ jet algorithm

along with some very preliminary results for our measurement of R_{32}.

The thesis is organized in the following way. In the following chapter, we give a brief overview of the Standard Model theory. Following that, we describe jet production in $p\bar{p}$, physics and motivate the measurement of R_{32}. Chapter 4 contains a description of the experimental apparatus, and in Chapter 5, we will discuss jet finding algorithms. The momentum calibration of jets in the detector is a considerable task requiring much attention, and, therefore, five Chapters are devoted to its derivation, testing, and summary. Finally, we will present a very preliminary measurement of R_{32}.

Chapter 2

The Standard Model

The particles of the Standard Model theory can be categorized into 4 groups: quarks (Table 2.1), leptons (Table 2.2), vector bosons (Table 2.3) and the Higgs scalar boson (Table 2.4). Quarks and leptons are fermions (spin 1/2 particles) and, within these groups, there are 3 generations. The three generations are identical except for their masses. Most matter is comprised of the first (lightest) generations (up and down quarks and electrons).

As stated previously, all matter interacts via four forces (gravity, electromag-

Table 2.1: The Standard Model Quarks.

	Charge	**Mass** (MeV/c^2)
up	$\frac{2}{3}$	1.5 - 5
down	$-\frac{1}{3}$	3 - 9
charm	$\frac{2}{3}$	1,100-1,400
strange	$-\frac{1}{3}$	60-170
top	$\frac{2}{3}$	174,300 $\pm$ 5,100
bottom	$-\frac{1}{3}$	4,100-4,400

Table 2.2: The Standard Model Leptons.

	Charge	**Mass** (MeV/c^2)
e^-	-1	0.511
ν_e	0	$< 5.1 \times 10^{-6}$
μ^-	-1	106
ν_μ	0	< 0.27
τ	-1	1,777
ν_τ	0	< 31

Table 2.3: The Standard Model Vector Bosons and their respective forces.

	Force	**Charge**	**Mass** (MeV/c^2)
γ	Electromagnetic	0	0
gluon	Strong	0	0
$W^\pm$	Weak	± 1	80000
Z^0	Weak	0	91000

Table 2.4: The Scalar Higgs Boson.

	Charge	**Mass** (MeV/c^2)
H	0	> 58400 [15]

netism, the weak force and the strong force). The current Standard Model theory encompasses all but gravity. In the Standard Model theory, interactions are described in the framework of the U(1)×SU(2)$_L$×SU(3) gauge group. The electromagnetic and weak forces are unified in the electroweak gauge, U(1)×SU(2)$_L$, and the strong force is described under SU(3). The forces are mediated by the exchange of the vector bosons corresponding to the symmetries of the group as shown in Table 2.3. One scalar Higgs boson, H, is predicted (shown in Table 2.4). Its existence is not yet confirmed, but it is necessary to account for the masses of the $W^{\pm}$ and Z^0 vector bosons in the present theory.

What is presented here is a very minimal view of the Standard Model theory. For a more rigorous description the reader is directed to the references, [16, 17, 18, 19, 20, 21].

2.1 Electroweak Interactions

The electromagnetic and weak interactions are unified in the Standard Model under the gauge group, U(1)×SU(2)$_L$. U(1) symmetry implies conservation of hypercharge, Y, and under SU(2)$_L$, isospin, T, is conserved. Electric charge, Q, is related to these by $Q = T_3 + \frac{Y}{2}$ where T_3 is the third component of isospin. Therefore, Q is also conserved in the electroweak gauge. The subscript, L, denotes that the SU(2) group acts only upon the left handed component of the field. No right handed neutrinos have been observed. The group acts on left handed doublets and right handed

singlets. The lepton doublets and singlets are written as

$$\begin{pmatrix} \nu_e \\ e \end{pmatrix}_L , \begin{pmatrix} \nu_\mu \\ \mu \end{pmatrix}_L , \begin{pmatrix} \nu_\tau \\ \tau \end{pmatrix}_L , e_R,\ \mu_R,\ \tau_R\ .$$

The quark doublets and singlets are

$$\begin{pmatrix} u \\ d' \end{pmatrix}_L , \begin{pmatrix} c \\ s' \end{pmatrix}_L , \begin{pmatrix} t \\ b' \end{pmatrix}_L , u_R,\ c_R,\ t_R,\ d_R,\ s_R,\ b_R\ .$$

The bottom components of the quark doublets are different from the mass eigenstates in Table 2.1. They can be written as linear combinations of the mass eigenstates using the CKM matrix (named after Cabibbo, Kobayashi, and Maskawa):

$$\begin{pmatrix} d' \\ s' \\ b' \end{pmatrix} = \begin{pmatrix} V_{ud}V_{cd}V_{td} \\ V_{us}V_{cs}V_{ts} \\ V_{ub}V_{cb}V_{tb} \end{pmatrix} \begin{pmatrix} d \\ s \\ b \end{pmatrix} .$$

This gives us some mixing between the different quark generations (e.g. the up quark can couple to the strange and bottom quarks as well as the down quark). The couplings between the different quark generations are rare and, therefore, the off diagonal CKM matrix elements are $<< 1$.

In the vacuum (ground state), the U(1)×SU(2)$_L$ Lagrangian requires the four gauge bosons to be massless. The symmetry of the ground state must be spontaneously broken to account for the masses of the W^+, W^- and Z^0 bosons. This is done through the Higgs mechanism. The result is the scalar Higgs boson and in addition to mass, the W and Z bosons gain a longitudinal polarization component.

The masses of the mediators and the strength of the interactions are determined by 3 fundamental parameters: the weak isospin coupling, g_w, hypercharge coupling, g', and the vacuum expectation value for spontaneous symmetry breaking, ν. They are given by the following relations:

$$g_w = \frac{e}{\sin\theta_W} \ , \tag{2.1}$$

$$g' = \frac{e}{\cos\theta_W} \ , \tag{2.2}$$

and

$$\nu = \frac{2M_W}{g_w} \ , \tag{2.3}$$

where e is the magnitude of the charge of the electron, M_W is the mass of the $W^{\pm}$ and θ_W is the weak mixing angle. It is often convenient to express these in terms of 3 other variables: the fine structure constant, α_{em}, the Fermi constant, G_F, and $\sin^2\theta_W$. α_{em} and G_F are related to g_w, g', and ν by

$$\alpha_{em} = \frac{e^2}{4\pi} = \frac{1}{4\pi}\left(\frac{1}{\frac{1}{g_w^2}+\frac{1}{g'^2}}\right) \ , \tag{2.4}$$

and

$$G_F = \frac{1}{\sqrt{2}\nu^2} = \frac{g_w^2}{4\sqrt{2}M_W^2} \ . \tag{2.5}$$

$\sin^2\theta_W$ is given by the masses of the W, M_W, and Z^0, M_Z, by

$$\sin^2\theta_W = 1 - \frac{M_W^2}{M_Z^2} \ . \tag{2.6}$$

Current experimentally measured values for α_{em}, G_F, M_W and M_Z are

$$\alpha_{em}(m_e) = \frac{1}{137.0359895} \ , \tag{2.7}$$

$$G_F = 1.16639 \times 10^{-5} GeV^{-2} \ , \tag{2.8}$$

$$M_W = 80.410 \pm 0.044 \ GeV/c^2 \quad and \quad M_Z = 91.187 \pm 0.007 \ GeV/c^2 \ . \tag{2.9}$$

An example of a weak interaction is illustrated using a Feynman diagram in Figure 2.1a in which an electron and an up quark exchange a W boson resulting in an electron neutrino and a down quark. In Feynman diagrams, time runs horizontally with some space coordinate on the vertical axis. By convention, fermions are depicted by a solid line with an arrow pointing in the forward direction of time. An arrow pointing in the reverse direction indicates an antiparticle. A dashed line is drawn for W (and Z) bosons. In succeeding diagrams, photons are represented by a wavy line and gluons by a helix as shown in 2.1(b).

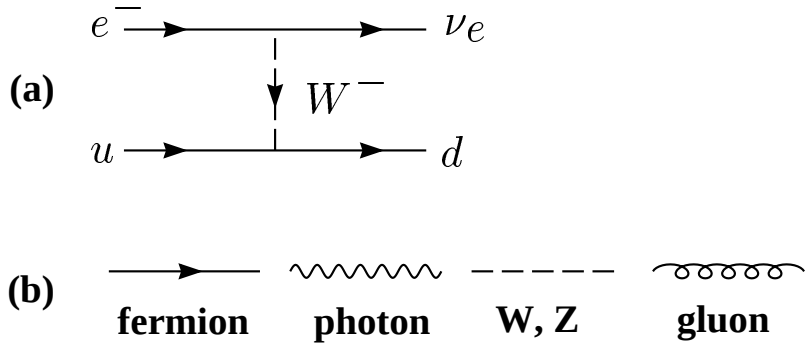

Figure 2.1: (a) Feynman diagram for $e^- u \to \nu_e d$ by W exchange. Time flows from left to right. (b) Fermions are depicted by a solid line with an arrow pointing in the forward direction of time (an arrow in the reverse direction denotes an antiparticle). Photons are represented by a wavy line, W and Z bosons by a dashed line, and gluons by a helix.

The Z^0 and $W^{\pm}$ are self coupling, and in addition, there are mixed couplings between the photon, $W^{\pm}$ and Z^0. The Higgs couples only to the $W^{\pm}$ and Z^0 and the fermions.

2.2 Quantum Chromodynamics

Quantum chromodynamics in the Standard Model is based on the SU(3) gauge group. Under SU(3) symmetry, color charge is conserved. Each quark carries one of three color indices, r, g, b = red, green, blue), and an octet of gluons carry color anti-color charge. The group acts on color triplets for each of the six quarks. The gluon octet can be expressed in the following color states:

$$\begin{aligned}
|1\rangle &= \quad (r\bar{b} + b\bar{r})/\sqrt{2} \qquad & |5\rangle &= -i(r\bar{g} + g\bar{r})/\sqrt{2} \\
|2\rangle &= -i(r\bar{b} + b\bar{r})/\sqrt{2} \qquad & |6\rangle &= (b\bar{g} + g\bar{b})/\sqrt{2} \\
|3\rangle &= \quad (r\bar{r} + b\bar{b})/\sqrt{2} \qquad & |7\rangle &= -i(b\bar{g} + g\bar{b})/\sqrt{2} \\
|4\rangle &= \quad (r\bar{g} + g\bar{r})/\sqrt{2} \qquad & |8\rangle &= (r\bar{r} + b\bar{b} + 2g\bar{g})/\sqrt{6}
\end{aligned} \tag{2.10}$$

where r=red, b=blue, and g=green. The quark triplets are

$$\begin{pmatrix} u_r \\ u_b \\ u_g \end{pmatrix}, \begin{pmatrix} c_r \\ c_b \\ c_g \end{pmatrix}, \begin{pmatrix} t_r \\ t_b \\ t_g \end{pmatrix}, \begin{pmatrix} d_r \\ d_b \\ d_g \end{pmatrix}, \begin{pmatrix} s_r \\ s_b \\ s_g \end{pmatrix}, \begin{pmatrix} b_r \\ b_b \\ b_g \end{pmatrix} .$$

In nature, only color singlet (i.e. colorless) quark combinations exist. Mesons are made of quark anti-quark pairs with color anti-color respectively, $q_a\bar{q}^a$, and baryons

consist of 3 quarks with 3 different colors, $\epsilon^{abc} q_a q_b q_c$ where ϵ^{abc} is the antisymmetric tensor.

Leptons (and their respective neutrinos) do not carry color and, therefore, they do not participate in strong interactions. Only quarks and gluons interact via the strong force. The gluons are massless and one parameter, the strong coupling, g_s, describes the interactions. In a similar manner to the weak couplings of the $W^{\pm}$ and Z^0 bosons, the gluons are self coupling.

2.3 The Running of the Couplings

The strengths of electromagnetic, weak and strong interactions are quantified by their respective coupling constants. The strength of the electromagnetic force is defined by the Fine Structure Constant, α_{em} (Equation 2.4), and the weak and strong coupling constants, α_w and α_s, are given by

$$\alpha_w = \frac{g_w^2}{4\pi} \quad \text{and} \quad \alpha_s = \frac{g_s^2}{4\pi} \ . \tag{2.11}$$

The strengths of the forces depend on the distance between the interacting particles and, therefore, these so called *constants* vary. For the electromagnetic force, this can be understood if we imagine that the vacuum acts like a dielectric medium. As the separation between two charged fermions increases, fermion antifermion pairs (e.g. e^+e^-) begin to pop up in the vacuum. These pairs screen the bare charges and give an effective charge that is somewhat reduced. This is referred to as *vacuum polarization*. In Figure 2.2(a), this is depicted in a Feynman diagram. The fermion

antifermion pairs are represented by a fermion loop (or bubble) in the photon propagator.

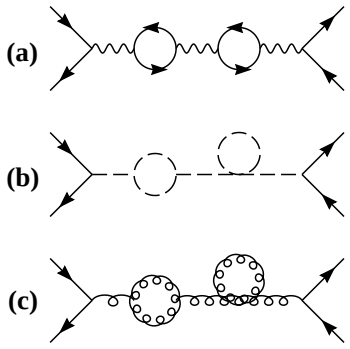

Figure 2.2: Feynman loop diagrams. (a) Fermion loops in the photon propagator. (b) W and Z loops in the Z propagator. (c) gluon loops in the gluon propagator.

At distances greater than $2.43 \times 10^{-10} cm$ (the Compton wavelength of the electron), the electronic charge is fully shielded and $\alpha_{em} \approx \frac{1}{137}$. If we increase our energy (decrease deBroglie wavelength) to 80 GeV ($M_W c^2$), the coupling increases to $\alpha_{em} \approx \frac{1}{129}$.

In the cases of the weak and strong forces, matters are complicated by the self coupling of the force mediators. In addition to fermion loops, we have $W^{\pm}$, Z^0, and gluon loops (see Figure 2.2(b) and 2.2(c). These compete with the fermion loops so that the forces actually decrease as energy increases (wavelength decreases).

This was a very important discovery in QCD physics because the quarks, while inseparable at low energy (known as *confinement*), behave as free particles at very high energies. This is referred to as *asymptotic freedom*.

2.4 Cross Sections

In classical physics, the cross section for a given interaction is defined as the area over which the desired interaction can take place. For example, the cross section for an arrow hitting a target is the area of the target. The interactions we are interested in, however, are not simply "hit or miss" interactions. Particles do not have to "touch" to interact. In these interactions, it may be more useful to imagine the particles as fields (electroweak and/or strong fields) rather than hard point like objects. Since the forces span to infinity, the absolute cross sections for electroweak and strong interactions are infinite. To make some quantitative sense out of this, we study differential cross sections, $d\sigma$, for various kinematical cuts. This is defined as

$$d\sigma = \frac{2\pi}{\hbar}|M|^2 \times (\text{phase space}) \ , \tag{2.12}$$

where $\hbar$ is the reduced Planck's constant, $h/2\pi = 6.5822 \times 10^{-22} MeV sec$, divided by 2π, M is the amplitude (or matrix element). The *phase space* term contains all the kinematic constraints (e.g. masses, energies and momenta of the incoming and outgoing particles). This is handled by integrating over the 4 momenta of the outgoing particles (in the kinematic region of interest) with a delta function included to ensure conservation of 4 momentum. The matrix element contains the meat of the calculation. This contains all the dynamical information about the interactions (e.g. coupling strengths, vacuum polarization, 4 momenta of the internal propagators, etc.).

In the case of $p\bar{p}$ collisions, the matrix element is complicated by the fact that

protons and antiprotons are composite particles made of *partons* (a generic term for quarks and gluons). We are interested in $p\bar{p}$ collisions in which an interaction between one parton in the proton and one parton in the antiproton interact resulting in 2 or more hard (i.e. energetic) partons emerging at large angles with respect to the collision axis. The remnant partons which did not take place in the hard interaction continue along the collision axis. An example of this is illustrated in Figure 2.3 where partons i and j (in the proton and antiproton respectively) interact producing partons j and k (plus the proton and antiproton remnants). The matrix element for this interaction can be factorized into two parts: the scattering amplitude which defines the hard process, $\hat{\sigma}(i, j \rightarrow k, l)$, and the probability that we find partons i and j in the proton and antiproton respectively, f_i (f_j). With this, the matrix element can be expressed as

$$M_{i,j\rightarrow k,l} = f_i(x_i, Q^2, \mu_F) f_j(x_j, Q^2, \mu_F) \hat{\sigma}(i, j \rightarrow k, l) \ , \tag{2.13}$$

where Q^2 is the momentum transfer in the hard process, and μ_F is the factorization scale which defines the separation between interactions calculated as part of the hard process and what gets absorbed into f_i and f_j. f_i (f_j) are called *parton distribution functions* (PDFs) which tell us the probability that parton i (j) carrying proton (antiproton) momentum fraction, x_i (x_j), will participate in the interaction.

Richard Feynman developed a method to calculate the scattering matrix elements, $\hat{\sigma}$. Using his diagrams, he devised a set of rules with which to calculate the hard scattering amplitude, $\hat{\sigma}$. A full explanation of the Feynman calculus is beyond the scope of this thesis. So we will point out just a few notable features and direct

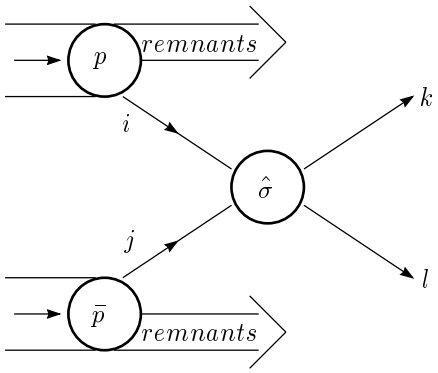

Figure 2.3: Factorization of the $p\bar{p}$ matrix element.

the reader to any one of the references, [18, 16, 17, 19, 20], for further enlightenment.

- At each vertex, 4 momentum must be conserved. In Figure 2.4a,

$$p_1^\nu = p_3^\nu + q^\nu \quad \text{and} \quad p_2^\nu = p_4^\nu - q^\nu \ . \tag{2.14}$$

- At each vertex, a term proportional to g is included ($g_s \propto \alpha_s$ for all vertices in Figure 2.4).

- For each internal line, a term proportional to $1/(q^2 - m^2)$ is included, where q is the 4 momentum of the propagator and m is its mass. The internal particles are virtual particles and, therefore, $q^2 \neq m^2$. Since the gluon is massless, the propagator in Figure 2.4a is just $1/q^2$.

- An integration over all undetermined internal momenta is performed (the fermion loop momenta in Figure 2.4b).

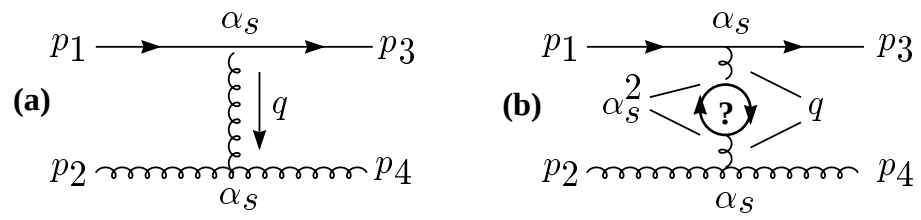

Figure 2.4: Feynman diagrams for qg→qg via gluon exchange. (a) Lowest order ($\mathcal{O}(\alpha_s^2)$) diagram. (b) 1 Loop ($\mathcal{O}(\alpha_s^4)$) diagram

2.5 Renormalization and the Strong Coupling, α_s

In calculating the contributions from internal loops in Feynman diagrams, integrals over loop momenta lead to divergences at very small momenta. To eliminate these, additional parameters are introduced through a regularization procedure. This allows us to write the divergent terms in some well-defined way (they still diverge in some limit of the regularization parameters). The divergences are then removed by absorbing them into the definitions of the physical quantites. Thereby, the theory is *renormalized*. This has the side effect of introducing a new parameter, μ_R, with units of energy. The exact renormalization procedure is arbitrary, but all must lead to the same observables. Therefore, the renormalization scale, μ_R, plays an important role in comparisons between theory and experiment. In this thesis, we will confine the discussion to predictions using the *modified minimum subtraction scheme* [22], $\overline{MS}$.

The running of the strong coupling constant, α_s, is determined by the renormalization group equation,

$$Q^2 \frac{\partial \alpha_s}{\partial Q^2} = \beta(\alpha_s) \ . \tag{2.15}$$

where Q is the energy scale of the hard interaction. The β function expansion in

powers of α_s is given by [20],

$$\beta(\alpha_s) = -b\alpha_s^2 \left(1 + b'\alpha_s + \mathcal{O}(\alpha_s^2)\right) \ , \tag{2.16}$$

where b and b' are defined as

$$\begin{aligned} b &= \frac{33 - 2n_f}{12\pi} \ , \text{and} \\ b' &= \frac{153 - 19n_f}{2\pi(33 - 2n_f)} \ . \end{aligned} \tag{2.17}$$

n_f is equal to the number of quark flavors available at a given Q^2.

Using only the leading order term in Equation 2.17, the dependence of the strong coupling constant, α_s, on the renormalization scale, $\mu = \mu_R$, at a given Q^2 can be written as

$$\alpha_s(Q^2) = \frac{\alpha_s(\mu^2)}{1 + \alpha_s(\mu^2)bt} \ , \quad t = \ln\frac{Q^2}{\mu^2} \ . \tag{2.18}$$

Including the next-to-leading order term, it is written as an implicit function,

$$\frac{1}{\alpha_s(Q^2)} + \frac{1}{\alpha_s(\mu^2)} + b' \ln\frac{\alpha_s(Q^2)}{1 + b'\alpha_s(Q^2)} - b' \ln\frac{\alpha_s(\mu^2)}{1 + b'\alpha_s(\mu^2)} = bt \ . \tag{2.19}$$

Equations 2.18 and 2.19 tell us how α_s varies with μ_R for a given Q^2, but they don't tell us the absolute value. This must be measured by experiment. Once α_s has been measured at one value of Q^2, it is determined for all Q^2 values. Experimentally, α_s has been measured for Q^2 values ranging from 1.5 GeV to 130 GeV. These different values are compared by scaling each value to the mass of the Z^0. The current world

Process	Q (GeV)	$\alpha_s(Q^2)$
τ Decay	1.777	0.35 ± 0.03
$p\bar{p}$ $\frac{\sigma(W+1jet)}{\sigma(W+0jet)}$	M_W	0.123 ± 0.025
Quarkonium Decay	9.45	0.163 ± 0.014
$e^+e^- \rightarrow$ Hadrons	35	0.146 ± 0.03
e^+e^-Event Shapes	58	0.125 ± 0.009
	34	0.14 ± 0.02
	29	0.160 ± 0.012
	130	0.114 ± 0.008
e^+e^-Fragmentation	91.2	0.125 ± 0.009
$e^-p \rightarrow e^-$+Jets	91.2	0.118 ± 0.008
Lattice QCD	91.2	0.117 ± 0.003

Table 2.5: Summary of α_s measurements [15].

average is [15]

$$\alpha_s(M_Z) = 0.119 \pm 0.002 \ . \tag{2.20}$$

A summary of these measurements is shown in Table 2.5 and Figure 2.5. Our measurement (if completed) would span values of Q^2 from 100 to 900 GeV.

Another way of looking at this is to introduce a parameter, Λ, which represents the energy scale at which the coupling diverges. This defines the boundary of the perturbative domain and is defined by

$$\ln \frac{Q^2}{\Lambda^2} = -\int_{\alpha_s(Q^2)}^{\infty} \frac{dx}{\beta(x)} \ . \tag{2.21}$$

Expressed in terms of Λ, the leading order and next-to-leading order α_s are

$$\begin{aligned} LO \quad \alpha_s(Q^2) &= \frac{1}{bL} \\ NLO \quad \alpha_s(Q^2) &= \frac{1}{bL}\left(1 - \frac{b'}{b}\frac{\ln L}{L}\right) \ , \end{aligned} \tag{2.22}$$

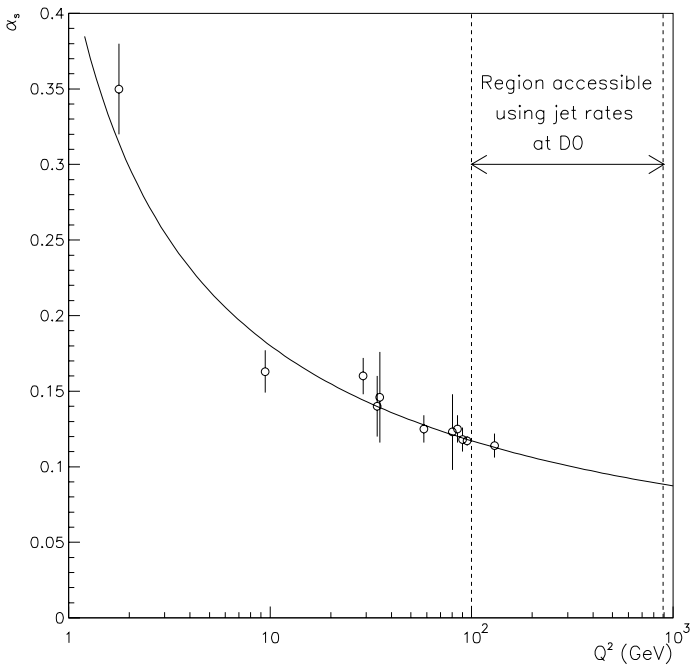

Figure 2.5: Graphical representation of the data from Table 2.5. The curve corresponds to the next-to-leading order running of $\alpha_s(Q^2)$ setting $\alpha_s(M_Z) = 0.119$. The region accessible using jet rates at DØ is also shown.

where $L = \ln(Q^2/\Lambda^2)$. The value for $\alpha_s(M_Z)$ quoted above gives a value of [15]

$$\Lambda^{(5)} = 237^{+24}_{-26} MeV \ , \tag{2.23}$$

calculated at next-to-leading order ((5) denotes a theoretical calculation including 5 flavors of quarks).

Chapter 3

Jet Production in $p\bar{p}$ Collisions

At the Fermilab Tevatron, protons collide with antiprotons at a center-of-mass energy, $\sqrt{s} = 1.8$ TeV. Most often, these collisions result in sprays of highly energetic particles (called *jets*). In this chapter, we will discuss the physics specific to jet production in $p\bar{p}$ collisions.

We begin with a quick view of a typical event in $p\bar{p}$ collisions which produces jets. Next, we define the variables used to define the kinematics of such events. Then, we give a brief description of the Monte Carlo event generators we use to test our methods and compare our results to theoretical predictions. Finally, we will discuss the motivation behind the measurement of the ratio of events with 3 or more jets to events with 2 or more jets, R_{32}.

3.1 $p\bar{p}$ Collisions

So far, we have considered only simple $2 \rightarrow 2$ particle reactions. What we actually observe in proton antiproton collisions is much more complex. When a proton and an antiproton collide at very high energies, their composite particles behave almost independently of one another such that only two partons (one from the proton and one from the antiproton) will most likely take part in the interaction. Two or more partons emerge from the interaction along with the remnants of the proton and antiproton. Immediately, these outgoing partons radiate gluons and/or produce pairs of quarks and antiquarks in a shower of partons. Then, the partons recombine into colorless composite particles (hadrons). The results of the collision are *jets* of particles.

Let us consider an interaction where a quark from a proton interacts with a gluon from an antiproton. The Feynman diagram for the interaction is shown in Figure 3.1. Figures 3.2 and 3.3 depict the interaction at 3 different levels before and after the collision respectively. Before the collision, we have a proton and antiproton at the hadronic level (Figure 3.2a). If we look a little closer, we see that the proton and antiproton are made up of a sea of quarks and gluons (Figure 3.2b). At the most elemental level, two partons, a quark and a gluon, take part in the hard interaction and the others do not participate (Figure 3.2c).

After the collision, two partons emerge from the hard process (Figure 3.3a). Immediately, the quark and gluon begin to radiate gluons and quark-antiquark pairs producing a shower of partons (Figure 3.3b). These partons fragment further, re-

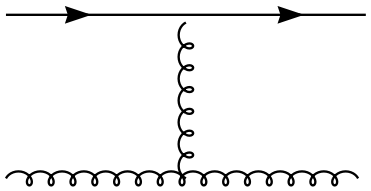

Figure 3.1: Feynman diagram for $qg \to qg$ by gluon exchange.

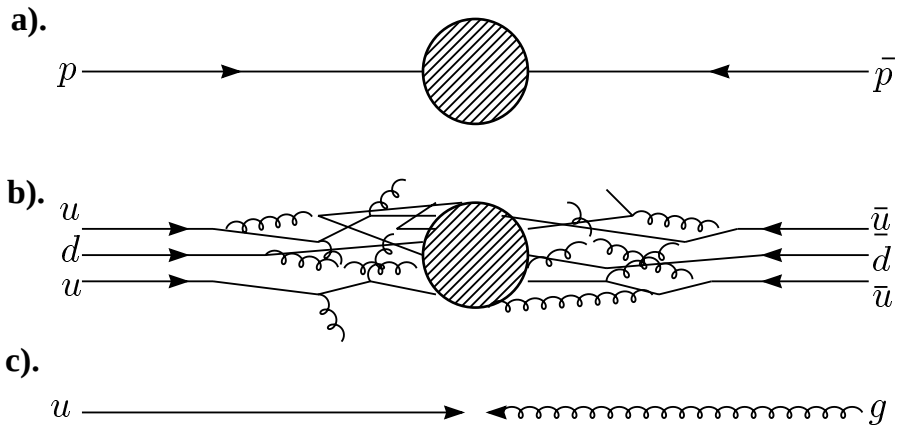

Figure 3.2: A quark from a proton interacts with a gluon from an antiproton (before). (a) At the hadron level, a proton collides with an antiproton. (b) At the parton shower level, a sea of quarks and gluons interact. (c) At the $2 \to 2$ parton level, a quark interacts with a gluon.

combine and form jets of colorless hadrons (Figure 3.3c).

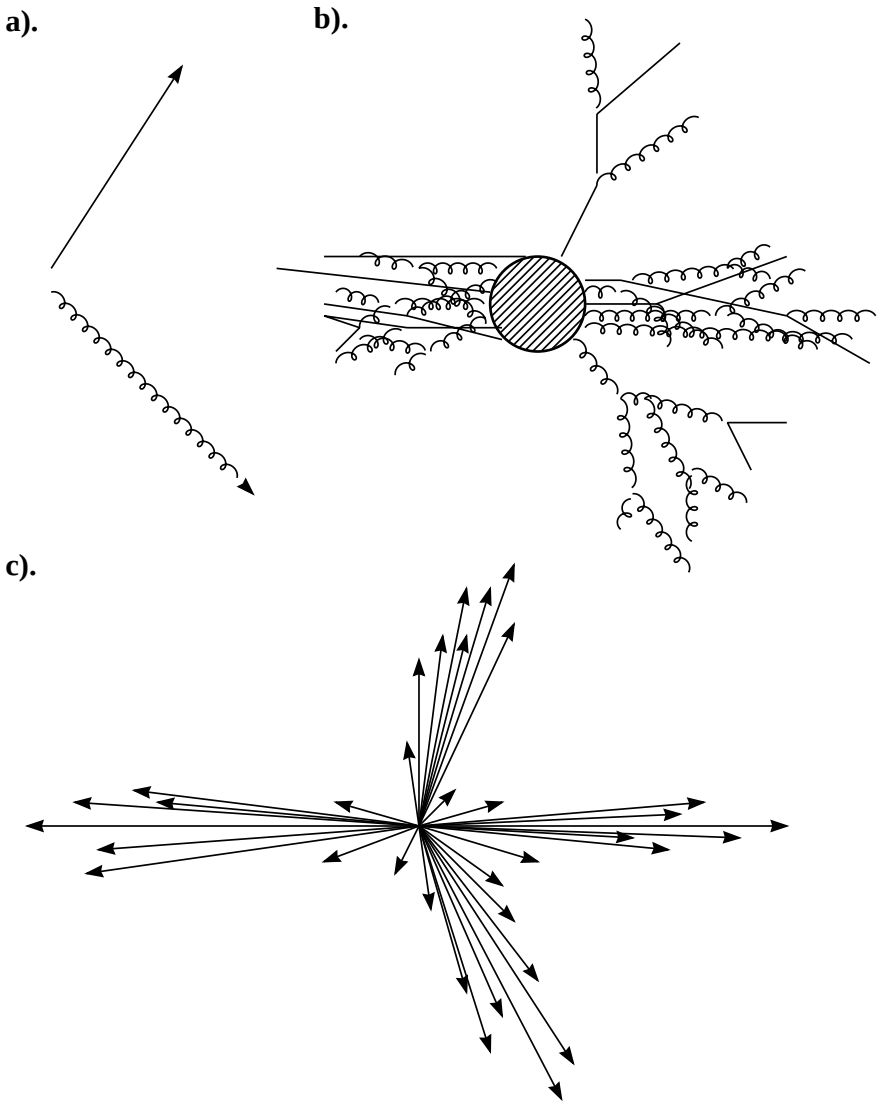

Figure 3.3: A quark from a proton interacts with a gluon from an antiproton (after). (a) At the $2 \rightarrow 2$ parton level, a quark and a gluon emerge. (b) At the parton shower level, jets of quarks and gluons emerge. (c) At the hadron level, jets of hadrons emerge.

Finally, these jets of hadrons deposit their energy in the detector. Shown in Figure 3.4 is an event as seen by the DØ detector. This is a side view of the detector (the z axis is the horizontal axis) where the transverse components (perpendicular to the z axis) are projected onto the vertical axis. The shaded regions depict energy

deposition in the detector and we see two large clusters of energy emerging from an interaction vertex. The DØ detector will be described in the following chapter.

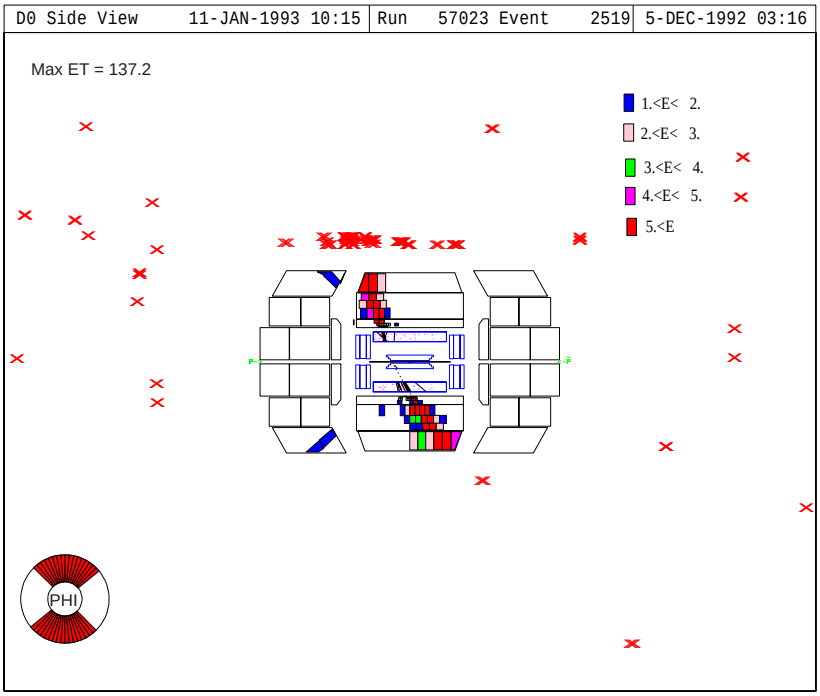

Figure 3.4: An event as seen by the DØ detector. The z axis defines left to right; the information has been averaged in ϕ.

3.2 $p\bar{p}$ Event Variables

The partons participating in the hard interaction do not have a fixed energy. Their energy is some fraction of the proton or antiproton energy. This allows us to study interactions which take place over a wide range of center of mass energies, $\sqrt{\hat{s}}$. One drawback to this is that the center-of-mass (c.m.) frame is likely to be Lorentz boosted with respect to the lab frame. We desire, therefore, to define the kinematics

in terms that are invariant under longitudinal Lorentz boosts.

We define the z-axis to lie along the proton-antiproton beams (the axis of the Lorentz boost). Under these conditions, for a given momentum vector, the azimuthal angle, ϕ, and the component of momentum in the x-y plane, $P_T = \sqrt{P_x^2 + P_y^2}$, are both boost invariant. In addition, we define a rapidity, y, which is also boost invariant (except for an additive factor):

$$y = \frac{1}{2} \ln \left(\frac{E - P_z}{E + P_z} \right) , \tag{3.1}$$

where E is the energy and P_z is the longitudinal component of the vector momentum. For massless 4 vectors, this reduces to the so called *pseudorapidity*, η, which is related to polar angle, θ, by

$$\eta = -\ln \left(\tan \frac{\theta}{2} \right) . \tag{3.2}$$

In $p\bar{p}$ collisions, the jets of particles are produced at high energies ($P >> M$) and, therefore, the pseudorapidity is approximately equal to real rapidity, $\eta \approx y$. Because η is defined by the polar angle, θ, it is much more easily measured than the real rapidity, y. Hence, the kinematic variables used are transverse momentum, P_T, the azimuthal angle, ϕ, and pseudorapidity, η. For historical reasons, we often refer to the transverse momentum, P_T as "E_T ".

3.3 Monte Carlo Event Generators

We will describe two types of Monte Carlo event generators. The Jetrad [23] and Herwig [24, 25] event generators provide good examples of both types and are the

most frequently used in jet physics at DØ.

As the parton shower develops, the available energy gets dispersed among the partons. This causes the strong coupling to strengthen (α_s increases) and the radiation becomes soft and/or collinear. Perturbation theory requires the coupling to be small and, therefore, at a certain point, the shower development cannot be calculated analytically.

At present, the matrix element for $p\bar{p}$ collisions can be calculated exactly to $\mathcal{O}(\alpha_s^3)$. The Jetrad [23] Monte Carlo is one such event generator. It includes tree level Feynman diagrams with 2 and 3 final state partons (no loops) and the interference terms between the 2 parton final state diagrams with and without an internal loop. An example of contributing Feynman diagrams is shown in Figure 3.5. The Jetrad event generator includes at most 3 final state partons (evolution to hadrons is not modeled).

It is also possible to rearrange the terms in the calculation so that soft/collinear radiation terms are *resummed* and included in the matrix element. This calculation, however, breaks down when the radiation is hard and produced at large angles. Thus, it is not possible to combine the two techniques into one calculation that would cover the full range of hard and soft parton splitting. The Herwig Monte Carlo event generator uses a resummation calculation evolved from a $2 \rightarrow 2$ matrix element to predict the parton shower.

In addition to this, the process where partons recombine to form colorless hadrons (called *hadronization*) is not well understood. It is approximated using a fragmentation function which gives the probability of finding a given hadron with some

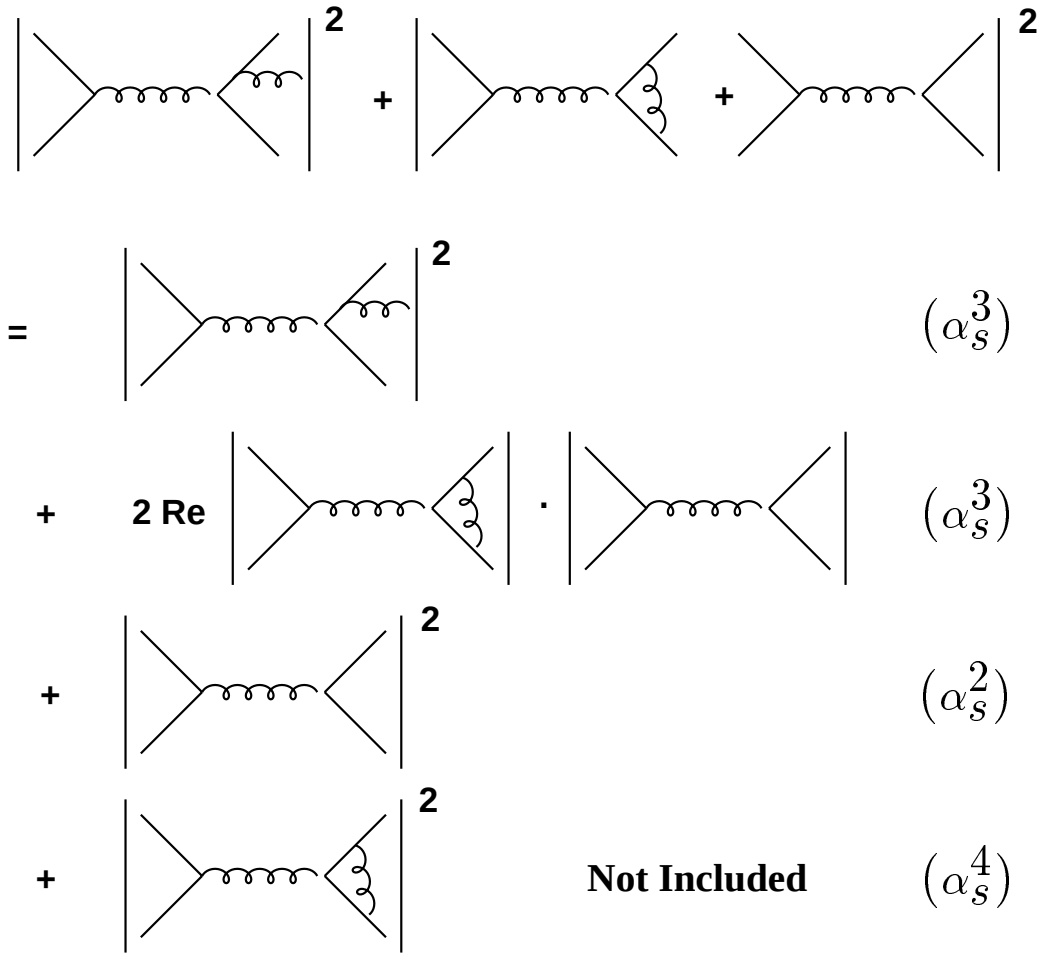

Figure 3.5: An example of $\mathcal{O}(\alpha_s^3)$ Feynman diagram contributions in the Jetrad Monte Carlo event generator. Tree level Feynman diagrams with 2 and 3 final state partons are included. The interference term between the 2 parton final state diagrams with and without an internal loop is included too. The last term ($\mathcal{O}(\alpha_s^4)$) is neglected.

fraction of the overall momentum. Various models are used which are tuned using experimental data and then, incorporated into Monte Carlo event generators. For the details regarding the Herwig event generator, the reader is directed to [24, 25].

3.4 Jets

Given that energy and momentum must be conserved, we can infer the kinematics of the partonic interaction by measuring jet properties. Defining jets, however, is less than straightforward. At the simple $2 \to 2$ parton level, there are two energetic partons well separated in ϕ, and there is little ambiguity even as the jet evolves through parton showering and hadronization. At $\mathcal{O}(\alpha_s^3)$, there can be 3 final state partons. Recall that the calculation breaks down for soft and/or collinear radiation. Therefore, jets must be defined in such a way so that they will be insensitive to these splittings. Quantities which are insensitive to soft/collinear radiation are often referred to as *infrared safe* quantities. An ideal jet algorithm recombines soft/collinear splittings. The specific jet definition determines which splittings are recombined, and, therefore, the theoretical calculation for a given cross section depends on the choice of jet definition. In Chapter 5, we will discuss two jet algorithms employed at DØ: the fixed cone and $k_\perp$ algorithms.

3.5 R_{32}

At lowest order, the hard scattering cross section for events with 3 final state partons (jets), σ^3_{LO}, is proportional to α_s^3,

$$\sigma^3_{LO}(Q^2, \mu, J) = \alpha_s^3(Q^2, \mu) C_3(Q^2, J) \ , \tag{3.3}$$

where α_s is given by Equation 2.18 and C_3 is constant for a given momentum exchange, Q^2, and jet definition, J. Likewise, the lowest order 2 jet cross section is proportional to α_s^2,

$$\sigma^2_{LO}(Q^2, \mu, J) = \alpha_s^2(Q^2, \mu) B_2(Q^2, J) \ . \tag{3.4}$$

At lowest order, therefore, the ratio of cross sections for 3 and 2 jet events, R_{32} is proportional to α_s,

$$R_{32}^{LO} = \frac{\sigma^3_{LO}}{\sigma^2_{LO}} = \frac{C_3(Q^2, J)}{B_2(Q^2, J)} \alpha_s(Q^2, \mu) \ . \tag{3.5}$$

This makes it possible to extract a value of α_s from an experimental measurement of R_{32} given the constant terms, C_3 and B_2. At this time, the theoretical calculation for R_{32} is not available at anything other than leading order. It is only a matter of time before theorists will be able to calculate next-to-leading order 3 jet cross section, and we can begin to speculate as to the method of extraction based on what is available for the next-to-leading order 2 jet cross section calculation.

At next to lowest order, we can define an inclusive cross section for 2 jets (events

where there are 2 or more final state partons). The matrix element is given by

$$\sigma^{\geq 2}_{NLO}(Q^2,\mu) = \alpha_s^2(Q^2,\mu)B_2(Q^2,J) + \alpha_s^3(Q^2,\mu)B_3(Q^2,\mu,J) \tag{3.6}$$

where the coefficient for the α_s^3 term, B_3, has a dependency on μ given by

$$B_3(Q^2,\mu) = B_2(Q^2,J)\ln\left(\frac{Q^2}{\mu}\right) + B_3^0(Q^2,J)\ . \tag{3.7}$$

In the next to lowest order case, α_s is given by Equation 2.19. The 3 jet inclusive cross section calculation is not available at this time to next to lowest order. However, we expect it to take a similar form,

$$\sigma^{\geq 3}_{NLO}(Q^2,\mu) = \alpha_s^3(Q^2,\mu)C_3(Q^2,J) + \alpha_s^4(Q^2,\mu)C_4(Q^2,\mu,J) \tag{3.8}$$

where C_4 is given by

$$C_4(Q^2,\mu) = C_3(Q^2,J)\ln\left(\frac{Q^2}{\mu}\right) + C_4^0(Q^2,J)\ . \tag{3.9}$$

Here, the ratio of 3 to 2 jet events will be given by

$$R_{32}^{NLO} = \frac{C_3(Q^2,J) + \alpha_s(Q^2,\mu)C_4(Q^2,\mu,J)}{B_2(Q^2,J) + \alpha_s(Q^2,\mu)B_3(Q^2,\mu,J)}\alpha_s(Q^2,\mu)\ . \tag{3.10}$$

When the next-to-leading order calculation becomes available for 3 final state partons (i.e. C_4 is calculated), we will be able to extract α_s from the experimental measurement of R_{32} using the above equation.

The extraction of α_s is extremely sensitive to the choice of renormalization scale,

μ_R. As the calculations become available to higher and higher orders, the sensitivity to the renormalization scale lessens and it is possible to get a more accurate prediction.

The measurements of α_s shown in Table 2.5 are extracted using varieties of leading order (LO), next-to-leading order (NLO), next-to-next-to-leading order (NNLO), and resummation calculations. Almost all of the errors quoted there are totally dominated by theoretical uncertainties due to the choice of renormalization scale, μ_R, and we expect the same will be true for a measurement using jet rates at DØ. So the necessity and/or usefulness of such a measurement may come into question. The extraction of α_s from a measurement of R_{32} at DØ probes regions of phase space previously unavailable. And because α_s is a fundamental parameter of the Standard Model theory, such a measurement will become useful in the future when the theoretical uncertainties are better understood.

Chapter 4

The Tevatron and The DØ Detector

The DØ collider experiment is located at the Fermi National Accelerator Laboratory. Protons and antiprotons collide at a center of mass energy of 1.8 TeV. At this time, the Fermilab Tevatron produces the highest energy particles in the world (excluding cosmic rays). We present here a description of the Fermilab Tevatron Collider and the various components of the DØ detector.

4.1 The Fermilab Tevatron Collider

Protons are accelerated to 900 GeV in 5 stages:

1. Hydrogen (H^-) ions are created with 750 KeV.

2. The H^- ions are accelerated to 400 MeV and the electrons are stripped off.

3. The protons are accelerated in the Booster ring to 8 GeV.

4. The protons are accelerated in the Main ring to 150 GeV.

5. Finally, the protons accelerate in the Tevatron to 900 GeV.

The components involved in these 5 stages are shown in Figure 4.1

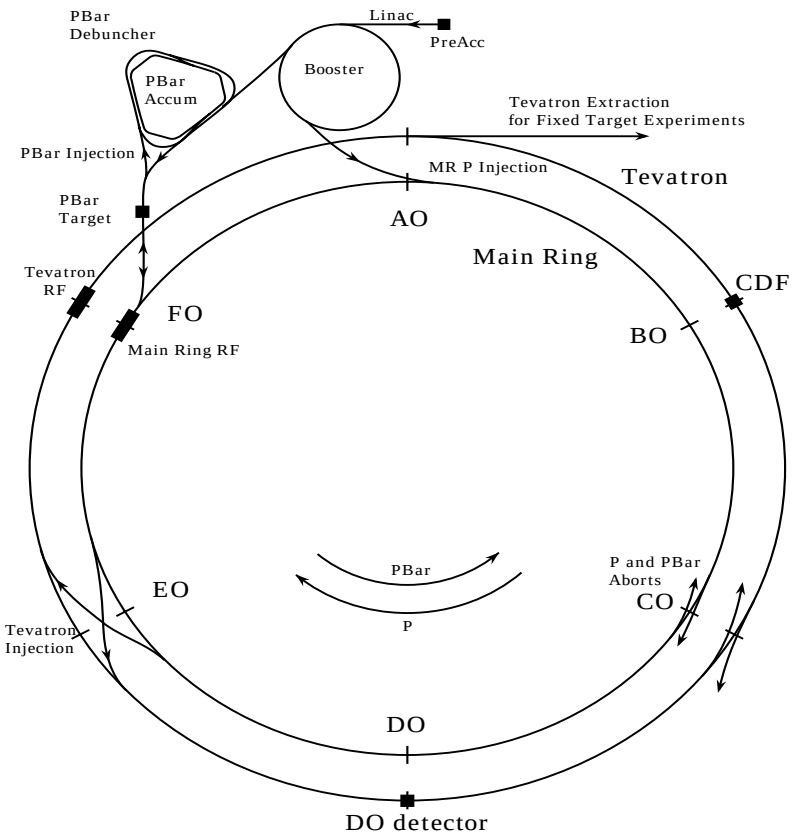

Figure 4.1: Overview of the Fermilab Tevatron.

In the first stage, electrons are added to hydrogen atoms with an energy of 750 KeV (30 times the energy of electrons in a television picture tube). This is done in an electrostatic generator called a *Cockcroft-Walton*.

Next, these negatively charged ions are introduced into a linear accelerator (LINAC) made up of drift tubes with an oscillating electric field. The oscillations are timed so that the ions are accelerated in bunches by a positive potential. The negative po-

tential occurs after the ions are free of the cavity. As the ions traverse the LINAC, the tubes become progressively longer to accommodate the increase in the speed of the ions. As they exit the LINAC, the ions pass through a carbon foil which strips off their electrons resulting in a beam of protons.

The protons enter an accelerator ring called the *Booster*. The Booster is a 500 foot diameter synchrotron which consists of resonant frequency (RF) cavities and magnets which bend the path of the bunches of protons into a circle. As the protons are accelerated, the electromagnetic field increases to match the speed of the bunches. The protons cycle around the Booster roughly 20,000 times before they leave with an energy of 8 GeV.

Next, they enter what is known as the *Main* ring. The Main ring is buried 20 feet below ground surface in a 10 foot wide tunnel. It is 2 km in diameter and consists of 1000 quadropole and dipole copper coiled magnets which focus and bend the protons in the main ring. Here, the protons are accelerated up to an energy of 150 GeV before they are dropped down into the Tevatron for the final stage.

During the Main ring stage, some of the protons are syphoned off and focused onto a target (typically nickel). Antiprotons (among many other particles) are produced in these collisions. The antiprotons are selected and directed to a *Debuncher* ring. The Debuncher ring is positioned in a separate tunnel and is shaped in a triangular ring of 500 feet per side. In the Debuncher ring, bunches of antiprotons are collected and "cooled" to within a small range of momenta and then they are stored in the *accumulator* ring directly below the Debuncher ring in the same tunnel. Once a reasonable store has been accumulated, the antiprotons are released into the Main

ring where they will be accelerated in opposite direction to the protons. Finally, they too are diverted down to the Tevatron for the final stage of acceleration.

The Tevatron synchrotron is positioned in the same tunnel as the Main ring. It is in this stage that the protons and antiprotons reach their maximum energy of 900 GeV. In order to produce a magnetic field large enough to bend the beams into a circular path at this energy, superconducting magnets are used. The superconducting magnets are kept cooled to a temperature of -450 degrees Fahrenheit by liquid helium. During the data taking run (1b) on which this thesis is based, the collider was operated with 6 bunches of protons and antiprotons (each) in the Tevatron. At two interaction points, BØ and DØ, the proton and antiproton beams collide. At either interaction point, the time between bunch crossings was $3.5\mu sec$.

4.2 The DØ Detector

The DØ experiment is so named because the detector is positioned around the DØ interaction point in the Tevatron ring. The DØ detector is a multipurpose collider detector. It is a multifaceted piece of apparatus designed to measure a wide variety of observables. A cut away view of the DØ detector is shown in Figure 4.2. The detector is made up of 4 subsystems:

- the Level Zero detector,
- the Tracking system,
- the Calorimeter, and

- the Muon detector.

The Level Zero detector determines whether or not an inelastic collision took place when the proton and antiproton beams cross. A particle produced in a collision will first pass through the Tracking system. If it is charged, its path will be detected. Next, it will encounter the Calorimeter where it will most likely deposit its energy. If it is a muon, however, it is unlikely to interact with the material in the calorimeter and it will pass through the calorimeter and its path can be traced in the Muon detector. A magnet bends the path of the muon, and from the curvature of its path, the muon's momentum can be inferred.

This thesis is mainly concerned with jets of hadrons which deposit their energy in the calorimeter. Therefore, we will give only a brief description of the tracking and muon systems and concentrate our discussion on the calorimeter. We will also briefly discuss triggering and data taking.

4.2.1 The Level Zero Detector

The Level Zero Detector is used to determine if an inelastic collision took place during a bunch crossing. It also provides a rough estimate of the position of the interaction vertex. Ideally, the vertex would always occur at the center of the detector ($z = 0.0$). In reality, however, the vertex position is described by a gaussian with a width of about 25 cm and an offset of 8 cm from the center.

The Level Zero detector consists of two scintillator based hodoscopes surrounding the beampipe on either side of the interaction region. The hodoscopes detect charged

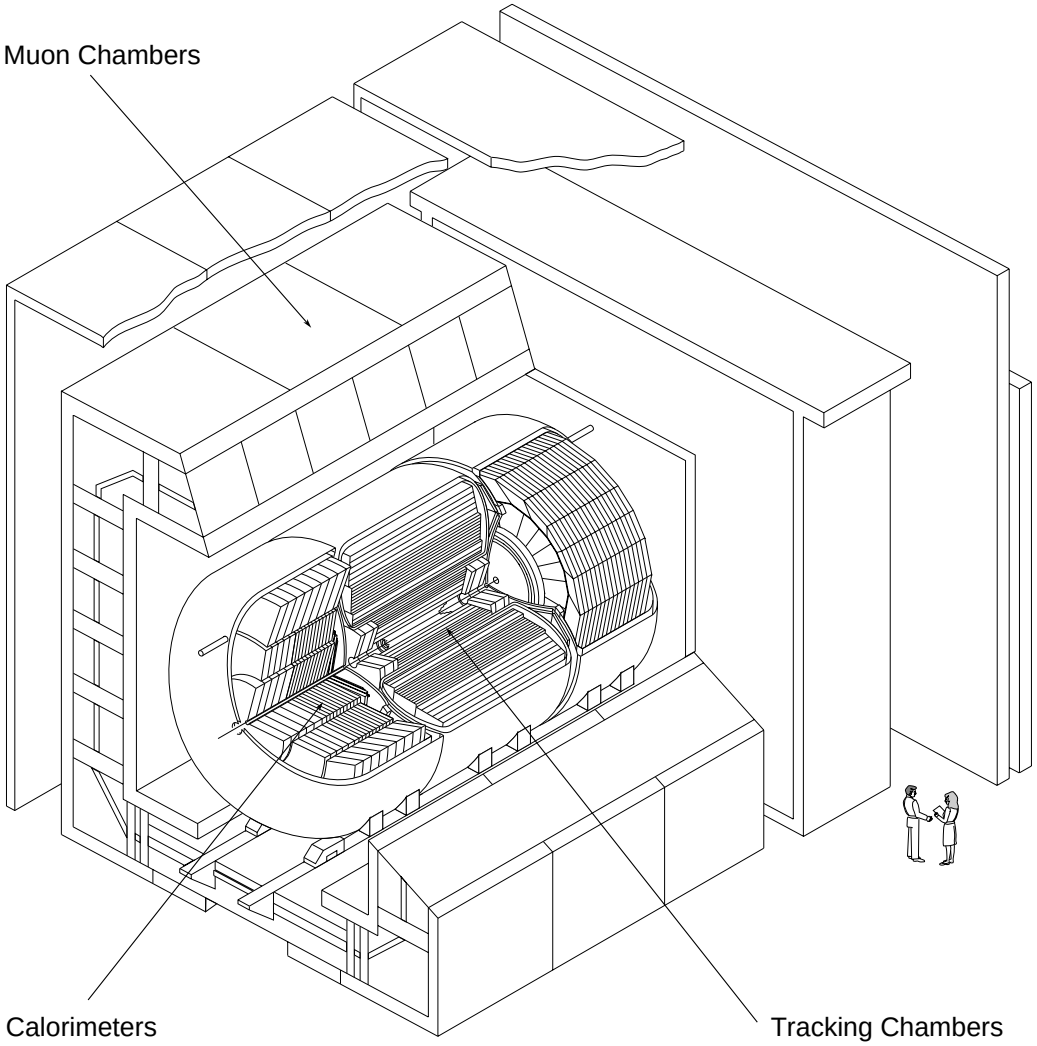

Figure 4.2: Cutaway view of the DØ detector.

particles. When a collision takes place, the remnants of the proton and antiproton shower close to the beamline. By taking the difference in the times that the two hodoscopes detect particles, the interaction point can be inferred.

4.2.2 The Tracking System

The tracking system consists of 3 separate detectors:

- a vertex detector (VTX),
- a transition radiation detector (TRD), and
- central and forward (in pseudorapidity) drift chambers (CDC and FDC).

A side view of these detectors is shown in Figure 4.3.

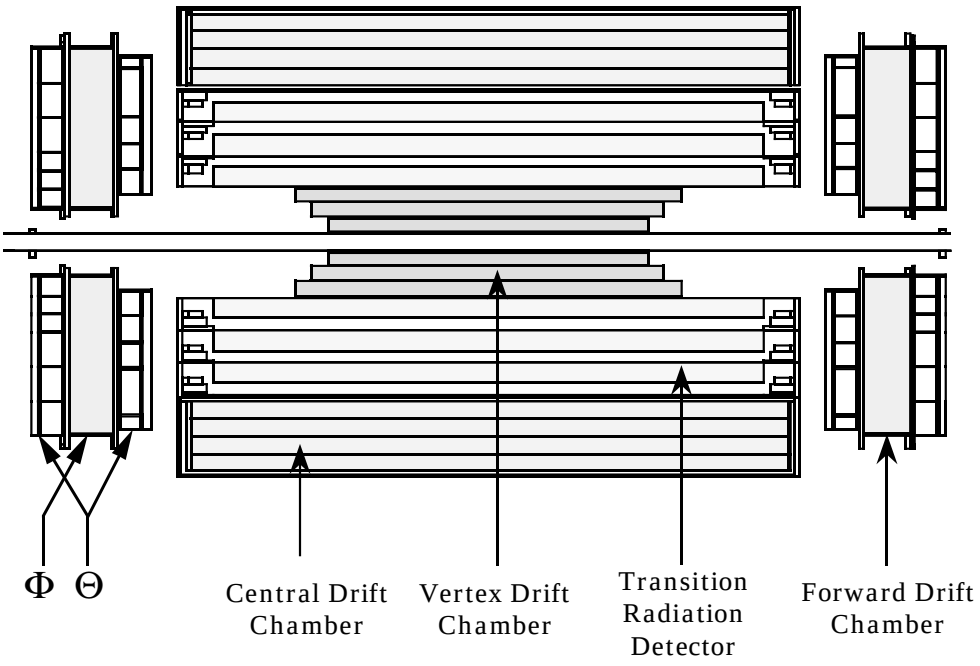

Figure 4.3: The four detectors which comprise the tracking system.

Innermost is the vertex detector (VTX) which gives a much more precise measurement of the interaction point than is determined by the Level Zero detector. The VTX has an inner radius of 3.7 cm and an outer radius of 16.2 cm. It contains 3 layers of wire chambers filled with CO_2(95%)-ethane(5%). As a charged particle passes through the chamber, it ionizes the gas and a potential difference in the chamber cause the electrons to collect on the wire and a signal is read out at both ends. The position of the wires provide a measure of the $r-\phi$ coordinate and the timing of the readout gives the position along the beamline (z) using charge division.

In the transition radiation detector (TRD), charged particles radiate photons when passing between regions of different dielectric constants and these photons are measured in X-ray detectors. The energy of the photons is inversely proportional to the mass of the particle. This allows us to differentiate between electrons and hadrons. The TRD consists of 3 layers of 393 polypropylene radiator foils and a layer of X-ray detectors.

Just inside the Calorimeter, lie the central and forward drift chambers (CDC and FDC). These operate on the same principle as the VTX.

4.2.3 The Calorimeter

The DØ calorimeter (Figure 4.4) is a uranium liquid argon sampling calorimeter. It provides exemplary coverage around the interaction region with fine segmentation. It was designed for ease of calibration with linear, compensating response to energy.

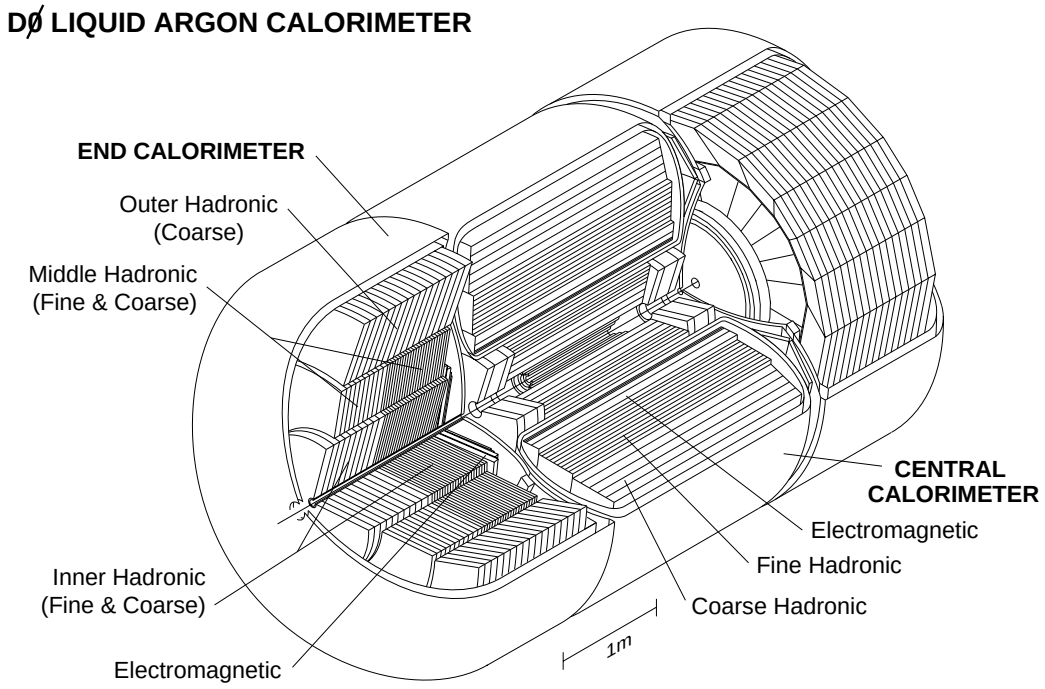

Figure 4.4: Cutaway view of the DØ calorimeter detector.

Particles entering the calorimeter interact with depleted uranium producing a shower of particles. These secondary particles ionize the liquid argon and a signal is produced on a copper readout pad. A schematic diagram of a unit cell is shown in Figure 4.5. The absorber plates are kept at ground and a readout board with a resistive surface is kept at 2000 V. The electron drift time across the liquid argon gap is 450 nsec. The signal is measured by a preamplifier and is then sent to a base line subtractor (BLS) for analog shaping. At this point, the signal is split. One is sent to the trigger framework and the other is sent to analog-to-digital converters (ADCs) where it is translated into energy. If the energy in the cell is within 2σ of the *pedestal* value, it is not read out. This *zero suppression* significantly reduces the number of cells read out. Otherwise, the pedestal value is subtracted and the energy read out. The pedestal value is the average background energy measured during a calibration run and σ is the width of the distribution.

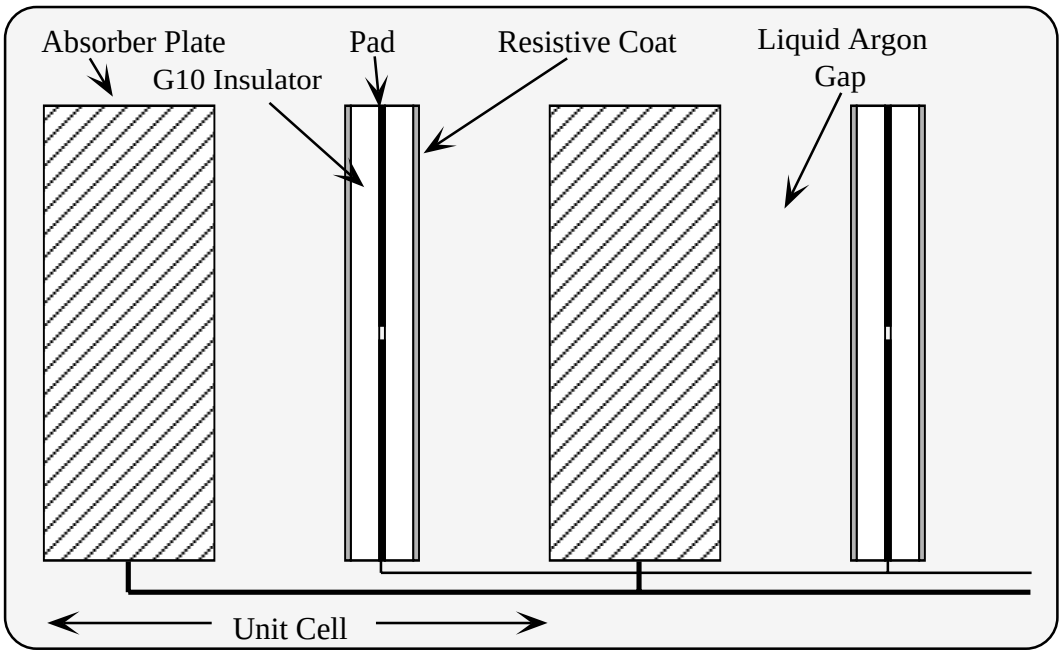

Figure 4.5: Schematic view of a liquid argon readout cell.

The DØ calorimeter is separated into 3 cryostats containing 3 separate calorimeters. One covers the central pseudorapidity region (CC), $|\eta^{det}| < 1.2$, and the other two cover the forward rapidity regions in the north and south respectively (EC), $1.5 < |\eta^{det}| < 4.5$. The calorimeter is also segmented longitudinally into 3 sections in order of increasing distance from the interaction region: electromagnetic (EM), fine hadronic (FH) and coarse hadronic (CH).

The EM section is comprised of 4 layers of cells with 3 mm thick uranium plates in the CC and 4 mm plates in the EC. The thickness of the layers increases going away from the interaction with 2, 2, 7 and 10 radiation lengths (X_0). The 1st, 2nd and 4th layers are segmented in $\eta \times \phi$ by 0.1×0.1. The 3rd layer is where the maximum shower deposition occurs for an electromagnetic object (i.e. electron or photon) and has a finer segmentation of 0.05×0.05. A quadrant of the DØ calorimeter is shown

in Figure 4.6.

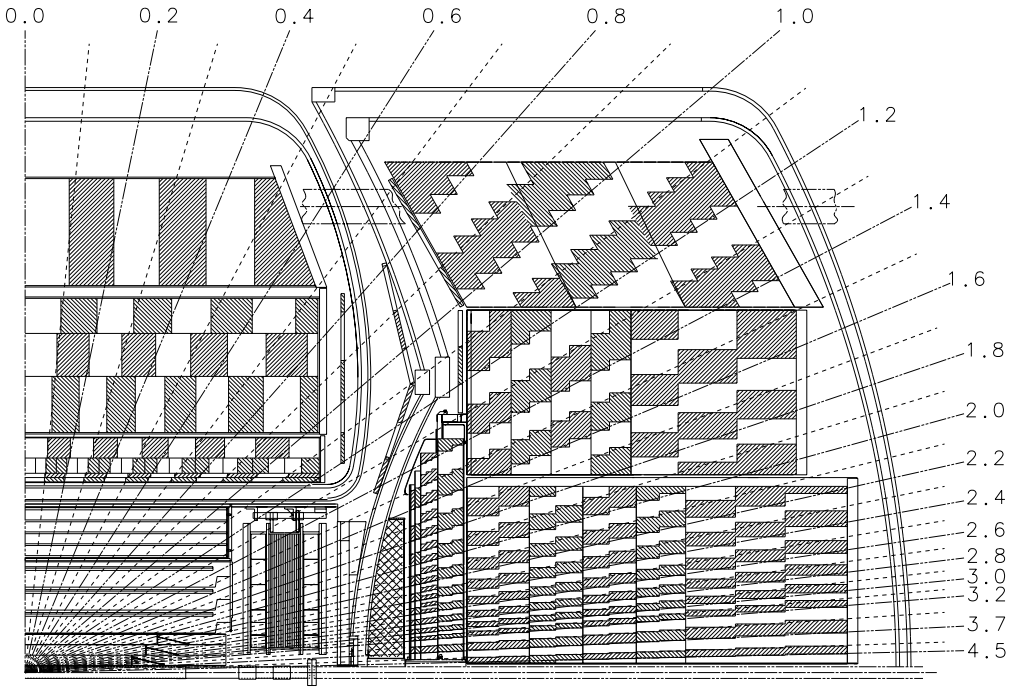

Figure 4.6: One quadrant of the DØ calorimeter.

The FH uses 6 mm uranium-niobium(2%) plates and is comprised of 3 cell layers in the CC and 4 layers in the EC. Its total depth is about 5 interaction lengths. All layers are segmented in 0.1×0.1 in $\eta \times \phi$.

The CH uses 46.5 mm copper plates in the CC and stainless steel plates in the EC. This amounts to 4 interaction lengths and only the most energetic particles make it through the outer wall of the cryostats.

The calorimeter modules were calibrated during test beam runs where sections of the calorimeter were exposed to particles with known energy. The response to energy was seen to be linear to within 0.5% for electrons above 10 GeV and for pions above 20 GeV. The ratio of these, e/π, is remarkably close to unity (less than 1.05). The energy resolution was found to be $15\%/\sqrt{E}$ and $50\%/\sqrt{E}$ for electrons and pions

respectively.

The Inter Cryostat Region

Particles entering the area between the CC and EC cryostats may encounter very little of the calorimetry. Two systems are placed in this region to mend this situation: the *massless gap* and the *inner cryostat* (ICD) detectors.

The massless gap detectors are made up of signal boards placed on the steel endplates of the calorimeters inside the cryostats. Alternating boards are set at ground and high voltage. They detect showering in the liquid argon between the steel endplates and the cryostat walls.

The ICD detector is positioned on the outside of the end cryostats. They are comprised of scintillating tiles (0.1×0.1 in $\eta \times \phi$) and signals are read out through bundles of wave shifting fiber.

4.2.4 The Muon Spectrometer

The Muon detector is divided into two subsystems with a total of 5 toroidal magnets. The wide angle muon system (WAMUS) covers the central rapidity region and the small angle muon system (SAMUS) covers the forward region. Both systems consist of 3 layers of proportional drift tubes (PDTs). The first layer lies inside the toroids and together with the tracking detectors, the incident path of a muon can be measured. After the muon's path is bent by the toroid, the deflection can be measured in the 2nd and 3rd layer PDTs and the momentum of the muon inferred.

The muon system is also used as a loose veto when a cosmic ray muon enters the detector during data taking.

4.2.5 The DØ Trigger System

As stated in Section 4.1, $p\bar{p}$ bunch crossings occur every $3.5\mu sec$. Most interactions are of little interest because they generally produce low transverse momentum objects. The DØ trigger system filters the events by making quick decisions about whether or not a given event is of interest. There are four levels of decision making: level 0, 1, 1.5, and 2. Each subsequent level is more discriminating yet more time consuming. The first three level decisions are hardware triggers and the fourth, level 2, is a software trigger. A block diagram of these four levels is shown in Figure 4.7.

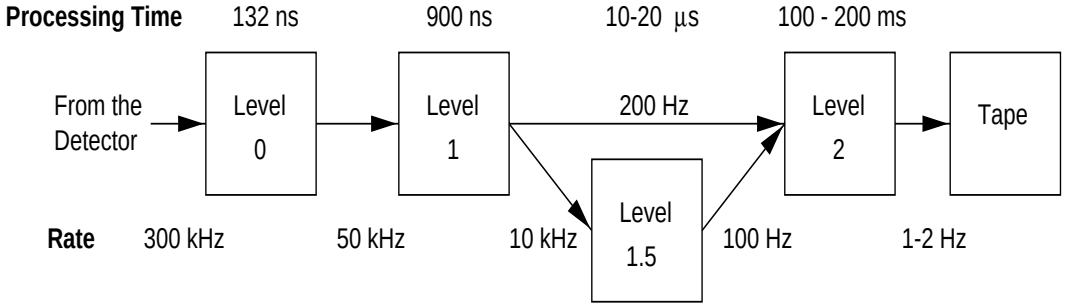

Figure 4.7: Block diagram of the DØ trigger system.

Level Ø

The level Ø trigger is the least discriminating. It simply looks for the break up of the proton and antiproton in the Level Zero detector. It's efficiency is >98%. It also provides information regarding multiple interactions occurring in a single bunch crossing and it measures the instantaneous luminosity.

Level 1 and Level 1.5

The level 1 trigger is divided into two components: muon and calorimeter. The muon trigger simply triggers on the number of muon tracks. If an event passes the level 1 muon trigger, a level 1.5 decision is made based on the transverse momentum of the muon. This creates a detector deadtime of one bunch crossing.

The calorimeter level 1 trigger makes fast sums of energy in towers in the calorimeter of 0.2×0.2 in $\eta \times \phi$. Several different reference sets are used to define energy cuts on the trigger towers in various sections of the calorimeter. There are also reference sets for energy summed in large groups of trigger towers. These are called *large tiles* and cover regions of 0.8×1.6 in $\eta \times \phi$.

After an event passes levels 1 and/or 1.5, it is passed to the level 2 system.

Level 2

The level 2 system is a farm of 50 VAXstation 4000/60 processors running identical executables which attempt to reconstruct each event. If the event is deemed worthy by the level 2 software, the detector information and run conditions are written to a disk buffer and eventually transferred to tape.

4.2.6 Offline Reconstruction

The *raw* data on tape is taken to another facility at Fermilab for processing. A large software package has been developed which reconstructs the data (RECO). The RECO software uses calibration information obtained from test beam data and

various algorithms to piece together physical objects such as photons, electrons, jets, muons, etc, from the raw detector data. Jets are reconstructed using the fixed cone jet finding algorithm. $k_\perp$ jets must be reconstructed in a separate package after the data has been processed through RECO. The $k_\perp$ and fixed cone jet finding algorithms are described in Chapter 5. All of the data used in this thesis used data reconstructed with version 12 of the reconstruction software (RECO v12).

Chapter 5

The $k_\perp$ and Cone Jet Algorithms

In Chapter 3, we discussed jet production in $p\bar{p}$ collisions. We showed an event display in which two jets of hadrons deposited their energy in the DØ detector (Figure 3.4). Shown in Figure 5.1 is the same event displayed in a 3 dimensional *lego* plot. The x and y axes represent η and ϕ coordinates shown in units of calorimeter towers, IETA and IPHI (a calorimeter tower equals 0.1×0.1 in $\eta \times \phi$). The vertical axis shows the amount of energy deposited in the towers and we see two large clusters of energy in the central part of the region along with some smaller clusters at large absolute values of IETA.

In order to relate these clusters of energy to a simple partonic interaction, we employ jet algorithms to reconstruct the parton momenta from the energy deposited in the calorimeter. We present here two jet finding algorithms used to analyze DØ data: the fixed cone and the $k_\perp$ jet algorithms. Compared to the fixed cone algorithm, the $k_\perp$ algorithm is more amenable to jet counting, and, therefore, we use $k_\perp$ jets to measure R_{32}. The fixed cone algorithm was established prior to the

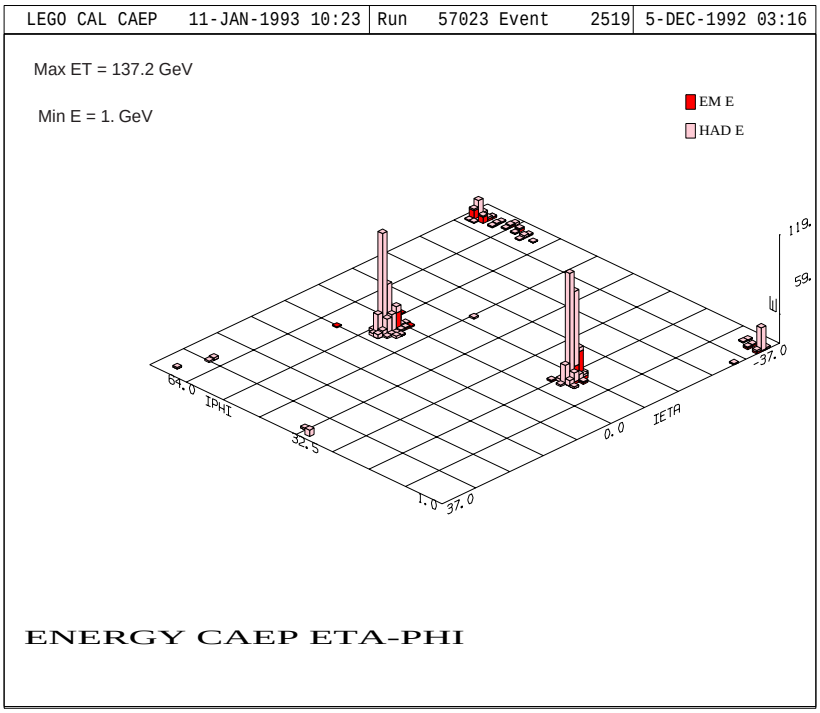

Figure 5.1: Lego plot of a 2 jet event as seen by the DØ detector. The x and y axes represent η and ϕ coordinates shown in units of calorimeter towers, IETA and IPHI (a calorimeter tower equals 0.1×0.1 in $\eta \times \phi$). The vertical axis shows the amount of energy deposited in the towers.

$k_\perp$ algorithm, however, and much of our work calibrating the $k_\perp$ jet algorithm is based on results obtained previously for cone jets. So we will begin our discussion with a brief description of the cone jet finding algorithm. The focus of this thesis is the implementation and calibration of the $k_\perp$ jet algorithm. So we will give a more detailed account of the $k_\perp$ jet algorithm.

5.1 The Fixed Cone Jet Algorithm

The fixed cone algorithm defines a jet by the sum of the 4-momenta contained in a fixed cone of radius, R, in $\eta-\phi$ space (see Figure 5.2). In other words, the 4-momenta of all particles with $\Delta R < R$ are included,

$$\Delta R_i = \sqrt{(\eta_J - \eta_i)^2 + (\phi_J - \phi_i)^2} < R \ , \tag{5.1}$$

where η_J and ϕ_J is define the center of the jet cone and η_i and ϕ_i give the position of a 4-vector inside the cone. Cone jets are found using an iterative procedure at DØ in the following way [36].

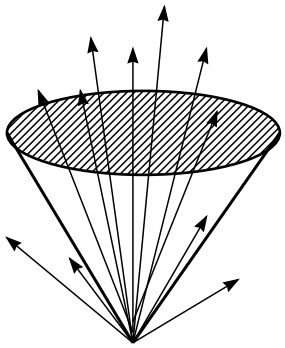

Figure 5.2: Fixed cone jet.

1. One starts with a list of 4-momenta describing partons, hadrons, or energy deposited in a detector.

2. A reasonably high P_T particle is chosen as a beginning (called a *seed*).

3. A cone of radius R in $\eta - \phi$ is drawn around the seed axis.

4. A new jet axis is found defined by the P_T weighted η and ϕ of the particles in the cone,

$$\eta = \frac{\sum_{i=1}^{n} \eta_i P_{T\,i}}{E_T} \quad \text{and} \quad \phi = \frac{\sum_{i=1}^{n} \phi_i P_{T\,i}}{E_T} \ . \tag{5.2}$$

   where E_T is defined as the scalar sum of the P_T of the particles inside the cone,

$$E_T = \sum_{i=1}^{n} P_{T\,i} \ . \tag{5.3}$$

5. Steps 3 and 4 are repeated (substituting the new jet axis for the seed axis) until a stable jet axis is found.

6. The η, and ϕ of the jet are redefined by

$$\eta = -\ln\left(\tan\left(\frac{\theta}{2}\right)\right) \quad \text{and} \quad \phi = \tan^{-1}\left(\frac{P_X}{P_Y}\right) \ , \tag{5.4}$$

   where

$$\theta = \sin^{-1}\left(\frac{E_T}{E}\right) \ , \quad P_X = \sum_{i=1}^{n} P_{x\,i} \quad \text{and} \quad P_Y = \sum_{i=1}^{n} P_{y\,i} \ . \tag{5.5}$$

Infrequently, two jets may be found with cones that overlap. In such cases, a *split/merge* criterion must be applied to decide if the jets should be merged into one jet or divided into two jets. At DØ the jets are merged if the shared energy is less

than 50% of the E_T of the lower E_T jet. Otherwise, the shared energy is divided between the two jets and their E_T η, and ϕ are recalculated as in step 6.

It was mentioned in Chapter 3 that at present, the matrix element is calculated to $\mathcal{O}(\alpha_s^3)$ only. In such calculations (e.g. Jetrad Monte Carlo events), there can be at most 2 partons produced, and at most, 2 partons can be included in a jet. In such cases, it is possible that the two partons are separated by some distance, r, in $\eta - \phi$ space such that $R < r < 2R$. Using the iterative method described above, the two partons will not be combined into a single jet. After parton showering and hadronization, however, it is possible that they will be merged into a single jet. We introduce an additional parameter, R_{sep}. Then, we combine the two partons if they are within $R_{sep} \times R$ of one another (typically $R_{sep} \sim 1.2 - 1.3$). The R_{sep} parameter is tuned to match what is seen experimentally in the splitting and merging of jets.

The prescription where the jet axis is defined by the P_T weighted center and the jet E_T is defined by scalar summed P_T (step 4) is known as the *Snowmass* recombination scheme. It was agreed upon as the standard recombination scheme for fixed cone jets during the Summer Study on High Energy Physics in Snowmass, Colorado, in 1990. The final jet η and ϕ definitions (step 6) were found to give better agreement between Herwig Monte Carlo jets at the parton shower, hadron, and detector levels and are therefore used in the DØ implementation of the fixed cone algorithm.

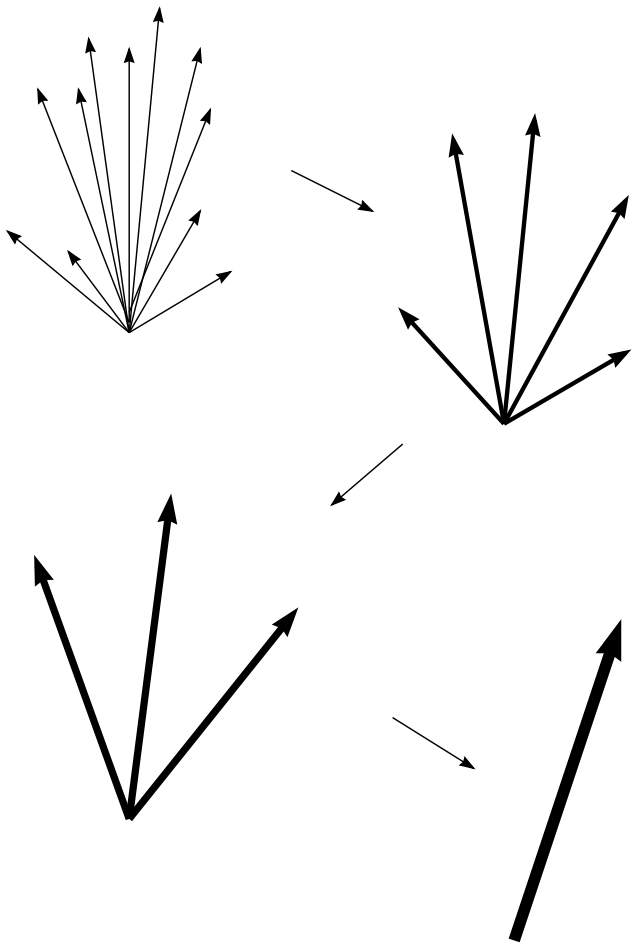

Figure 5.3: $k_\perp$ jet clustering.

5.2 Clustering Algorithms for e^+e^-Collisions

Unlike the cone jet finding algorithm described above, clustering algorithms begin by considering individual pairs of particles. We start with a list of 4-vectors describing partons, hadrons or detector information. The pairs of particles are evaluated based on some *closeness* criterion in phase space and the closest pair is merged into a single 4-vector. The merged particle is compared to all the other particles and the process is repeated until some stopping criteria has been satisfied. This is illustrated in Figure 5.3 and the basic steps in e^+e^-clustering algorithms are as follows.

1. For each pair of particles, i and j, we calculate some closeness function, y_{ij}.

2. The minimum y_{min} of all y_{ij} is found.

3. y_{min} is compared to some parameter, y_{cut}.

4. If $y_{min} < y_{cut}$ particles i and j are removed from the list of 4-vectors and merged into a new pseudo particle, k. y_{kj} is calculated for all other particles and we return to step 2.

5. If $y_{min} > y_{cut}$, then clustering stops and we are left with a list of jets.

The first of such algorithms was introduced by the JADE collaboration [37, 38]. In this algorithm, the closeness function is the scaled invariant mass,

$$y_{cut} > y_{ij} = \frac{{M_{ij}}^2}{{E_{vis}}^2} \tag{5.6}$$

where E_{vis} is the visible energy of the event. The pair mass is calculated for massless particles as

$$M_{ij}{}^2 = 2E_iE_j\,(1 - \cos\Theta_{ij}) \tag{5.7}$$

where Θ_{ij} is the angular separation. This can result in "fake" jets when many soft particles belonging to unrelated parton showers are combined. This is illustrated in Figure 5.4a where clustering begins by combining 4-vectors, 1 and 2, resulting in 4-vector, a. Since the algorithm is sensitive to soft radiation, it is not infrared safe (as was discussed in Chapter 3).

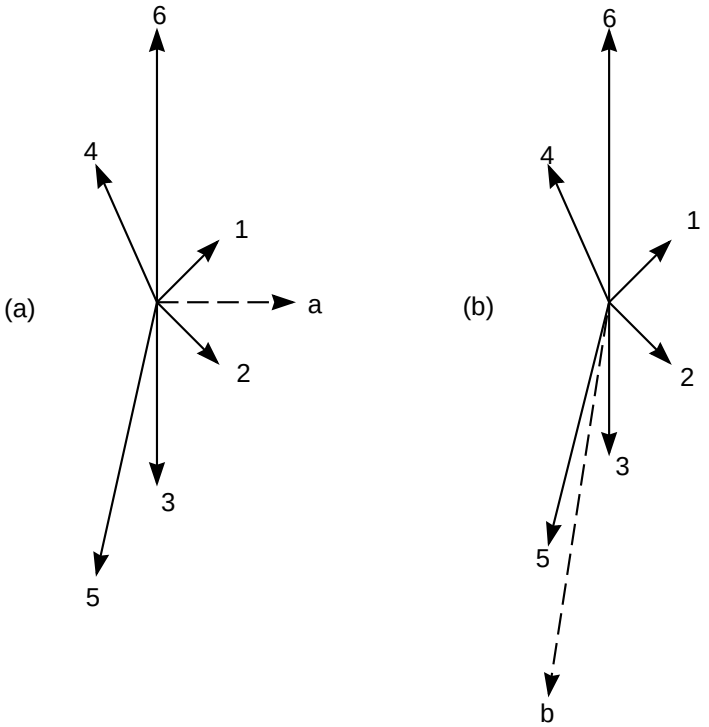

Figure 5.4: Jet Clustering in e^+e^-Collisions. (a) The JADE algorithm. (b) The $k_\perp$ (or Durham) algorithm.

Later, the $k_\perp$ (or Durham) algorithm was proposed with the argument that it has more of a tendency to be infrared and collinear safe and is less subject to hadronization corrections[39]. It was noticed that by simply replacing E_iE_j in the invariant mass equation (5.7) by $min(E_i^2, E_j^2)$, the problem would be solved. Soft particles would be merged with their nearest energetic neighbor instead of with other soft particles. This is illustrated in Figure 5.4b where 4-vectors, 3 and 5, are combined into 4-vector, b. For small angular separation, it can be shown that the new function approximates the minimum relative transverse momentum,

$$\begin{aligned} {k_{\perp,ij}}^2 = & \quad \min\left({E_i}^2, {E_j}^2\right)\sin^2\Theta \\ \cong & \quad 2\min\left({E_i}^2, {E_j}^2\right)(1-\cos\Theta_{ij}), \quad for\ \Theta_{ij} \to 0. \end{aligned} \tag{5.8}$$

Thus, it was dubbed the $k_\perp$ algorithm with $k_\perp$ as the new closeness parameter.

5.3 Adaptation of the $k_\perp$ Algorithm for $p\bar{p}$ Collisions

The event structure in $p\bar{p}$ collisions differs from e^+e^- collisions and this results in some modification of the $k_\perp$ jet definition. The variables used to assign particles (final state partons, hadrons or calorimeter cells) to jets in e^+e^- physics are the energies, E, and the polar and azimuthal angles, θ and ϕ. In $p\bar{p}$ collisions, the c.m. frame of the hard process is often moving with respect to the lab frame. Thus, the variables used must be boost invariant along the beam axis, $E_T = P_T$, η and ϕ.

$k_\perp$ can be expressed in terms of boost invariant quantities in the following way

for pairs of massless particles:

$$k_{\perp,ij}{}^2 \cong 2\min\left(E_{T,i}{}^2, E_{T,j}{}^2\right)\left[\cosh\left(\eta_i - \eta_j\right) - \cos\left(\phi_i - \phi_j\right)\right] . \tag{5.9}$$

As $\Delta\eta, \Delta\phi \to 0$, it can be expressed as

$$k_{\perp,ij}{}^2 \cong \min\left(E_{T,i}{}^2, E_{T,j}{}^2\right) R_{ij}^2 , \tag{5.10}$$

where $R_{ij}^2 = \Delta\eta^2 + \Delta\phi^2$.

In e^+e^- collisions, essentially all of the hadrons in the final state are thought to be associated with final state partons in the hard scattering process. In collisions producing high E_T jets, all particles should be assigned to a jet. The final state hadrons in $p\bar{p}$ collisions, on the other hand, are associated not only with the final state partons in the hard scattering process, but with radiation from partons in the incident $p\bar{p}$ pair as well as the remnants of the $p\bar{p}$. Therefore, not all the particles should be assigned to the high E_T jets, but many may be associated with the *beam jets* ($p\bar{p}$ remnants).

In addition to this, the c.m. energy of the hard process (defined as $\sqrt{\hat{s}}$) is variable and unknown. In the Durham algorithm described above, the closeness function is scaled by visible energy in the event,

$$y_{ij} = \frac{k_{\perp\ ij}}{E_{vis}} , \tag{5.11}$$

and the stopping parameter, y_{cut}, is dimensionless. Since E_{vis} ($\sqrt{\hat{s}}$) is not known in $p\bar{p}$ collisions, we must provide an alternative prescription for stopping the clustering.

A few different modifications have been suggested to adapt the Durham algorithm for use in $p\bar{p}$ collisions [41, 40]. The $k_\perp$ algorithm we have implemented at DØ is based on the algorithm suggested by Ellis and Soper in [41]. Below we describe the $k_\perp$ algorithm we have implemented at DØ.

5.4 $k_\perp$ Jets at DØ

Before jets are reconstructed, a preclustering of calorimeter cells is performed [42]. The $k_\perp$ algorithm is an $\mathcal{O}(n^3)$ algorithm (i.e. for n particles, $\sim n^3$ calculations must be performed) and it is desirable to reduce the ~6000 calorimeter cells in an average event without severely affecting the physics results. In preclustering, calorimeter cells are first added into towers in the calorimeter. Towers with E_T <0.2 GeV have their E_T redistributed in neighboring towers. The amount of E_T added to neighboring tower E_T is weighted by the neighboring tower E_T . Then, all towers within 0.2 of each other in $\eta - \phi$ space are combined. The E_T redistribution and tower merging is done using scalar E_T addition (subtraction in the case of negative E_T). In order to have a consistent comparison to jets at the parton and hadron level, we also perform the preclustering prior to jet reconstruction of partons and hadrons. There, parton and hadron 4 vector information takes the place of the calorimeter towers.

After the preclustering is performed, we apply a jet reconstruction algorithm. The jet algorithm we employ does not use a cutoff parameter, y_{cut}. Instead, particles are combined until all objects are separated $\eta - \phi$ space by some value

$$R_{ij}{}^2 > D^2, \tag{5.12}$$

where i and j are jets constructed by successively combining particles. The $k_\perp$ jet recombination procedure is as follows.

1. For each pair of particles (preclusters), i and j, we calculate the function

$$d_{ij} = minimum\left({E_{T,i}}^2, {E_{T,j}}^2\right)\frac{{R_{ij}}^2}{D^2} \tag{5.13}$$

   where $D = 1$. Then we define for each particle, i,

$$d_i = {E_{T,i}}^2. \tag{5.14}$$

2. The minimum d_{min} of all the d_i and d_{ij} is found.

3. If d_{min} is a d_{ij}, particles i and j are merged into a new, pseudo-particle k with

$$\begin{aligned} E_{T,k} = P_{T,k} &= \sqrt{P_{x,k}^2 + P_{y,k}^2}\ , \\ \eta_k = -\ln\left(\tan\tfrac{\theta_k}{2}\right), &\quad \text{and} \quad \phi_k = \tan^{-1}\tfrac{P_{x,k}}{P_{y,k}}, \\ \text{with four vector} \quad {P_k}^\mu = {P_i}^\mu + {P_j}^\mu, &\quad \text{and} \quad \theta_k = \cos^{-1}\tfrac{P_{z,k}}{|\vec{P_k}|}. \end{aligned} \tag{5.15}$$

4. If d_{min} is a d_i (i.e. ${R_{ij}}^2 > D^2$ for all j), then the particle is deemed not "mergeable" and it is removed from the list of particles and placed in the list of jets.

5. Return to step 1. Repeat steps 1-5 until all particles have been merged into jets (i.e. ${R_{ij}}^2 > D^2$ for all ij). The result is a list of jets.

It is possible to employ alternate recombination schemes in step 3. We have derived an energy scale only for the 4-vector recombination scheme described here.

The 4-vector recombination scheme, ${P_k}^\mu = {P_i}^\mu + {P_j}^\mu$, is the natural choice because it is consistent with 4-momentum conservation. As a jet evolves from a simple partonic interaction in the hard process to a shower of particles in the detector, its 4-momentum must be conserved. It is, therefore, most appropriate to reconstruct a jet's momentum and energy by summing the 4-momenta of the constituents of the jet. Defining $E_T = P_T$ (versus $E \sin\theta$ or the scalar sum of E_T of the constituents) was decided upon because the definition of transverse energy is somewhat ambiguous for jets with mass while transverse momentum, P_T, is well defined and Lorentz invariant.

The Snowmass recombination scheme merges particles i and j into pseudo-particle k with

$$E_{T,k} = E_{T,i} + E_{T,j} \ , \quad \eta_k = \frac{E_{T,i}\eta_i + E_{T,i}\eta_i}{E_{T,i}} \ , \quad and \quad \phi_k = \frac{E_{T,i}\phi_i + E_{T,i}\phi_i}{E_{T,i}} \ . \tag{5.16}$$

It was suggested as an approximation to 4-vector recombination because it expedites theoretical calculations using the cone jet algorithm. For theoretical $k_\perp$ jet calculations there is no such advantage.

We define D=1.0 partly because this roughly corresponds to R=0.7 in the cone jet algorithm. D=1.0 was also seen to give fairly stable results in jet rate studies on Herwig Monte Carlo data comparing jets reconstructed from the parton shower, final state hadrons, and calorimeter cells.

Ellis and Soper examined the inclusive jet cross section for 100 GeV jet E_T and $|\eta| < 0.7$ using both the $k_\perp$ and cone jet algorithms [41]. At $\mathcal{O}(\alpha_s^3)$, they found similar results for $k_\perp$ jets and cone jets setting $D = 1.35 \times \mathcal{R}$. In addition, D=1.0

and $\mathcal{R}$=0.7 reduce the renomalization/factorization scale dependence, μ, for the $k_\perp$ and cone jet cross sections respectively.

A Side Note on $k_\perp$ and Cone Jet Sizes

It is difficult to compare the size of a $k_\perp$ jet to that of a fixed cone jet. Imagine a parton shower of 3 massless partons, all 3 at equal η, equal momenta and separated by 0.7 ϕ. They will all be included in a $\mathcal{R}$=0.7 cone jet, but the D=1.0 $k_\perp$ jet will only cluster two together. From this one may conclude a $\mathcal{R}$=0.7 cone jet is bigger than a D=1.0 $k_\perp$ jet. Now, imagine a similar shower except this time the particle in the center is 4 times as energetic as the other two and now they are separated by 0.8 ϕ. In this case, at most 2 will be included in a $\mathcal{R}$=0.7 cone jet, but all three will be included in a D=1.0 $k_\perp$ jet. In this case, the $k_\perp$ jet appears to be bigger.

It is difficult to extract any meaningful information from comparing $k_\perp$ jets to cone jets. What is more important is that we are able to compare our experimental results to theoretical predictions using the same jet algorithm. This is simply because a jet is defined by the algorithm employed. The $k_\perp$ jet algorithm can be applied at any level (partons, hadrons, calorimeter data) in exactly the same manner. Recall that cone jets needed an additional parameter, R_{sep}, in order to compare to $\mathcal{O}(\alpha_s^3)$ calculations. $k_\perp$ jets also have the feature that each 4-vector must be assigned to one and only one jet in the clustering procedure. This avoids adding additional split/merge criteria and makes the $k_\perp$ jet algorithm more suitable for jet counting.

5.4.1 Monte Carlo Event Jet Rates

When the $k_\perp$ jet finding procedure described above is concluded, we have a list of jets which are well separated in $\eta - \phi$ space. Many of these jets may be associated with the soft interactions between the remnants of the proton antiproton pair. They may also come from soft radiation from the partons involved in the hard interaction. The leading-order or next-to-leading order theory cannot accommodate this soft radiation, and if we include all the jets, we will not be able to extract α_s as we described previously. Therefore, it is necessary to make a cut to remove low P_T jets not associated with the hard process.

The probability for a parton to radiate a gluon (or split into a quark antiquark pair) is governed by α_s. This splitting is a function of the fraction of the original parton's momentum given to the radiated gluon (or quark antiquark pair). Therefore, we only count jets in an event if their P_T is greater than some fraction of the hard scale. To define the hard scale, we sum the P_T of the 3 highest P_T jets in each event, H_{T3},

$$H_{T3} = \sum_{i=1}^{3} P_{Ti} \ . \tag{5.17}$$

Then, all jets with P_T below some fraction times the hard scale ($P_T < f_{cut} \times H_{T3}$) are dropped [44],

To choose a reasonable fraction cut, we study Herwig (version 5.8) Monte Carlo data. The Monte Carlo data is generated with $2 \to 2$ parton E_T thresholds of 30, 60, 120, and 240 GeV. It is processed through the SHOWERLIB [48] DØ detector simulation.

Figure 5.5 shows fractional jet rates in Herwig Monte Carlo events as a function of the fraction cut, f_{cut}. We compare these rates for jets found after parton showering, hadronization, and detector simulation. If we set f_{cut} too high ($f_{cut} > 0.3$), there are events where only one jet passes our cut. These are events where the leading jet carries about half the available event E_T ($P_T^1 \approx H_{T3}/2$) and the remaining half is divided roughly equally between the second and third jets ($P_T^{2,3} \approx H_{T3}/4$). On the other hand, if we choose f_{cut} to be small, we begin to include many jets and the agreement between the three levels begins to break down. So a reasonable choice for f_{cut} seems to be in the range $0.15 < f_{cut} < 0.2$. We use $f_{cut} = 0.15$ because it gives us the largest signal for R_{32} in this range.

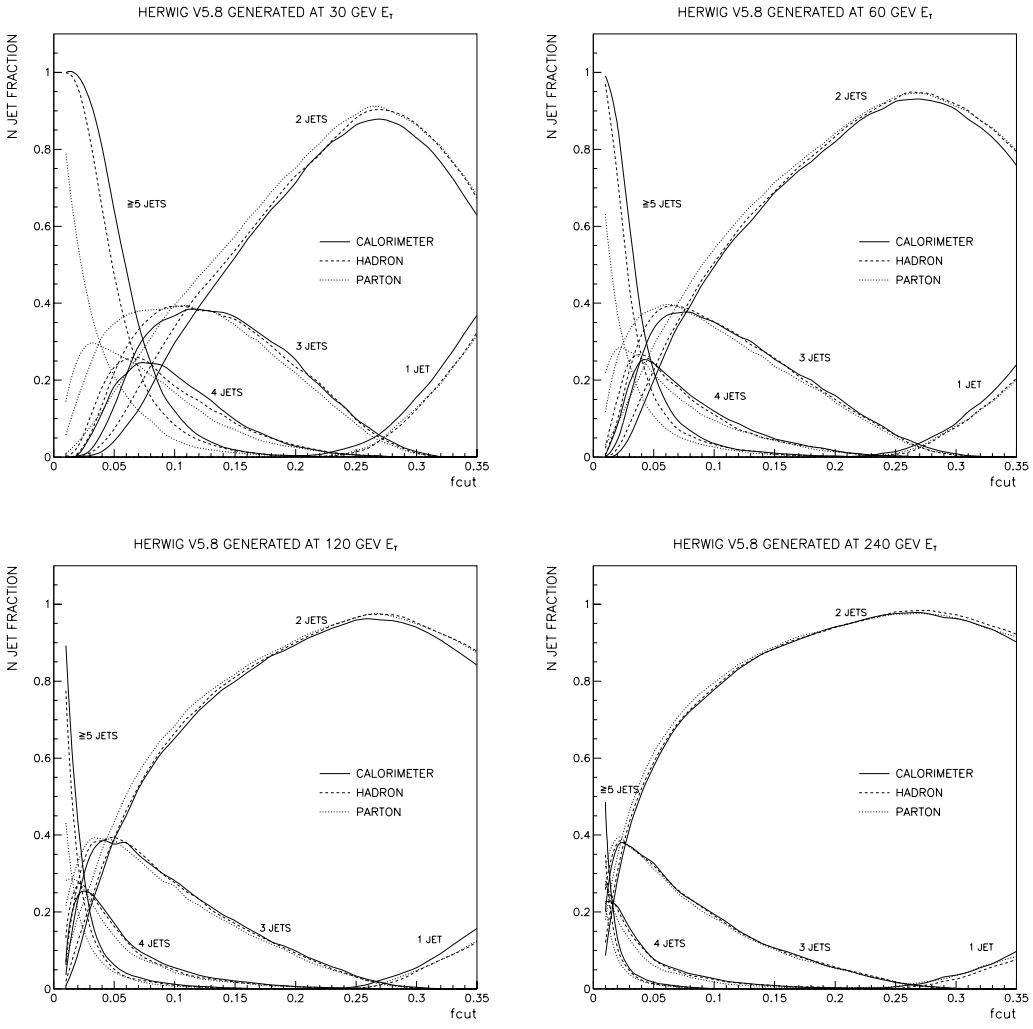

Figure 5.5: $k_\perp$ Jet Rates as a function of f_{cut} in Herwig v5.8 Monte Carlo Data.

Chapter 6

Introduction to $k_\perp$ Jet Momentum Calibration

An accurate calibration of $k_\perp$ jet momentum is not only necessary for a measurement of R_{32}, but it is necessary for almost all analyses involving $k_\perp$ jets. Because a variety of studies will depend on this work, it is important that the correction we derive be widely applicable. It will also be useful to have an understanding of the individual uncertainties and correlations associated with the various aspects of the $k_\perp$ jet momentum calibration.

Deriving a momentum correction for $k_\perp$ jets was an unexpectedly difficult assignment and as a result, we were unable to complete our analysis of R_{32}. In many ways, the calibration of the $k_\perp$ jet algorithm represents a much larger contribution to the field than the measurement of R_{32} (had we completed it). Many subsequent measurements will rely on the work decribed in the following chapters.

We will give a general overview of the jet momentum scale for $k_\perp$ jets. In the

following two chapters, we will give a full description of the offset and jet response corrections. Following that, we will show the results of the Monte Carlo closure test that was performed to test the method, and, finally, we will present the final $k_\perp$ jet momentum scale correction with errors.

6.1 General Overview of $k_\perp$ Jet Momentum Calibration

Almost all analyses involving the physics of jets attempt to relate the observed jets to a simple parton interaction. Precise calibration of measured jet momentum, therefore, is a priority. This is not a straightforward task as the evolution from partons to jets of hadrons to clusters of energy in the calorimeter is very complex and riddled with theoretical unknowns and detector effects.

The jet momentum scale correction is an attempt to remove effects of the detector as well as the physics underlying event (momentum due to soft interactions between the remnant partons of the proton and antiproton). The goal is to approximate the sum of all the final state particle momenta incorporated into a jet resulting from the hard parton interaction. Hadronization effects are not corrected for here. The analysis described in the following chapters is an attempt only to correct jets to the particle (final state hadrons) level.

The method for correcting $k_\perp$ jet momentum is done in two steps. First an offset is subtracted and then a response scaling factor is applied. This can be expressed

by the following relation

$$P_{jet}^{ptcl} = \frac{P_{jet}^{meas} - E_O(\eta, \mathcal{L}, P_T)}{R_{jet}(\eta, P)} \ , \tag{6.1}$$

where P_{jet}^{ptcl} represents the "true" momentum of a jet found from final state particles using the $k_\perp$ algorithm, E_O denotes an offset correction and R_{jet} is a correction for the calorimeter jet response.

Because the definition of a jet is given by the algorithm employed, the calibration will depend on the choice of jet algorithm. To a certain extent, however, the corrections can be derived generally. Previously, the jet energy scale correction was derived for jets defined by the fixed cone jet algorithm [45, 47, 46] and we are able to use the results of that study for detector effects that are independent of the choice of jet algorithm. We also use results of this study to test our method for measuring the offset and for extrapolation into regions of phase space where we lack data for $k_\perp$ jets.

The cone jet energy scale is described in great detail in [45, 46]. Since much of the correction for $k_\perp$ jet momentum is based on that study, we will include it in our discussion emphasizing the material that is relevant to the $k_\perp$ jet momentum scale. From here on, we will refer to the established cone jet energy scale correction as CAFIX5.1 (Calorimeter Fix Package, version 5.1).

Chapter 7

$k_\perp$ Jet Offset Correction

The purpose of the offset correction is to subtract from the reconstructed jet the transverse momentum which is not associated with the hard interaction itself. We divide this into two parts: the offset due to the physics underlying event, O_{ue}, and the offset due to the experimental environment, O_{zb}, such as noise, residual pile-up from previous $p\bar{p}$ crossings and multiple $p\bar{p}$ interactions.

The underlying event contribution comes from soft interactions between the remnant partons of the $p\bar{p}$ pair which did not take part in the hard interaction.

The noise contribution arises because the average energy of the individual cells is not zero (even in the absence of beam) due to uranium decay and electronic noise. Although this is corrected on average by pedestal subtraction, there remains an effect due to zero suppression of cells at readout combined with a non symmetric noise distribution (for further details see [46, 51]).

Pile-up is the residual contribution from previous $\overline{p}p$ crossings. It results from the long shaping time associated with the preamplification stage. The base line

subtractor (BLS) samples the signal before the event and subtracts this amount. The signal from previous crossings continues to decay after this sampling, and, therefore, a residual correction is needed for a more accurate removal of the pile-up effects. The Luminosity has some effect on the amount of signal produced by previous $p\bar{p}$ crossings and therefore, residual pile-up will depend on luminosity.

The multiple interaction contribution is due to soft interactions between other $p\bar{p}$ pairs that do not contribute to the hard collision. This also depends on luminosity. While pile-up and multiple interactions contributions to the offset are luminosity dependent, the noise and underlying event are not.

In this Chapter, we present the offset correction to be applied to jets reconstructed with the $k_\perp$ algorithm. First, we will discuss the method, which is based on MC jets with DØ data overlayed. To test the method, we performed some studies using the 0.7 cone jet algorithm. We compare the results obtained using our method to the previously obtained results from DØ data [45, 46, 51]. This is shown in Appendix B. Finally, we present the results obtained for $k_\perp$ jet offsets, O_{zb} and O_{ue}.

To simulate the offset contribution to jets, we overlay DØ data on Monte Carlo data that has been processed through a DØ detector simulation. The Monte Carlo data do not include the physics underlying event and the detector simulation does not include the effects of noise. Neither are the effects of pile-up nor multiple interaction simulated in the Monte Carlo data. The overlayed DØ data contain these effects, and the offsets are measured by comparing jets in the sample with no overlay to jets with the overlay.

7.1 Monte Carlo Data With Overlay

We use Herwig (version 5.9) Monte Carlo data generated with no underlying event. Monte Carlo data (no underlying event) is generated with $2 \rightarrow 2$ parton E_T thresholds of 30, 50, 75, 100 and 150 GeV. It is processed through the SHOWERLIB [48] detector simulation.

Three different types of DØ data are overlayed on Monte Carlo Data. They are:

ZB *zero bias* data.

ZBnoLØ zero bias data not passing the Level Ø trigger.

MB *minimum bias* data.

The zero bias data, ZB, have the least restrictive trigger requirements. The trigger requires only that a bunch crossing take place and the data are taken at random over a range of instantaneous luminosities, $\mathcal{L}$. The ZBnoLØ data are a subset of the ZB data with the requirement that the event did not pass the level Ø trigger.

ZB data are taken for a range of instantaneous luminosities ($\mathcal{L}$ = 0.1, 3, 5, 10 and 14 $\times 10^{30}\text{cm}^{-2}\text{sec}^{-1}$). The ZB data include the effects of noise, pile-up and multiple interactions. ZBnoLØ and MB data are used only at low luminosity only ($0.1 \times 10^{30}\text{cm}^{-2}\text{sec}^{-1}$). ZBnoLØ data includes the effects of noise and pile-up, and MB data, in addition to noise and pile-up, include the physics underlying event. At low luminosity, very few events pass the Level Ø trigger, and, therefore, ZB and ZBnoLØ are almost identical.

The DØ data (ZB, ZBnoLØ, or MB) is added to the detector information in the

Monte Carlo SHOWERLIB data. As mentioned earlier (4.2.3), in data taking, cells with energy less than 2σ of the pedestal value are zero suppressed (not read out). Therefore, the overlayed data are also zero suppressed (using 0.0 as the pedestal value). We also use the Monte Carlo sample with no overlay. In this case, the calorimeter cells are not zero suppressed prior to reconstruction.

The overlayed and non-overlayed data are reconstructed using version 12 of the reconstruction package (RECO v12). Finally, we reconstruct $k_\perp$ jets from calorimeter cell information as described in section 5.4.

At this time we do not have data covering all luminosities, all jet E_T and all jet η. Shown in Table 7.1 is a summary of the data used in this thesis.

Type of Overlay	Herwig Threshold E_T (GeV)	Luminosity ($\times 10^{30}$cm^{-2}sec^{-1})	Jet η Range
none	30, 50, 75, 100, 150	N/A	$0.0< \|\eta\| <3.0$
ZB	30	5	$0.0< \|\eta\| <3.0$
ZB	30, 50, 75, 100, 150	0.1, 3, 5, 10, 14	$0.0< \|\eta\| <1.0$
ZBnoLØ	30, 50, 75, 100, 150	0.1	$0.0< \|\eta\| <1.0$
MB	30, 50, 75, 100, 150	0.1	$0.0< \|\eta\| <1.0$

Table 7.1: Availability of E_T , luminosity and η for overlayed Monte Carlo data.

7.2 The Method

Let us define the following notation for jets reconstructed from the various data to be used.

xx $k_\perp$ jet E_T in Monte Carlo with no overlay.

$m0$ $k_\perp$ jet E_T in Monte Carlo with MB overlay.

zn $k_\perp$ jet E_T in Monte Carlo with ZBnoLØ overlay.

zL $k_\perp$ jet E_T in Monte Carlo with ZB overlay at luminosity $\mathcal{L} = L \times 10^{30}\text{cm}^{-2}\text{sec}^{-1}$ (e.g. z5 for $\mathcal{L} = 5 \times 10^{30}\text{cm}^{-2}\text{sec}^{-1}$).

As mentioned above, the ZB data include the effects of noise, pile-up and multiple interactions. This contribution to a jet at a given luminosity, O^L_{zb}, is given by

$$O^L_{zb} = zL - xx. \tag{7.1}$$

The MB data include the effects in ZBnoLØ plus underlying event. Thus, the offset due to underlying event can be measured by

$$O_{ue} = m0 - zn. \tag{7.2}$$

These subtractions are performed on a jet by jet basis, for the two leading jets. We ensure the same jet is selected in both samples by requesting them to be within a distance of 0.5 in $\eta - \phi$ space. Figure 7.1 shows the distribution of distances, $R_{min} = [(\phi_{z5} - \phi_{xx})^2 + (\eta_{z5} - \eta_{xx})]^{1/2}$, from the leading xx jet to the closest jet in the $z5$ sample.

Figure 7.2 shows a typical distribution of the energy difference between corresponding jets in the noise overlayed ($z5$ in this case) and no noise sample, xx. From the mean and RMS of this distribution we extract the offset and its statistical error.

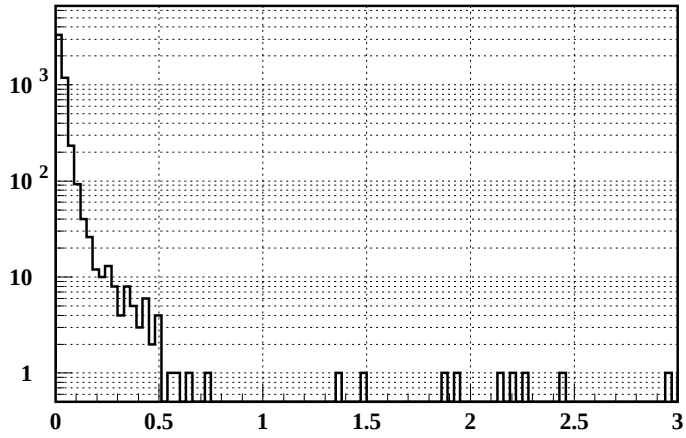

Figure 7.1: Distance in $\eta - \phi$ space from the leading xx $k_\perp$ jet to the closest $z5$ $k_\perp$ jet.

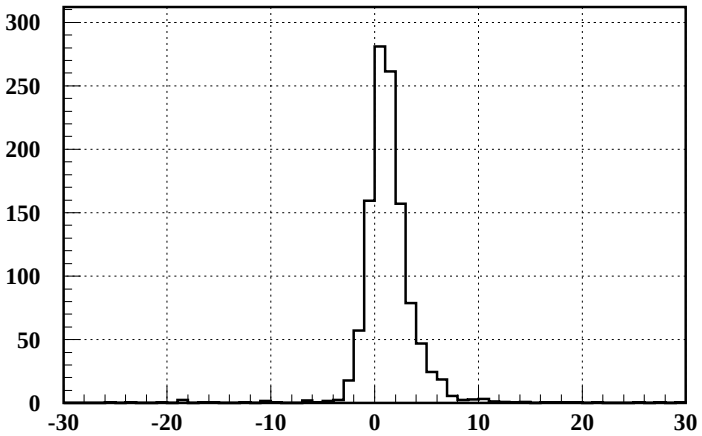

Figure 7.2: Distribution of E_T differences between corresponding $k_\perp$ jets in the $z5$ and xx samples

Note that leading jets in one sample do not always correspond to leading jets in the other. Figure 7.3 plots the E_T ranking number of the $z5$ jet associated to the two leading xx jets (jets are numbered in decreasing order according to their E_T). Besides the expected swapping between the leading two jets due to fluctuations in the overlayed noise, we sometimes find one of the leading xx jets to be associated with a lower energy $z5$ jet. To reduce the effects of E_T smearing, the events are weighted

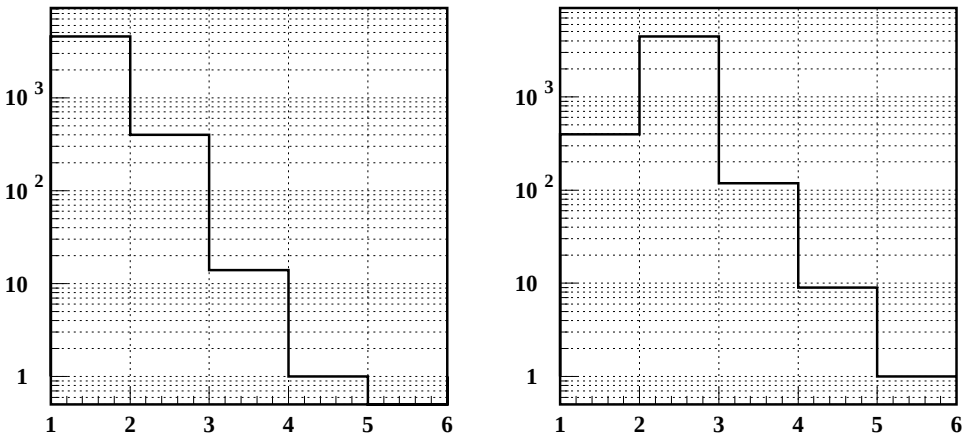

Figure 7.3: Ranking of overlayed $k_\perp$ jets compared to non-overlayed jets. Corresponding $z5$ $k_\perp$ jet matched to the leading (*left*) and second leading (*right*) xx $k_\perp$ jet. Jets are numbered in decreasing order according to their E_T .

so that we have a flat jet E_T distribution. The $k_\perp$ jet E_T distributions without weighting are shown in Figure 7.4. By using a flat distribution, we eliminate uneven contributions in a given jet E_T bin due to the steeply falling and rising distributions shown in Figure 7.4. This is discussed in more detail with respect to the 0.7 cone jet algorithm in Appendix B.

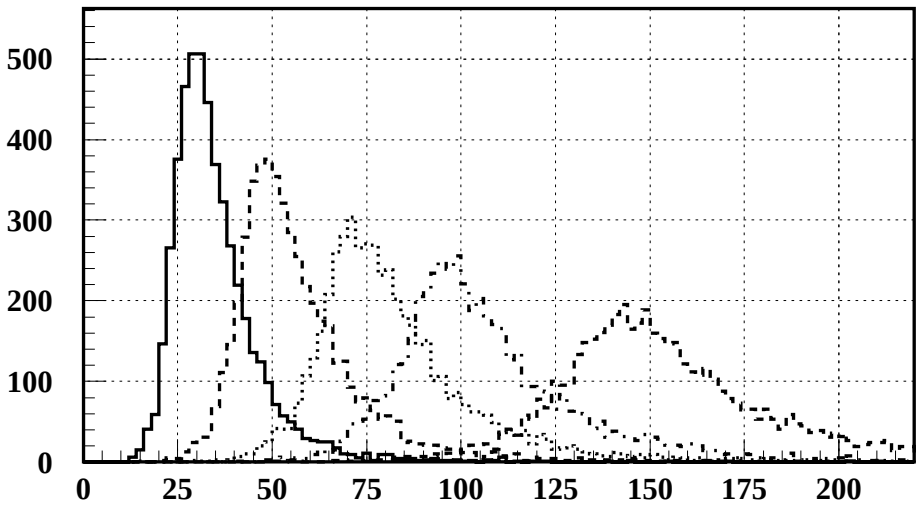

Figure 7.4: Distribution of reconstructed E_T for $k_\perp$ jets without noise overlay. The different line types correspond to samples generated with parton E_T thresholds of 30, 50, 75, 100 and 150 GeV.

7.3 Verification of the Overlay Method

To ascertain whether the overlay method models the contributions to the offset correctly, we compare the occupancies in 0.7 cone jets from our Monte Carlo with MB overlay sample to the occupancies measured in jets in a pure MB sample. Figure 7.5 shows the occupancies measured in 0.7 cone jets taken from pure MB data, and Figure 7.6 shows the occupancies in Monte Carlo with MB overlay data. We are only able to compare for $|\eta|$ <1.0, and the y-axis scales are dramatically different. However, under close examination, one can see that the occupancies for a given jet E_T are in good agreement with the exception for jet $E_T \leq$40 GeV.

In an attempt to further our understanding and confidence in the overlay method, we measured the offsets, O_{zb} and O_{ue}, for cone jets ($R = 0.7$) and compared our measurement to the previous correction derived for 0.7 cone jets in the CAFIX5.1

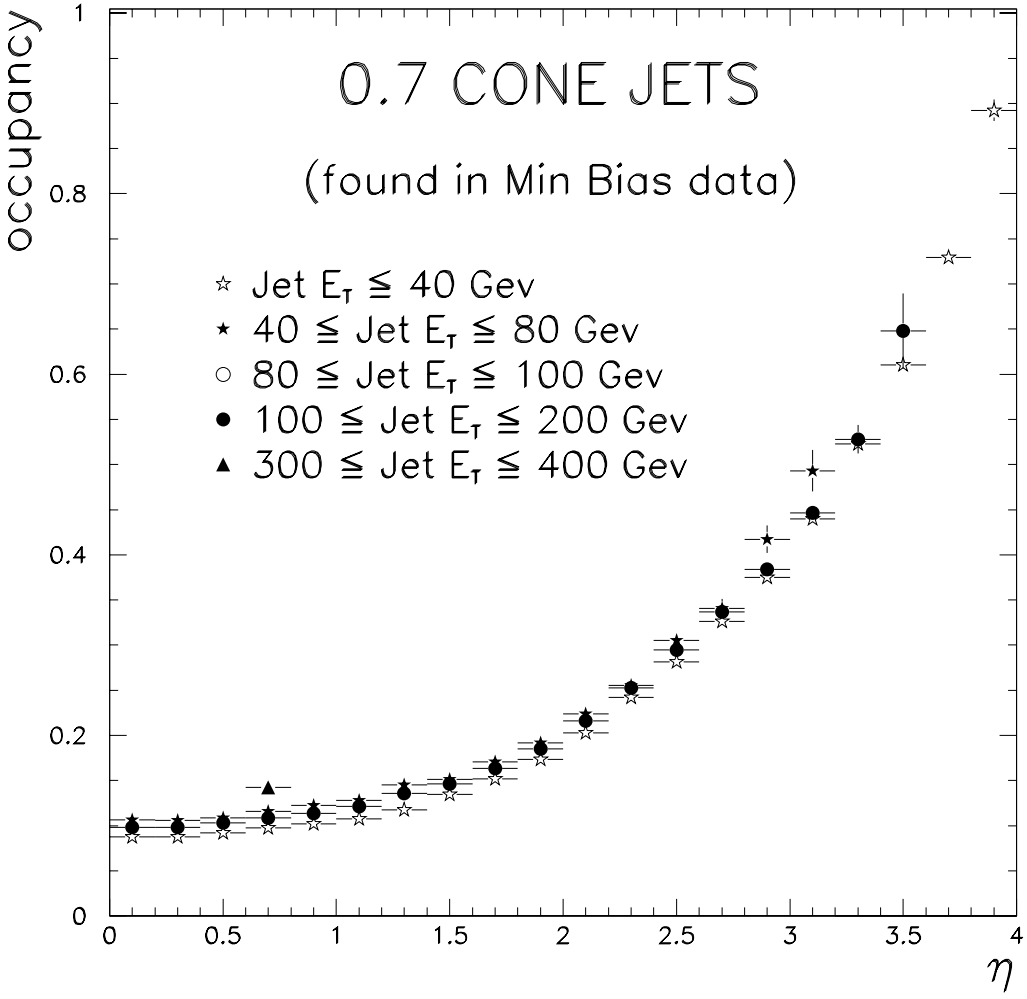

Figure 7.5: 0.7 cone jet occupancy vs. jet η for jets found in minimum bias data.

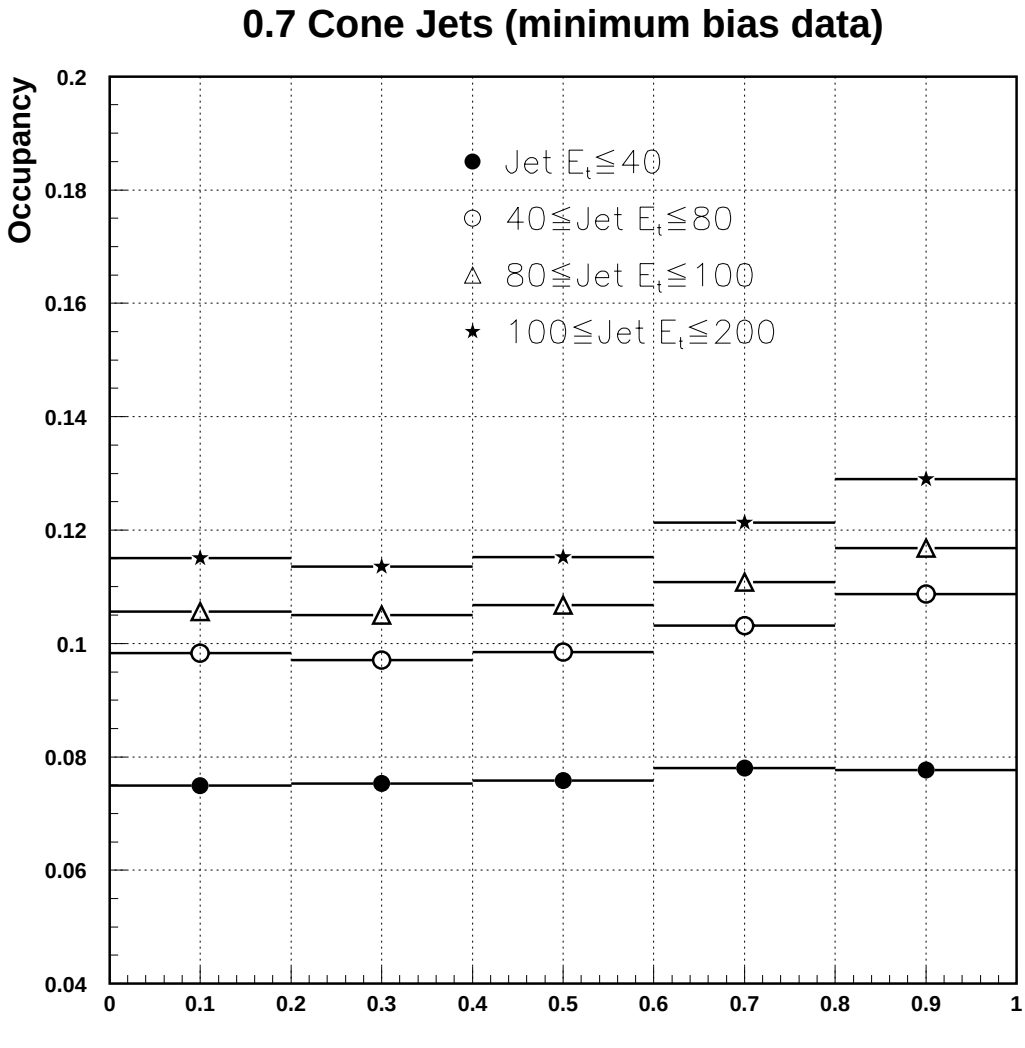

Figure 7.6: 0.7 cone jet occupancy vs. jet η for jets found in Monte Carlo with minimum bias overlay data.

correction package [51, 45, 46]. In that study, the densities were measured in ZB, ZBnoLØ, and MB events. The offsets were derived by multiplying densities by the area of a fixed cone jet, $\pi \times (0.7)^2 \sim 1.5$.

In order to compare to the CAFIX5.1 offsets, we measure the offset densities, D_{ue} and D_{zb}, by dividing the offsets, O_{ue} and O_{zb}, by the area of a 0.7 cone jet. This study is described in detail in Appendix B. For the offset due to noise, pile-up and multiple interactions, we compared for only one luminosity, $\mathcal{L} = 5 \times 10^{30} \mathrm{cm}^{-2} \mathrm{sec}^{-1}$.

Our results for the offset due to underlying event, D_{ue}, are consistent with CAFIX5.1 (see Figure B.4). For D_{zb}, on the other hand, we see a dependence on 0.7 cone jet E_T which was not prescribed in the CAFIX5.1 correction (see Figure B.2. We believe the E_T dependence that we see is due to zero suppression effects that were not accounted for in the CAFIX5.1 correction. The zero suppression correction used in CAFIX5.1 (Equation B.1) depends on the occupancy factor, F_{zb} in jets. The occupancy for jets was seen to have little dependence on jet E_T and, therefore, a constant occupancy was assumed. If instead we use the small variation in occupancy shown in Figure B.5 in the CAFIX5.1 zero suppression correction, we can explain only 30% of the 0.7 cone jet E_T dependence that we measure with the overlay method.

Because our occupancies for given jet E_T agree with pure MB data, we believe the overlay correctly models the effects of underlying event, noise, pile-up and multiple interactions. It is possible that the zero suppression correction used in CAFIX5.1 is inexact. Because the effects of zero suppression were not well understood when CAFIX5.1 was derived, a large error was assigned. This error accommodates the

discrepancy between our measurement and the CAFIX5.1 value. Because the E_T dependence for 0.7 cone jets cannot be confirmed with pure DØ data, we assign an error to O_{zb} for $k_\perp$ jets. As stated above, 30% of the effect is consistent with CAFIX5.1. The other 70% will be assigned as a systematic error to our measurement for the offset, O_{zb}, for $k_\perp$ jets.

7.4 Offsets for the $k_\perp$ Algorithm

At this time we do not have data covering all luminosities, all jet E_T and all jet η. Shown in Table 7.1 are the data available at this time. In the regions where we do not have data, we will either extrapolate using the data that we have or use offset corrections from CAFIX5.1.

7.4.1 Offset Due to Noise, Pile-Up and Multiple Interactions

As stated above, we measure the offset due to noise, pile-up and multiple interactions using the relation,

$$O_{zb}^{L} = zL - xx \ . \tag{7.3}$$

Figs. 7.7 and 7.8 present the results for O_{zb} as a function of E_T at $\mathcal{L} = 0.1 \times 10^{30}\text{cm}^{-2}\text{sec}^{-1}$ and $\mathcal{L} = 5 \times 10^{30}\text{cm}^{-2}\text{sec}^{-1}$, respectively. As opposed to the cone case (see Appendix B), very little E_T dependence is observed for the $k_\perp$ algorithm and this dependence becomes weaker as the luminosity increases. Exponential fits were done for luminosities lower than $\mathcal{L}$=$5\times10^{30}\text{cm}^{-2}\text{sec}^{-1}$.

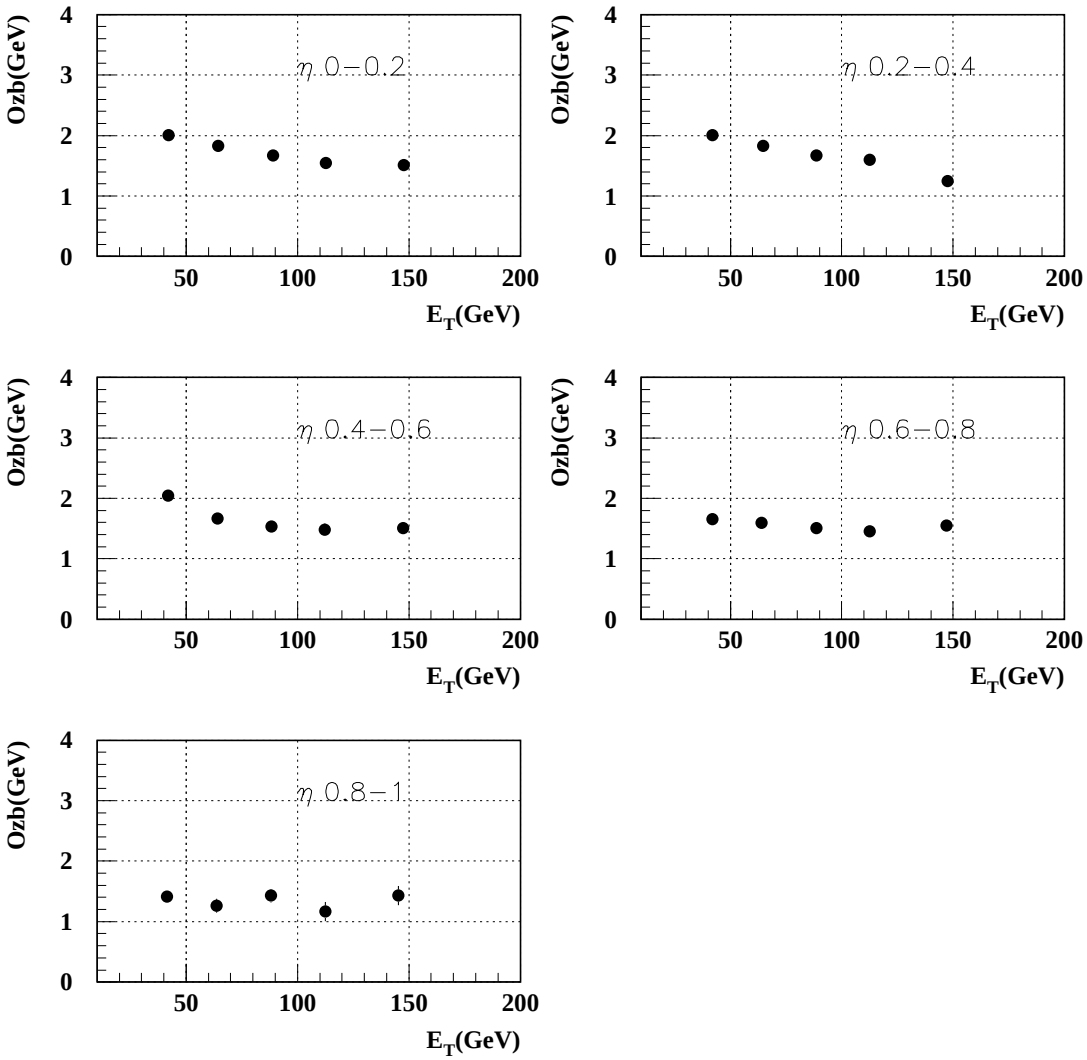

Figure 7.7: Measured O_{zb} vs. $k_\perp$ jet E_T at $\mathcal{L}$=0.1×10^{30}cm^{-2}sec^{-1}.

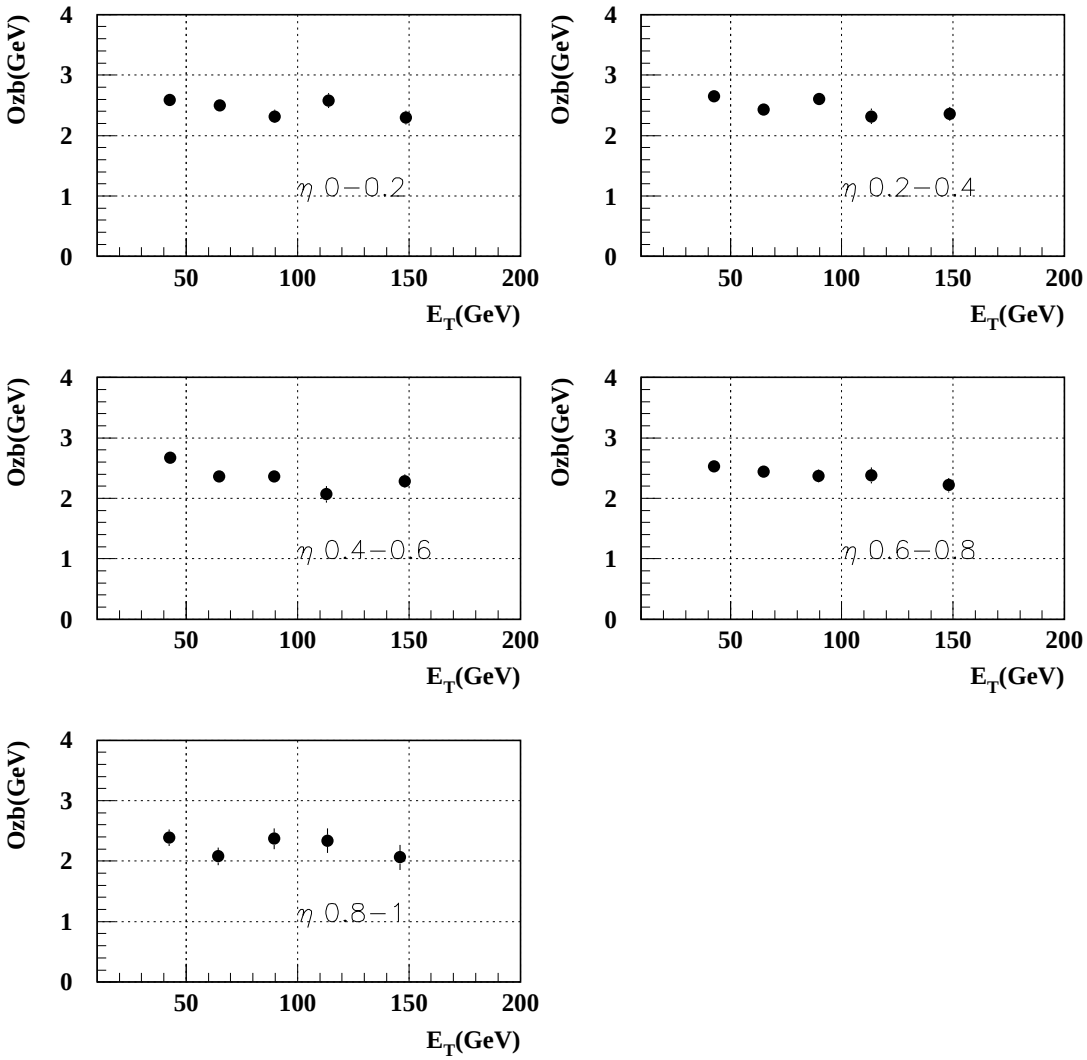

Figure 7.8: Measured O_{zb} vs. $k_\perp$ jet E_T at $\mathcal{L}$=5×10^{30}cm^{-2}sec^{-1}.

The study of η and luminosity dependence for the central region is summarized in Figure 7.9. The general trend is that $k_\perp$ offsets are 50-75% larger than for cone. Because the $k_\perp$ algorithm clusters everything into jets, we would expect it to "pull" in more noise and underlying event than a fixed cone algorithm (which excludes energy outside the cone radius).

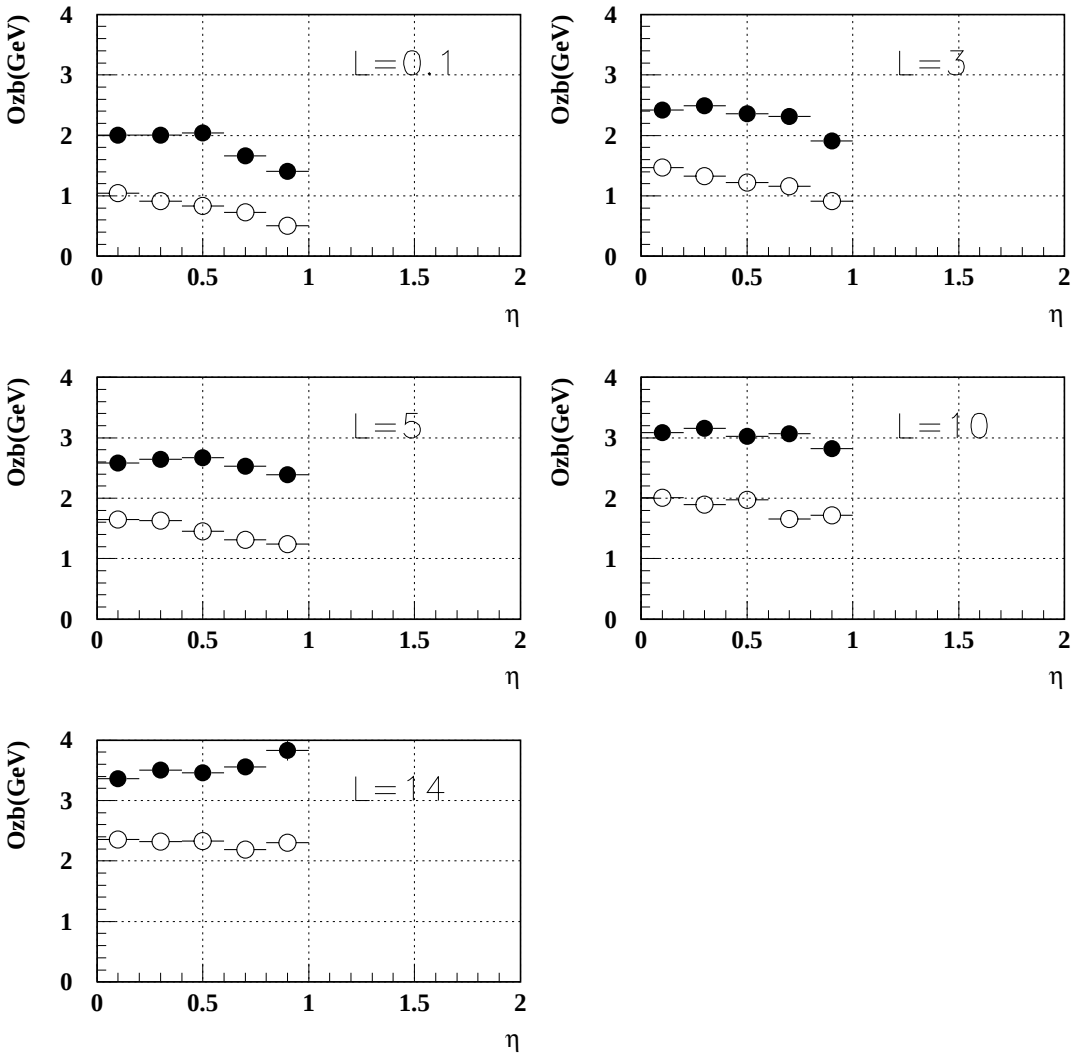

Figure 7.9: O_{zb} offset vs η for $k_\perp$ jets with 30<E_T <50 GeV. The result for cones (open circles) is shown for comparison.

To study the full rapidity range, we use a high statistics sample generated with

Herwig v5.9 with the underlying event included. This sample was only generated in the low energy range, E_T >30 GeV, and overlayed with ZB data with $\mathcal{L}$=5×10^{30}cm^{-2}sec^{-1}. The Underlying event essentially cancels when taking the difference $z5$-xx. Results are shown in Figure 7.10, for non overlayed jets with 30<E_T <50 GeV.

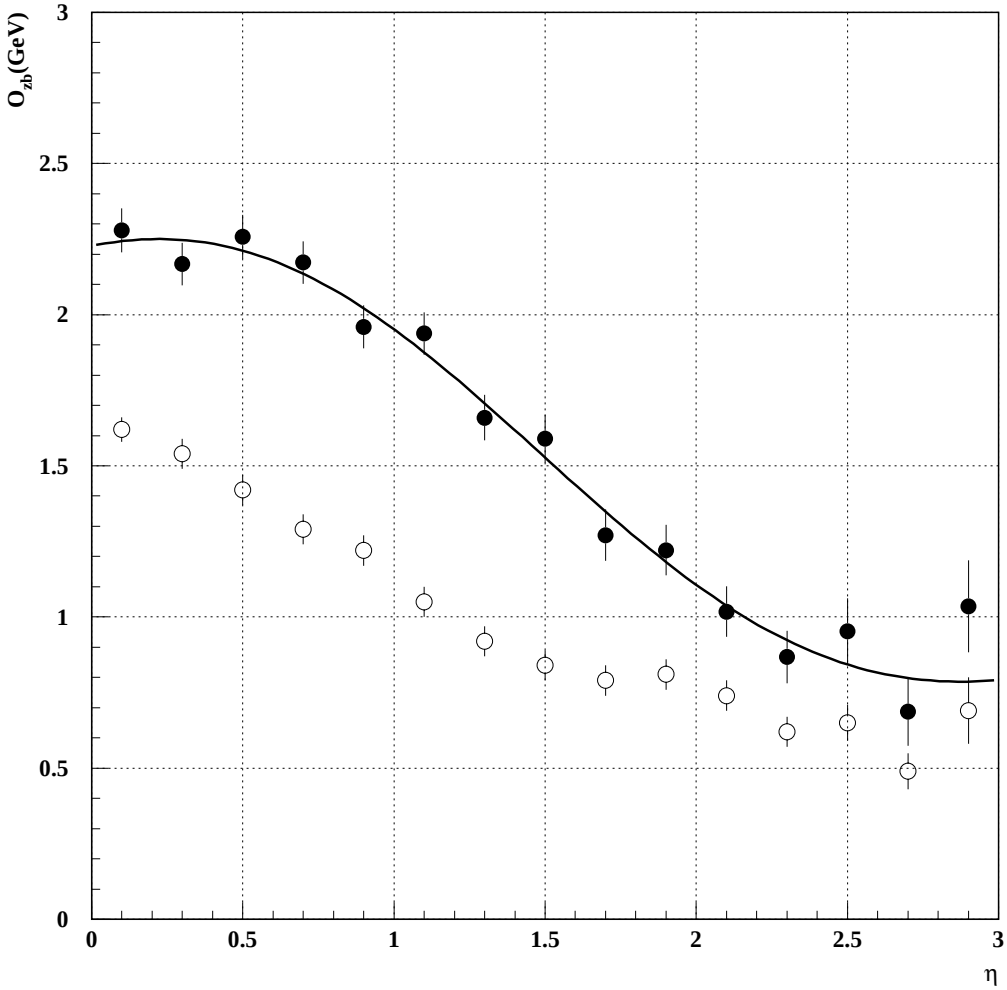

Figure 7.10: Measured O_{zb} vs. η for $k_\perp$ jets at $\mathcal{L}$=5 and 30<E_T <50 GeV (solid symbols). The result for cones is shown for comparison (open symbols).

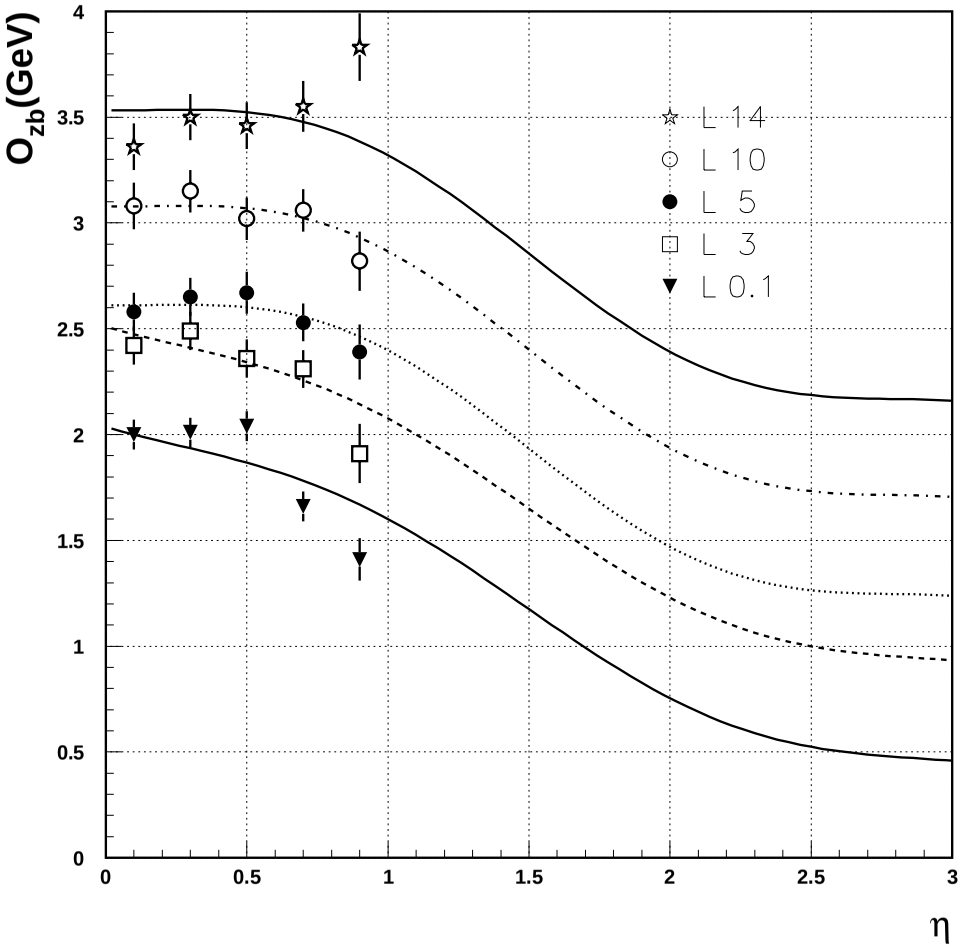

Figure 7.11: Parametrization of O_{zb} vs. $k_\perp$ jet η for jets with $30<E_T<50$ GeV, for various luminosities.

Since there is no MC available to get the offsets beyond the central region for luminosities other than $\mathcal{L}$=5, we estimate their values by extrapolating the measured central values (Figure 7.9) with a functional form as suggested by the fit shown in Figure 7.10.

In order to let all the points participate in the fit, the samples were divided in two groups according to their luminosity (lower and greater than $\mathcal{L}$=5). Two new distributions are obtained by making an average of the points after normalizing to the $\mathcal{L}$=5 distribution. The fits to these distributions were scaled with luminosity,

and the results are shown in Figure 7.11. Linear interpolation is used for luminosities between the values shown in Figure 7.11.

To get the final O_{zb}, these values must also be given an E_T dependence at low luminosity. This dependence is interpolated using a third degree polynomial between $\mathcal{L}$=0.1 and $\mathcal{L}$=5 so that at $\mathcal{L}$=0.1, the dependence is as shown in Figure 7.7 and flat above $\mathcal{L}$=5.

Figure 7.12 shows the final O_{zb} vs. E_T for 3 luminosities $\times$ 3 η values (with errors). Figure 7.13 shows the η dependence of O_{zb} for 2 values of $k_\perp$ jet E_T and 2 luminosities.

The error arising from the disagreement in the E_T dependence between our results of O_{zb} for cone jets and those shown in [45] is one of the major sources of uncertainty especially at high energies and low luminosities (around 15%). The functional form of O_{zb} contributes an error of 0.2 GeV (calculated as the average of the largest difference between the points and the fits for each curve in Figure 7.11). To accommodate the uncertainty for energies greater than 200 GeV, we introduce an additional uncertainty that rises smoothly from 0.0 to .2 GeV between 120 GeV and 270 GeV and remains flat above 270 GeV.

7.4.2 Offset Due to Physics Underlying Event

We measure the offset due to underlying event using the relation,

$$O_{ue} = m0 - zn. \tag{7.4}$$

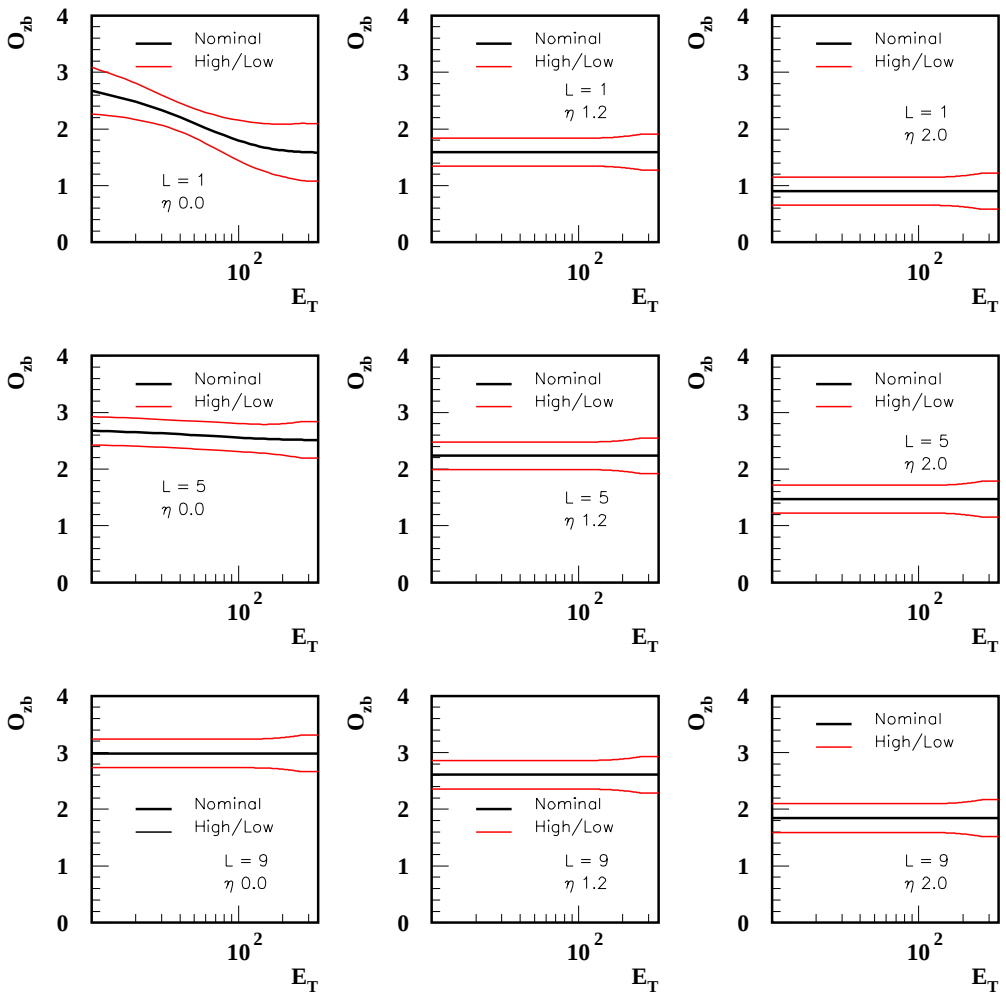

Figure 7.12: O_{zb} E_T dependence and errors, for $k_\perp$ jets at $\mathcal{L}$=1,5 and 9 and η =0.0, 1.2, and 2.0.

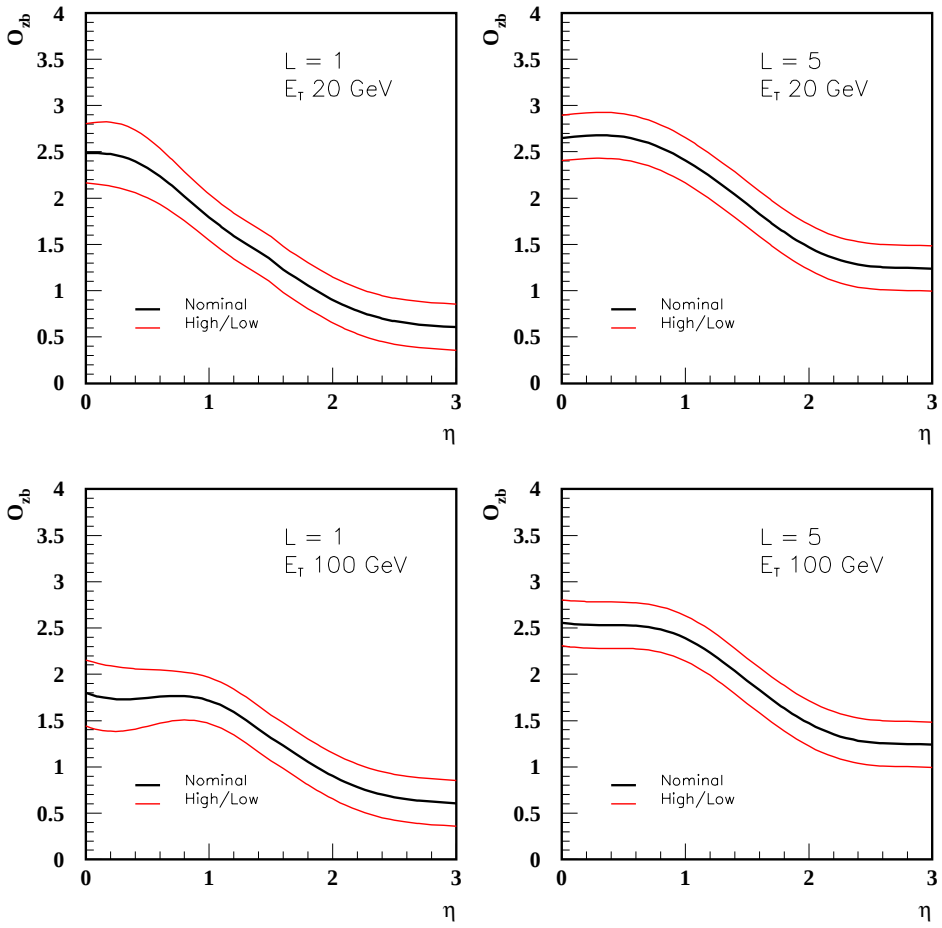

Figure 7.13: O_{zb} η dependence and errors for $k_\perp$ jets with jet E_T equalling 20 and 100 GeV at $\mathcal{L}$=1 and $\mathcal{L}$=5.

Figure 7.14 shows the physics underlying event offset, O_{ue}, compared to the previous result for cone. As shown in B, there is no evidence of an E_T dependence for 0.7 cone jets, and we do not see an E_T dependence for $k_\perp$ jets. Therefore we will apply a correction only as a function of η.

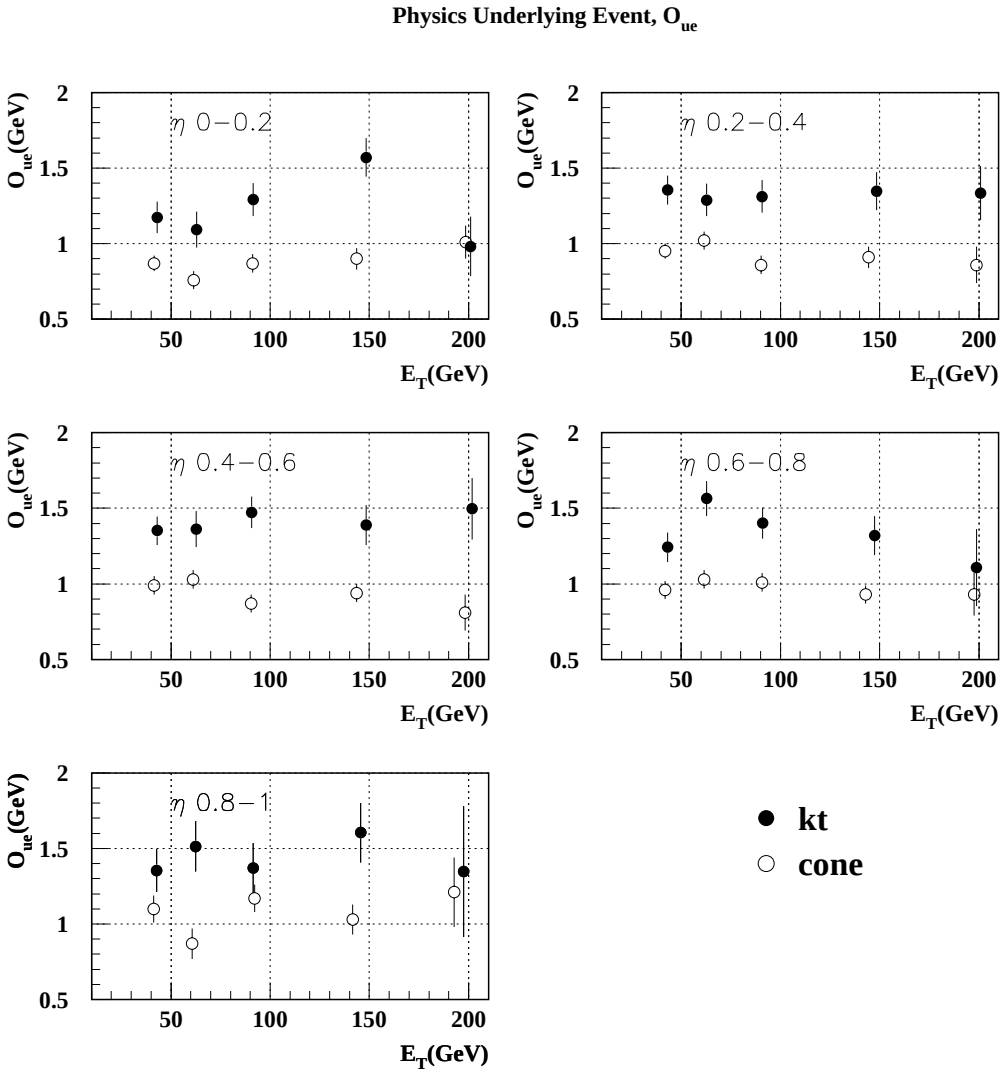

Figure 7.14: Measured O_{ue} vs E_T for $k_\perp$ jets. The result for cones is shown for comparison.

Figure 7.15 summarizes the results in O_{ue} for $k_\perp$ and for cone jets as a function of jet η compared to the offset given by CAFIX5.1. Unfortunately, there is no MC available to get the offsets beyond the central region. Therefore we must use the

CAFIX5.1 result to determine the η dependence. Figure 7.15 shows O_{ue} for $k_\perp$ jets for $|\eta|$ <1.0 compared to O_{ue} given by CAFIX5.1 and the measured 0.7 cone O_{ue} (from Monte Carlo data with overlay). The good agreement in the central region between our results for cone jets and those from CAFIX5.1 reinforces our confidence in the overlay method. O_{ue} is consistently larger for $k_\perp$ jets than it is for cone jets. We normalize the CAFIX5.1 offset to our measurement for the 0.7 cone jets. Then, we calculate the average difference between our measurements for the $k_\perp$ and cone jet offsets. We add this difference to the normalized CAFIX5.1 points to get the offset due to underlying event for $k_\perp$jets. The final underlying event offset, O_{ue} with errors is shown in Figure 7.16.

We apply a 0.1 GeV statistical error that comes from the normalization process described above. There is a systematic error of 0.1 GeV to accommodate possible E_T dependence (from Figure 7.14). Added in quadrature, this gives us about a 10% error in the region $|\eta|$ <1.0. We will inflate this to 15% above $|\eta|$ >1.0 where we have not measured O_{ue} for $k_\perp$ jets. The O_{ue} correction for $k_\perp$ jets (with errors) is shown in Figure 7.16.

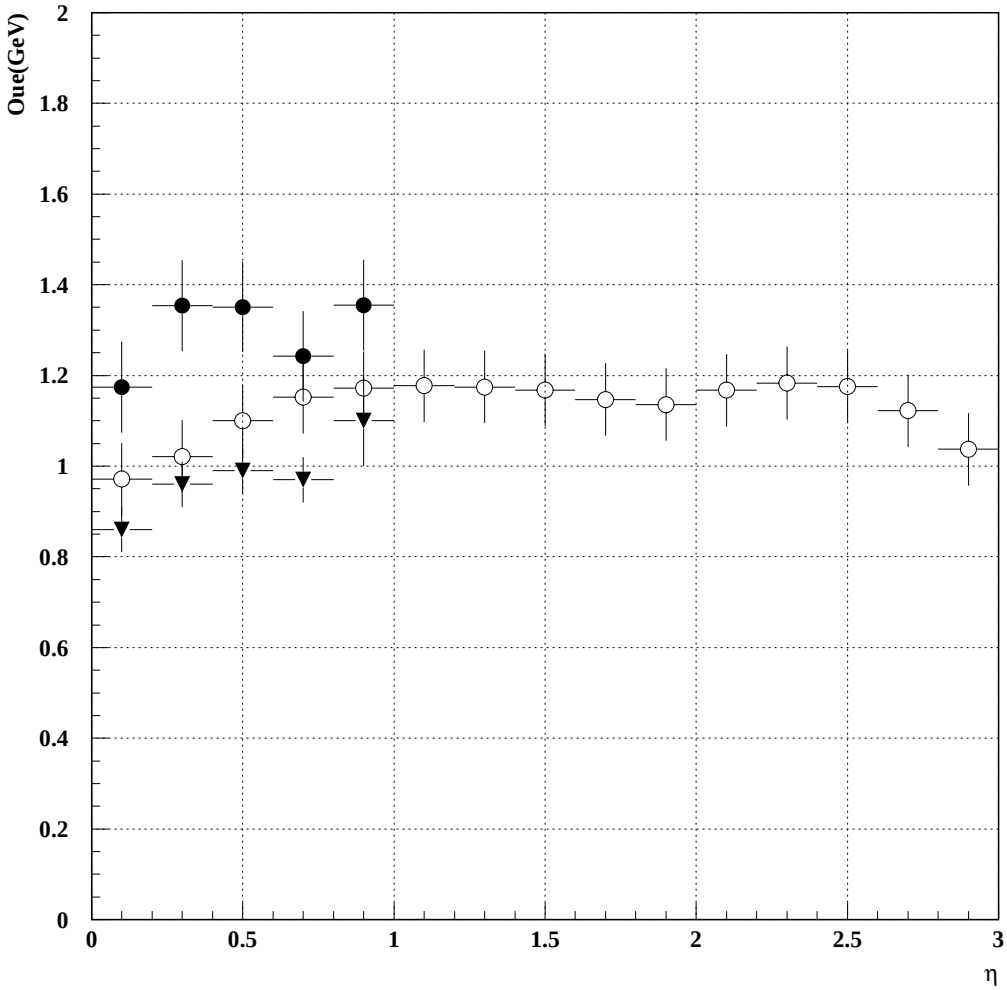

Figure 7.15: Measured O_{ue} vs $k_\perp$ jet η (solid circles) and cone jets η (triangles), together with the results from the CAFIX5.1 (open circles).

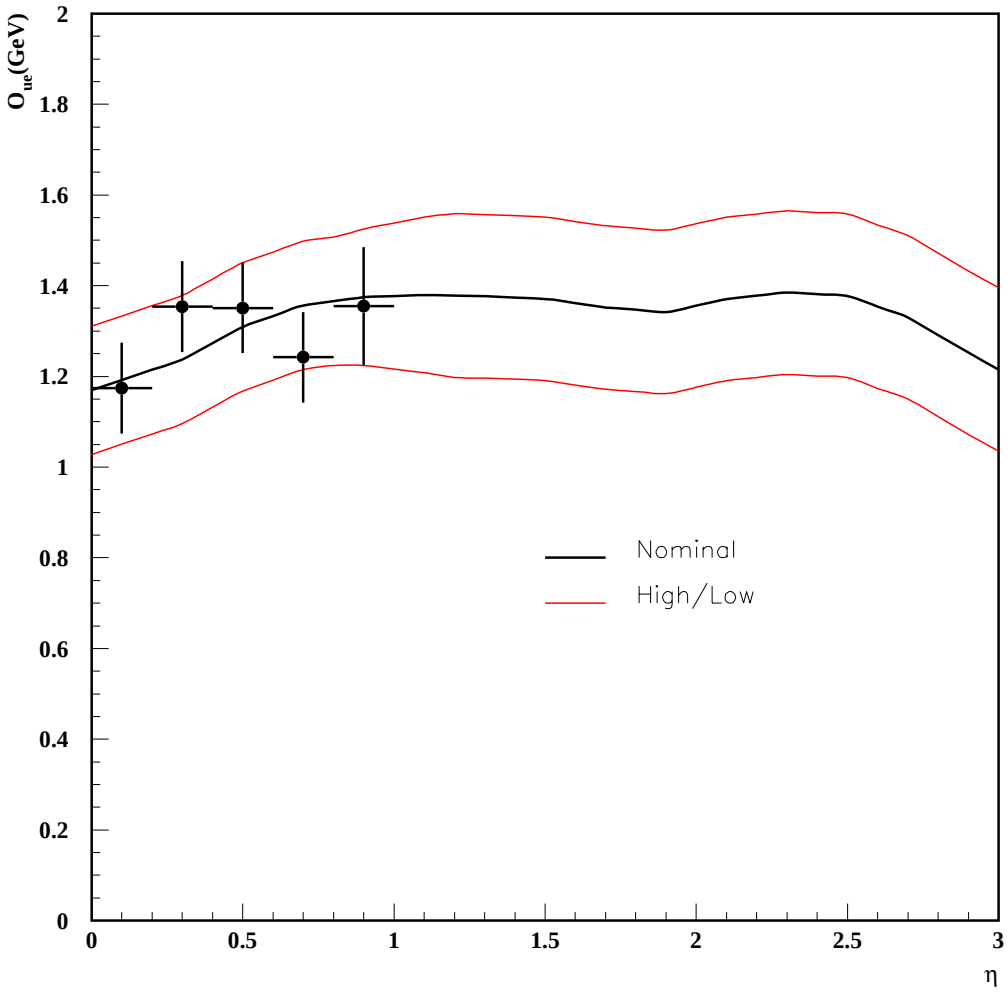

Figure 7.16: O_{ue} correction vs $k_\perp$ jet η. The points show the measured offset for $k_\perp$ jets.

Chapter 8

$k_\perp$ Jet Response Correction

The calorimeter is calibrated from Test Beam data based on charge deposition in the liquid argon for known incident particle energies. In theory, the true jet momentum and energy would simply be the vector sum of the energy deposited in the calorimeter. In reality, however, the measured jet energies are reduced due to energy losses in uninstrumented regions of the detector, variations in cryostat response to single particles (e.g. non-linear response for low energy particles), and variations in the e/π response ratio [46].

The calorimeter response to jet momentum was measured for fixed cone jets [45, 46]. There, the jet response is used to correct the scalar summed cone jet energy, E. We correct vector summed $k_\perp$ jet momentum, $P_{Kt\ jet}$. The method relies on transverse momentum (P_T) balance. It is, therefore, applicable to jet momentum. One would expect the jet response to be identical for momentum and energy. However, calorimeter showering effects widen jets, causing the vector summed momentum and scalar summed energy to require different corrections. This is discussed in more

detail in Appendix C.

The jet response correction is described in 7 sections:

1. The Missing E_T Projection Fraction (MPF) Method.
2. Cryostat Factor Correction.
3. $E' \rightarrow P_{kt}$ Mapping.
4. Jet Response vs. P_{kt}.
5. Low P_{kt} Jet Response.
6. ICR Correction.
7. Jet Response Errors.

8.1 The Missing E_T Projection Fraction Method

R_{jet} is measured using γ-jet momentum balance in the transverse plane. To do this, we use the missing transverse energy projection fraction (MPF) method. The missing transverse energy, $\vec{\not\!\!E}_T$, is the vector momentum necessary to balance the entire event in the transverse plane. Its x and y components are given by

$$\not\!\!E_{Tx} = -\sum_{i=1}^{n} P_{xi} \quad \text{and} \quad \not\!\!E_{Ty} = -\sum_{i=1}^{n} P_{yi} \ , \tag{8.1}$$

where P_{xi} and P_{yi} are the x and y components of 4-momenta assigned to each calorimeter cell (assumed massless).

In an ideal detector, there would be no energy losses and, therefore, $\not\!\!E_T$=0.0,

$$\vec{\not\!\!E}_T = -\left(\vec{P}_{T\gamma} + \vec{P}_{T\ had}\right) = 0\ , \tag{8.2}$$

where $\vec{P}_{T\ had}$ is the vector sum of the hadronic recoil in the transverse plane. In reality, the electromagnetic and hadronic responses are not unity and are measured as

$$\vec{P}^{meas}_{T\gamma} = R_{em}\vec{P}_{T\gamma} \quad \text{and} \quad \vec{P}^{meas}_{T\ had} = R_{had}\vec{P}_{T\ had}\ . \tag{8.3}$$

$\vec{\not\!\!E}_T$ is not zero and is now given by

$$\vec{\not\!\!E}_T = -\left(R_{em}\vec{E}_{T\gamma} + R_{had}\vec{E}^{had}_T\right) \neq 0.0\ . \tag{8.4}$$

The electromagnetic scale, R_{em}, is determined very accurately. Therefore, after the photons are calibrated, $\vec{\not\!\!E}_T$ is given by

$$\vec{\not\!\!E}_T = -\vec{E}_{T\gamma} - R_{had}\vec{E}^{had}_T. \tag{8.5}$$

From Equation 8.2, $\vec{P}_{T\ had} = -\vec{P}_{T\gamma}$, and we can write

$$\vec{\not\!\!E}_T = \vec{E}_{T\gamma}\left(R_{had} - 1\right). \tag{8.6}$$

Hence, the hadronic response can be measured using

$$R_{had} = 1 + MPF = 1 + \frac{\vec{\not\!\!E}_T \cdot \hat{n}_{T\gamma}}{E_{T\gamma}}, \tag{8.7}$$

where $\hat{n}_{T\gamma}$ is the unit vector for the transverse component of the photon's momentum.

Given that the event is balanced in transverse momentum, this gives the momentum fraction the jet measurement has lost due to imperfections in the calorimeter.

8.1.1 The Energy Estimator, E'

Ultimately, we would like to know the response as a function of jet momentum. However, resolution effects and reconstruction biases make the uncorrected jet momentum a poorly measured quantity. In order to avoid problems that may arise from this, we look at the response as a function of a well measured quantity that is strongly correlated with the true momentum of the jet of particles, P_{jet}^{ptcl}.

At leading order a $\gamma-$jet event should be balanced in P_T. Using this and the relation, $sin\theta = 1/cosh\eta$, the ideal energy of the jet, E', is given by

$$E' = E_{T\gamma}^{meas} cosh(\eta_{jet}) \ . \tag{8.8}$$

The response can then be converted to a function of $k_\perp$ jet momentum by mapping E' to $k_\perp$ jet P.

The response was derived as a function of cone jet energy in CAFIX 5.1. Only the position of the jet is used to define the response as a function of E'. We use $k_\perp$ jet momentum, P_{kt}, because the mpf method is based on momentum balance.

8.2 γ-Jet Data

The jet response was measured previously as a function of E' using fixed cone jets ($R = 0.7$) [45, 46]. To obtain a correction for $k_\perp$ jet momentum, we must provide a mapping of E' to P_{kt}. To do this, we use a subset of the data used to derive R_{jet} versus E'. Below we describe the criteria applied to the γ-jet data for measuring the jet response using cone jets. Some additional considerations were necessary for deriving the jet response correction for $k_\perp$ jets, and we discuss these issues below.

8.2.1 Photon Event Requirements

In order to measure the jet response, we require a jet to be balanced by a well calibrated object. In Section 4.2.3, we noted that the electromagnetic calorimeter is very well calibrated for electrons and pions above a certain threshold. Therefore, we do not actually require a pure photon sample, but we need an energetic, isolated, electromagnetic cluster. So, although we use events passing triggers designed to accept direct photons, we use different offline criteria to select events. Since the majority of these electromagnetic clusters are indeed photons, throughout this thesis, we will refer to them as *photons*.

Photon triggering is described in Appendix A.

Here is a list of the general offline criteria for the events used in our photon data.

- We select events with low instantaneous luminosity, $\mathcal{L} < 5\times10^{30}\text{cm}^{-2}\text{sec}^{-1}$.

- A multiple interaction tool, MITOOL, uses information from the level Ø, track-

ing, and calorimeter detectors to distinguish between events where one or more interactions took place. We select events flagged by the MITOOL as having only one interaction.

- $E_{T\gamma}$ must be greater than the trigger threshold plus one $\sigma_{E_{T\gamma}}$, where $\sigma_{E_{T\gamma}}$ is the photon energy resolution.

- Where multiple photon triggers are running at once, a high E_T threshold cut prevents a photon event from passing a lower threshold trigger and fail a higher threshold trigger. This removes photons which fluctuated to a very high energy in the calorimeter.

- Longitudinal and transverse isolation cuts demand that the EM cluster not be contaminated by hadronic activity.

- Events with photons within 0.01 radians of a ϕ crack in the calorimeter are rejected.

- Photons in the inter cryostat region (ICR) are avoided by demanding that $|\eta_\gamma| < 1.0$ or $1.6 < |\eta_\gamma| < 2.5$.

- Events are discarded if there is main ring activity at the time of the event. A portion of the main ring accelerator goes through the calorimeter. When the main ring is active, radiation leaks into the detector.

- One and only one vertex must be found, and the z-vertex of the event must be within 70 cm of the center.

- Events where a *noisy* cell was removed are discarded. During reconstruction, cells with a disproportionate amount of energy compared to their neighbors are removed by the AIDA (Anomalous Isolated Deposit Algorithm) software.

- For $E_{T\gamma} < 30$ GeV, we demand that no muon be detected. Otherwise, we demand that any muons detected have $P_{T\mu} < 100$ GeV. This is to avoid bremsstrahlung radiated photons from cosmic ray muons.

8.2.2 Cone Jet Requirements

Here is a list of the general offline criteria for 0.7 cone jets in our γ-jet data used to derive the CAFIX5.1 jet response.

- We remove jets whose axes are within 0.25 (in $\eta - \phi$ space) of the photon.

- There must be at least one remaining jet in the event.

- We avoid the ICR by demanding that the leading jet η be contained in the central cryostat, CC, or one of the end cryostats, EC ($|\eta_{jet}| < 0.7$ for CC and $1.8 < |\eta_{jet}| < 2.5$ for EC).

- If the leading jet lies in the EC, we exclude the events where $E_{T,\gamma} < 25.0$ GeV.

- We avoid *fake jets* by demanding that the fractions of jet P_T in the coarse hadronic (CHF) and electromagnetic (EMF) sections of the calorimeter be within reasonable limits:

$$0.05 < \text{EMF} < 0.95$$

$$\text{CHF} < 0.5\,.$$

- The E_T ratio between the highest and the second highest E_T cells in a jet (HCF) are required to be less than 10, HCF<10.

- We require the leading jet and γ to be back to back in ϕ ($2.8 < \Delta\phi < \pi$).

8.2.3 Additional considerations for $k_\perp$ Jets

$k_\perp$ jets were reconstructed for a subset of the γ-jet data described above in order to perform the E' to P_{kt} mapping. We use the same cuts on $k_\perp$ jets that were used for 0.7 cone jets in CAFIX5.1 (above) with the exceptions that we use $k_\perp$ jets in place of cone jets, we require $E_{T\gamma} > 20$ GeV (vs. 25 GeV) for EC jets, and we do not cut on HCF (this information is not available for $k_\perp$ jets).

When the $k_\perp$ jets were reconstructed for this analysis, additional corrections were applied to the cell energies in the calorimeter cryostats and inter cryostat region (ICR) [52]. These corrections were not included when cone jets were reconstructed and the CAFIX5.1 jet response was measured. The purpose of these corrections was to scale raw EM objects. These corrections were introduced for a special reconstruction environment called *DØFIX* [53]. We will refer to these corrections as DØFIX corrections from here on.

The DØFIX cryostat corrections are simple multiplicative factors which are applied at the calorimeter cell level. The DØFIX cryostat factors for the north (ECN), central (CC), and south (ECS) cryostats are shown in Table 8.1. A $k_\perp$ jet in a given cryostat will have a jet response that is higher (by the appropriate factor) than the CAFIX5.1 jet response. To correct $k_\perp$ jets, therefore, we multiply the CAFIX5.1 jet

response by 1.0496 (the CC DØFIX factor) and adjust jet correction in the north and south cryostats, F^N_{cry} and F^S_{cry}, to accommodate the DØFIX factors.

DØFIX Cryostat Factors		
ECN	CC	ECS
1.0609	1.0496	1.0478

Table 8.1: Cryostat corrections applied to the energy in the calorimeter cryostats introduced for the DØFIX environment.

The DØFIX corrections to the inter cryostat region (ICR) are not so straightforward. So we use jet P_T balance in two jet events to determine an ICR correction.

8.3 Cryostat Factor Correction

The jet response varies in the different η regions of the calorimeter. To eliminate these variations, we correct the $k_\perp$jet momentum, P_{kt}, so that uniform (in η) jet response correction may be applied. The CAFIX5.1 jet response we will use has been corrected for the η dependent factors (cryostat and ICR) using 0.7 cone jets. The η dependent corrections were applied to 0.7 cone jets and the event $\not\!\!E_T$ was corrected for the change in 0.7 cone jet momentum, and the jet response, $R_{jet} = 1 + MPF$, was measured. Once this is done, R_{jet} can be described by a single curve as a function of E'.

The jet response is measured for jets found in the central calorimeter cryostat, CC ($|\eta|$ <0.7), and the end cryostat, EC (1.8< $|\eta|$ <2.5). The cryostat factor, F_{cry}, (not to be confused with the DØFIX factors) is defined as the ratio $R^{EC}_{jet}/R^{CC}_{jet}$. It should not depend on the jet algorithm except where the jet pseudorapidity is needed

to determine the jet's position in the CC or EC. The value of F_{cry} using 0.7 cone jets was found to be

$$F_{cry} = 0.977 \pm 0.005\,(\text{stat}) \text{ for RECO V12}\,.$$

To verify that no complications arise from using a subset of the data or using $k_\perp$ jets to determine pseudorapidity and to correct event $\not\!\!E_T$, we remove the DØFIX cryostat corrections from $k_\perp$ jets, correct the EC jets with F_{cry}=0.977. We correct the event $\not\!\!E_T$ for the change in $k_\perp$ jet momentum. The resulting jet response is consistent with the CAFIX5.1 jet response with good agreement in the overlap region between central and forward jets (Figure 8.1).

Because the DØFIX correction factors are different in the north and south cryostats, we will have different jet response cryostat factors. The ratio of north to south cryostat factors without the DØFIX corrections was measured to be $F^N_{cry}/F^S_{cry} = 0.997 \pm 0.003$ [45]. We assume that the value F_{cry}=0.977 is the average of F^N_{cry} and F^S_{cry}. When we incorporate the DØFIX cryostat factors, we get north and south cryostat factors of F^N_{cry}=0.986 and F^S_{cry}=0.977.

8.4 $E' \rightarrow P_{kt}$ Mapping

Before mapping E' to P_{kt}, we subtract the offset from the jets. Then, we correct for the cryostat factors, F^N_{cry}=0.986 and F^S_{cry}=0.977. We map jets in the CC and EC separately and because jets in these two regions may fall partially into the ICR, we also include the η dependent ICR correction. We will discuss in detail how we

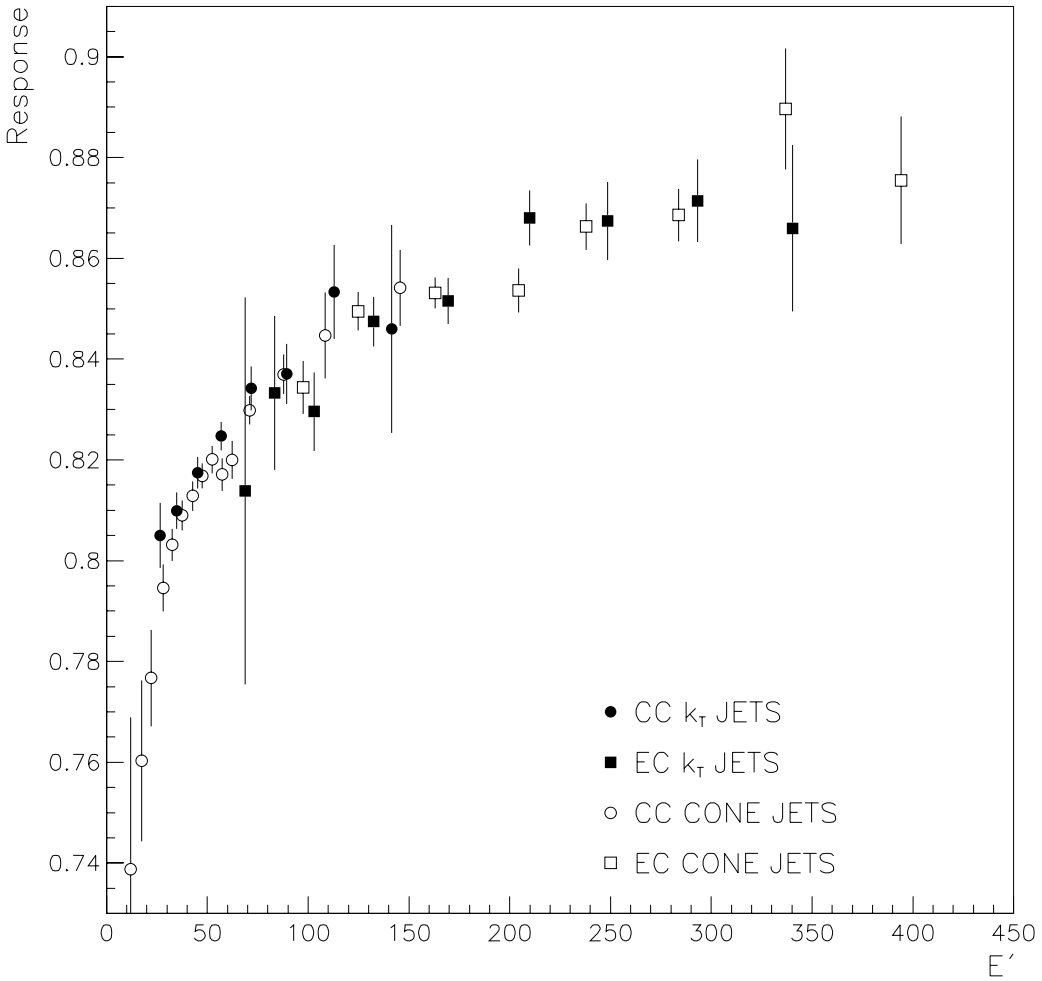

Figure 8.1: Response versus E'. Open symbols are from the full γ-jet data sample and solid symbols are from the smaller sample reconstructed with $k_\perp$ jets. The additional DØFIX cryostat corrections were removed from $k_\perp$ jets.

derived this correction for $k_\perp$ jets in section 8.6. The jet response has been corrected for the ICR using 0.7 cone jets. So this correction is only necessary for the mapping of E' to P_{kt}.

Once the jets have been corrected for the offset and the eta dependent jet response corrections, the average P_{kt} is binned in E' and plotted as a function of E' (Figure 8.2). We fit a straight line (ax + b) to the CC and EC jets separately. The fit parameters for the CC and EC are shown in Table 8.2. The results of the fits are shown in Figure 8.2 with χ^2/d.o.f. = 2.29 in the CC and χ^2/d.o.f. = 1.11 in the EC.

$E' \rightarrow P_{kt}$ Mapping Parameters		
	CC	EC
a	0.835 ± 0.009	0.838 ± 0.014
b	2.465 ± 0.392	4.522 ± 2.008

Table 8.2: Fit parameters for E' to P_{kt} mapping.

8.5 Response vs. P_{kt}

To accommodate the DØFIX corrections to the cryostats, the CAFIX5.1 jet response is scaled by the DØFIX CC factor. Using this and the mapping parameters above, we translate the R_{jet} versus E' data to R_{jet} versus P_{kt}. We fit R_{jet} versus P_{kt}using the same functional form that was used in CAFIX5.1,

$$R_{jet}(P_{kt}) = a + b \cdot \ln(P_{kt}) + c \cdot \ln\left(P_{kt}\right)^2 \tag{8.9}$$

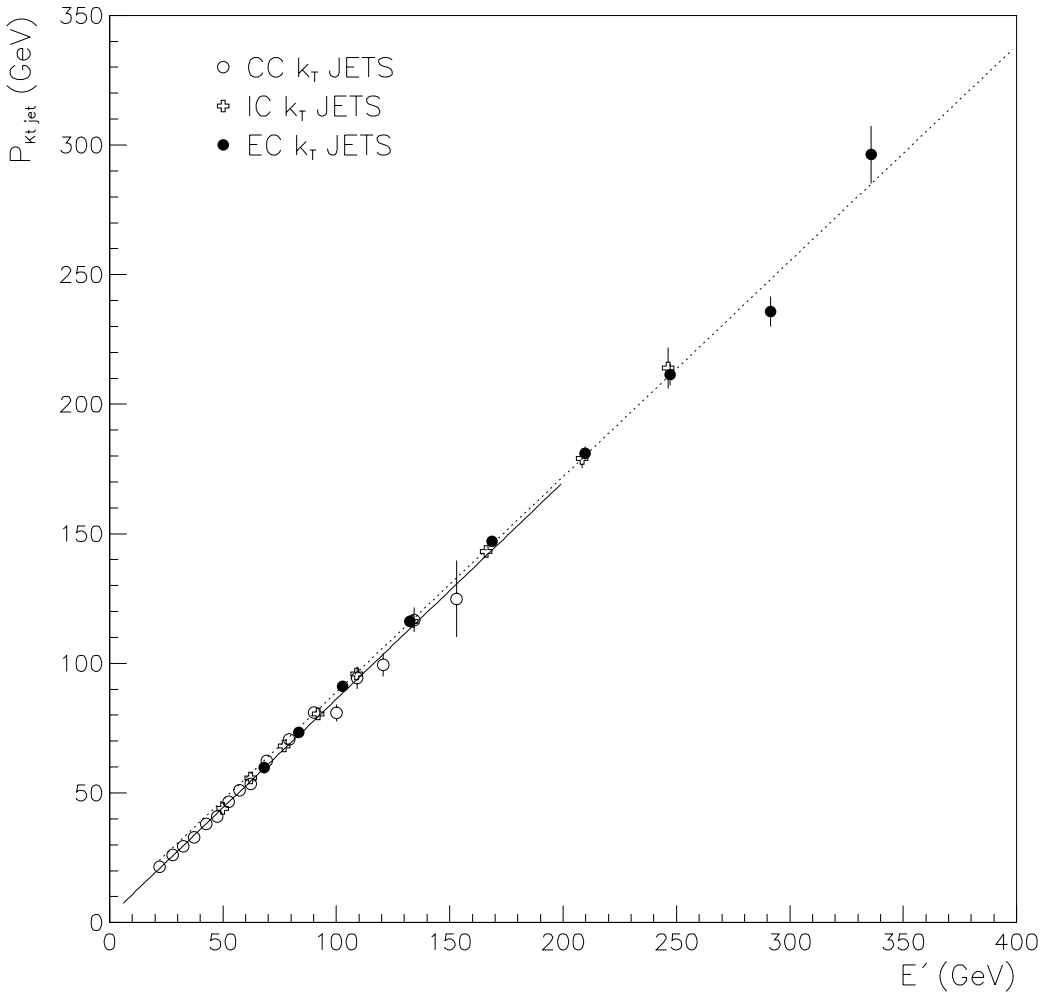

Figure 8.2: $k_\perp$ jet P versus E'. Straight lines were fit to the CC and EC separately.

We use a Monte Carlo point to constrain the fit at high momenta. We use the same Monte Carlo point that was used in CAFIX5.1 except we multiply both the jet momentum and the jet response by the DØFIX CC cryostat factor. The result of the fit is shown in Figure 8.3.

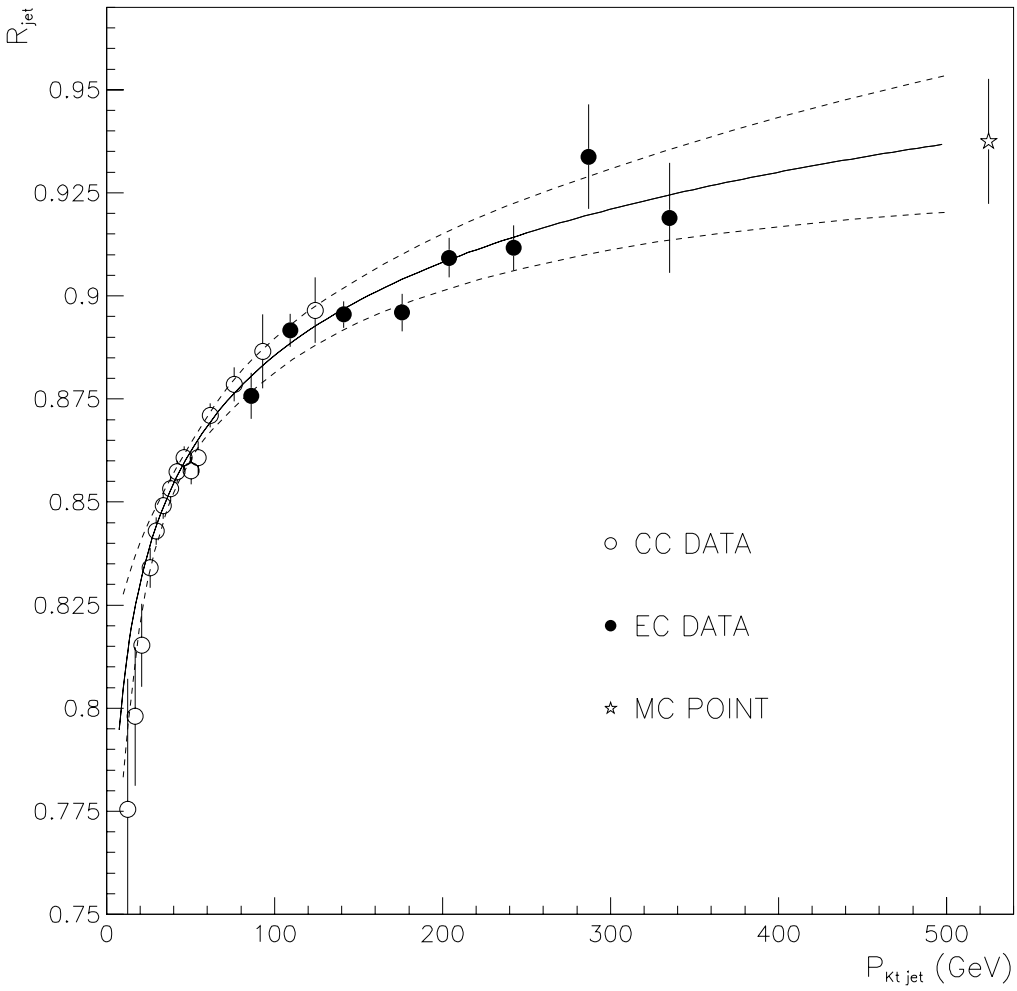

Figure 8.3: R_{jet} versus P_{kt}. The outer band shows limits on the measured jet response for high momentum jets based on the region in parameter space defined by the $\chi^2 = \chi^2_{min} + 3.5$ surface. This region corresponds to the 68% confidence region of parameter fluctuations from the nominal values.

The data were fit for $P_{kt} > 30$ GeV. The fit parameters are shown in Table 8.3. For comparison, the fit is shown in Figure 8.4. We also show the $k_\perp$ R_{jet} fit divided

Jet Response Parameters $R_{jet}(P_{kt}) = a + b \cdot \ln(P_{kt}) + c \cdot \ln(P_{kt})^2$			
	a	b	c
	0.7174 ± 0.0518	0.0399 ± 0.0233	-.0007 ± 0.0026

Table 8.3: Fit parameters for $k_\perp$ jet hadronic response correction.

by the DØFIX CC factor (with P_{kt} also divided by the DØFIX CC factor) for shape comparison with the fits for the cone algorithm. The single parameter errors show one standard deviation uncertainties as calculated from the $\chi^2 = \chi^2_{min} + 1$ surface in the parameter space. χ^2/d.o.f. = 0.650 for the fit.

8.6 ICR Correction

The cryostat factor, F_{cry}, is intended to put the end calorimeter cryostats on the same footing as the central cryostat. We wish to do the same in the ICR. To do this we use transverse momentum balance in di-jet events. The method is similar to that used to measure the hadronic response, but here, the central jet plays the role of the photon.

8.7 Jet-Jet Data

The jet-jet data used to determine the η dependent correction in the ICR to the jet response is taken from events passing the inclusive jet triggers (triggers requiring one or more jets in an event). These triggers are described in Appendix A.

Here is a list of the criteria for $k_\perp$ jets in our jet data.

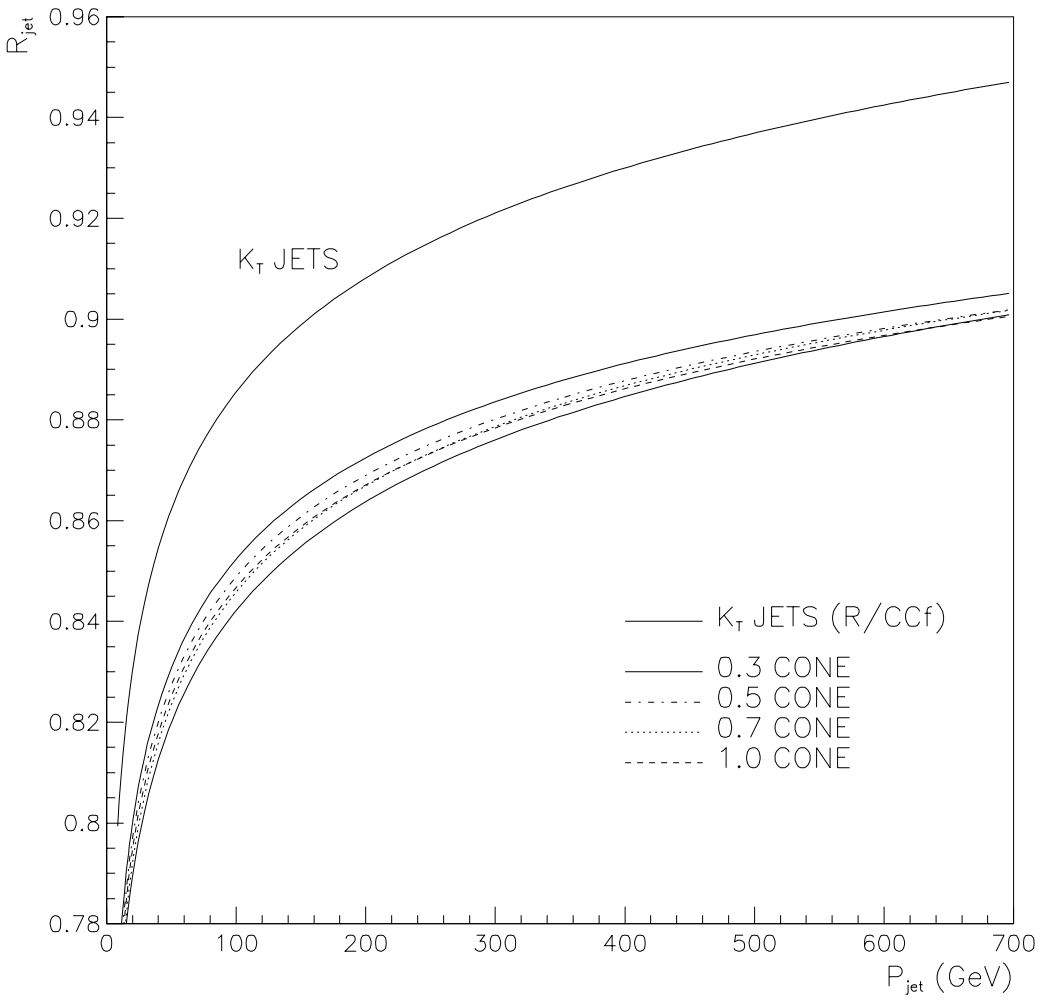

Figure 8.4: Response fit versus jet P_{kt}. $R_{jet}(P_{kt}) = a + b \cdot \ln(P_{kt}) + c \cdot \ln(P)^2$.

Data Sample	P_{T2} cut (GeV)
JET_MIN	30.0
JET_30	55.0
JET_50	90.0
JET_85	120.0
JET_MAX	175.0

Table 8.4: Second highest jet P_T requirements for triggers.

- We select events with low instantaneous luminosity, $\mathcal{L} < 5{\times}10^{30}\text{cm}^{-2}\text{sec}^{-1}$.

- We select events flagged by the MITOOL as having only one interaction.

- Events passing a given jet trigger must be fully efficient for the second highest P_T jet [49]. This removes resolution biases in the forward region. A list of jet triggers and the P_T cuts are shown in Table 8.4.

- There can be one and only one vertex found, with $|z| < 50$ cm.

- We demand two and only two reconstructed jets (no third jet with $P_T > 15$ GeV.

- We demand at least one jet with $|\eta_{jet}| < 0.5$.

- The missing transverse energy in the event, $\not\!\!E_T$, must be less than 70% of the leading jet P_T, $\frac{\not\!\!E_T}{E_{T1}} < 0.7$. $\not\!\!E_T$ is the magnitude of the vector momentum necessary to balance the entire event in the transverse plane. It is defined by

$$\not\!\!E_T = -\sqrt{\left(\sum_{i=1}^{n} P_{xi}\right)^2 + \left(\sum_{i=1}^{n} P_{yi}\right)^2}\ . \tag{8.10}$$

8.7.1 Measurement of F_η

We correct the $k_\perp$ jets for the cryostat factor and correct the event $\not\!\!E_T$ using the change in $k_\perp$jet momentum. The relative jet response of the forward jet with respect to the central jet, R^{rel}_{meas}, is measured as in photon events substituting the central jet for the photon:

$$R^{rel}_{meas}(E,\eta) = 1 + \frac{\vec{\not\!\!E}_T \cdot \hat{\eta}_{central\ jet}}{{P_T}^{central\ jet}}. \tag{8.11}$$

In a uniform detector and at leading order, the momentum of the forward jet would be given by $P^\eta = P_T^{CC} cosh\eta$. The ideal relative jet response, R^{rel}_{calc}, for the two jets could be calculated using the jet response as a function of P_{kt} by

$$R^{rel}_{calc}(P,\eta) = \frac{R_{jet}(P_T^{CC} cosh\eta)}{R_{jet}(P^{CC})}. \tag{8.12}$$

Thus, the η dependent ICR correction, f_η, is simply the factor needed to correct R_{meas} to R_{calc}.

Using the fit to $R_{jet}(P_{kt})$, we compare R_{meas} to R_{calc} in Figures 8.5 and 8.6.

To parameterize the correction factor, f_η, we look at η bins of 0.1 in the regions -2.0< η <-0.5 and 0.5< η <2.0. For each bin, we plot the correction factor as a function of the average P_T of the forward jet in a given bin for a given trigger. We fit these with a straight line and these fits are used to determine f_η as a function of jet P_T for each η (see Figures 8.7 and 8.8). After the correction is applied, R_{meas} agrees well with R_{calc} (see Figure 8.9).

As previously mentioned, the CAFIX5.1 jet response has been corrected for the η

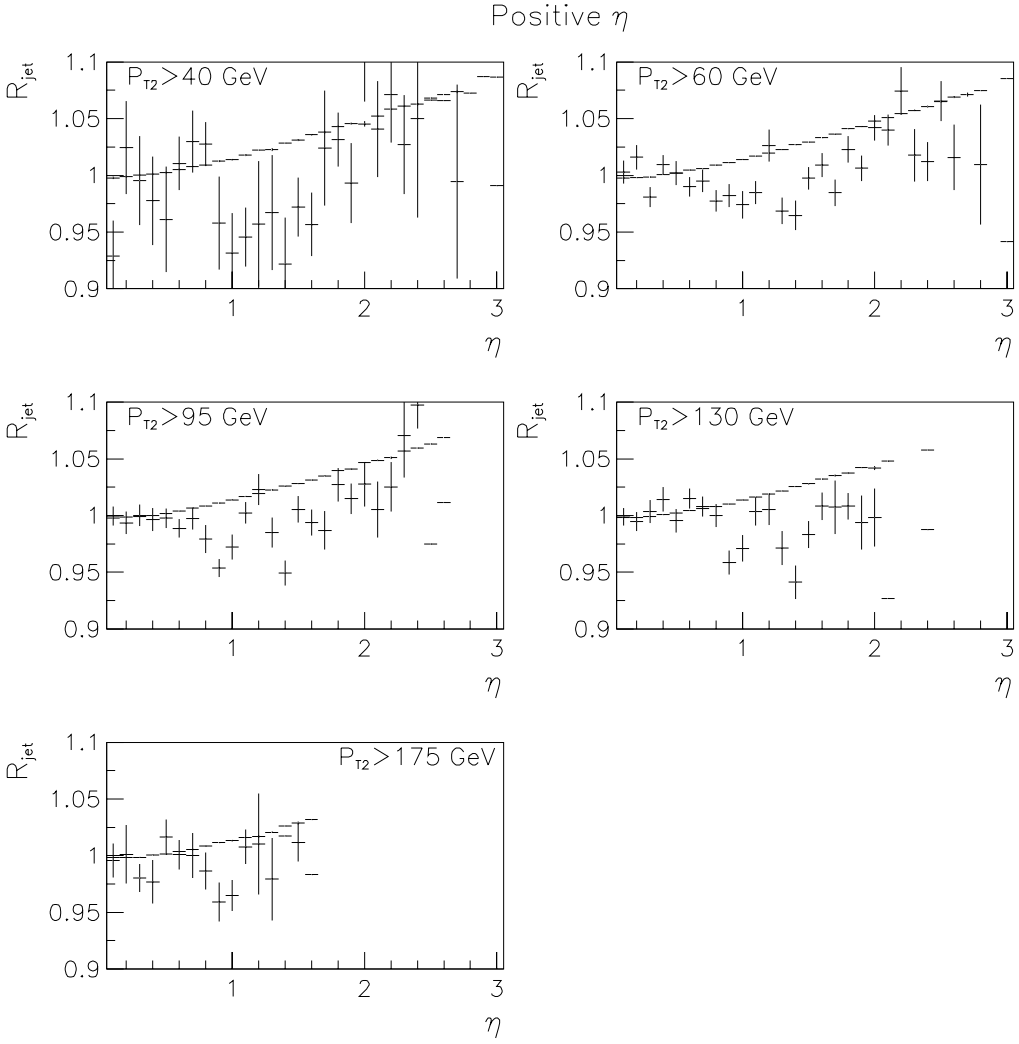

Figure 8.5: Response versus η >0.0 for jet-jet data.

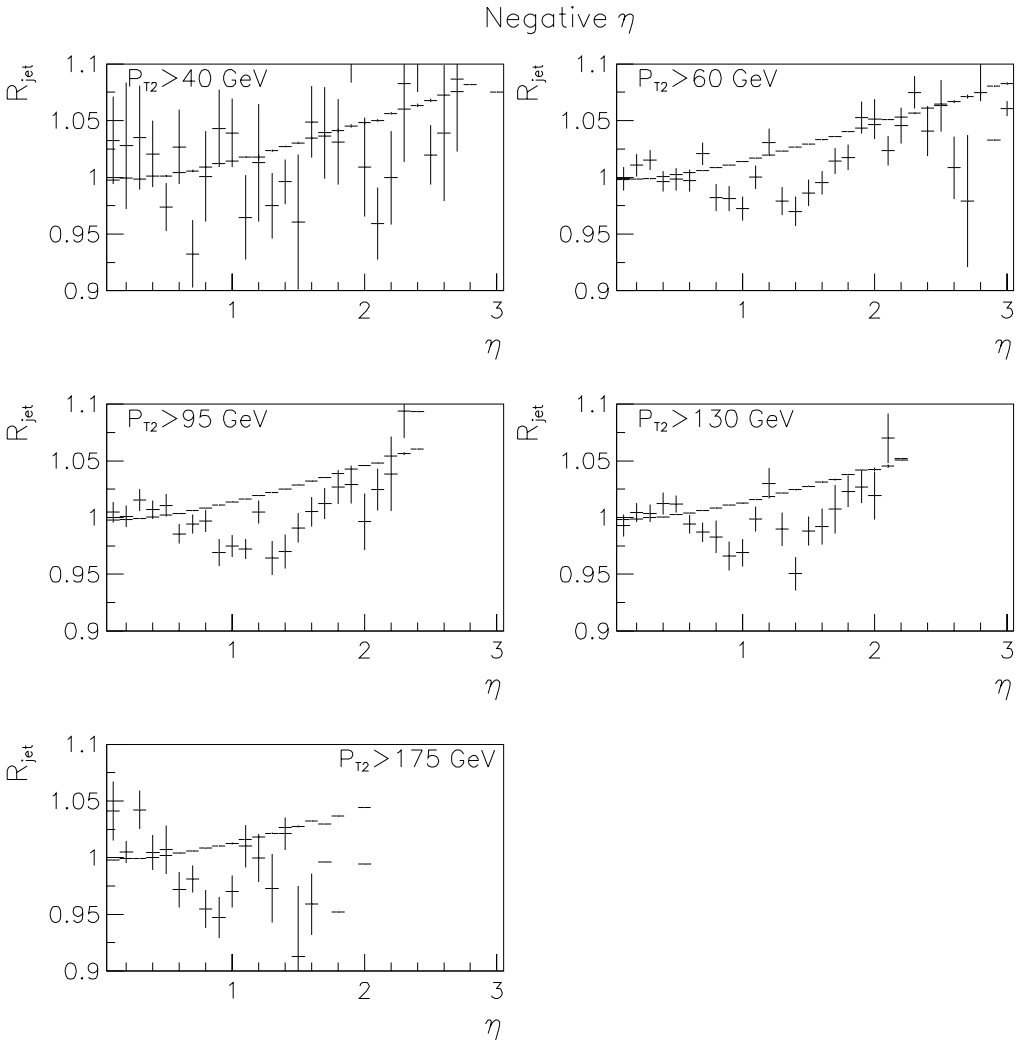

Figure 8.6: Response versus η <0.0 for jet-jet data.

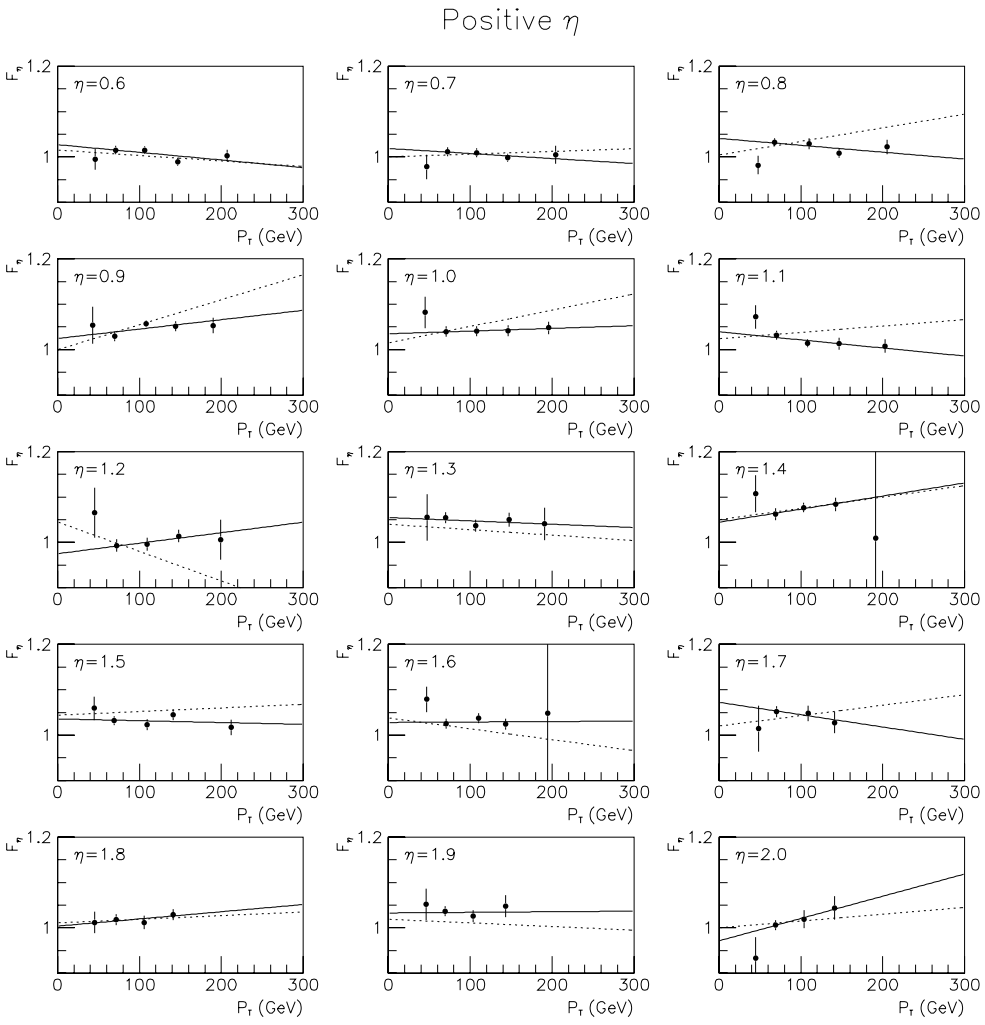

Figure 8.7: Correction factor F_η as a function of central jet P_T for positive η. The solid straight line is a fit to the data. The dotted line is the CAFIX5.1 correction for 0.7 cone jets.

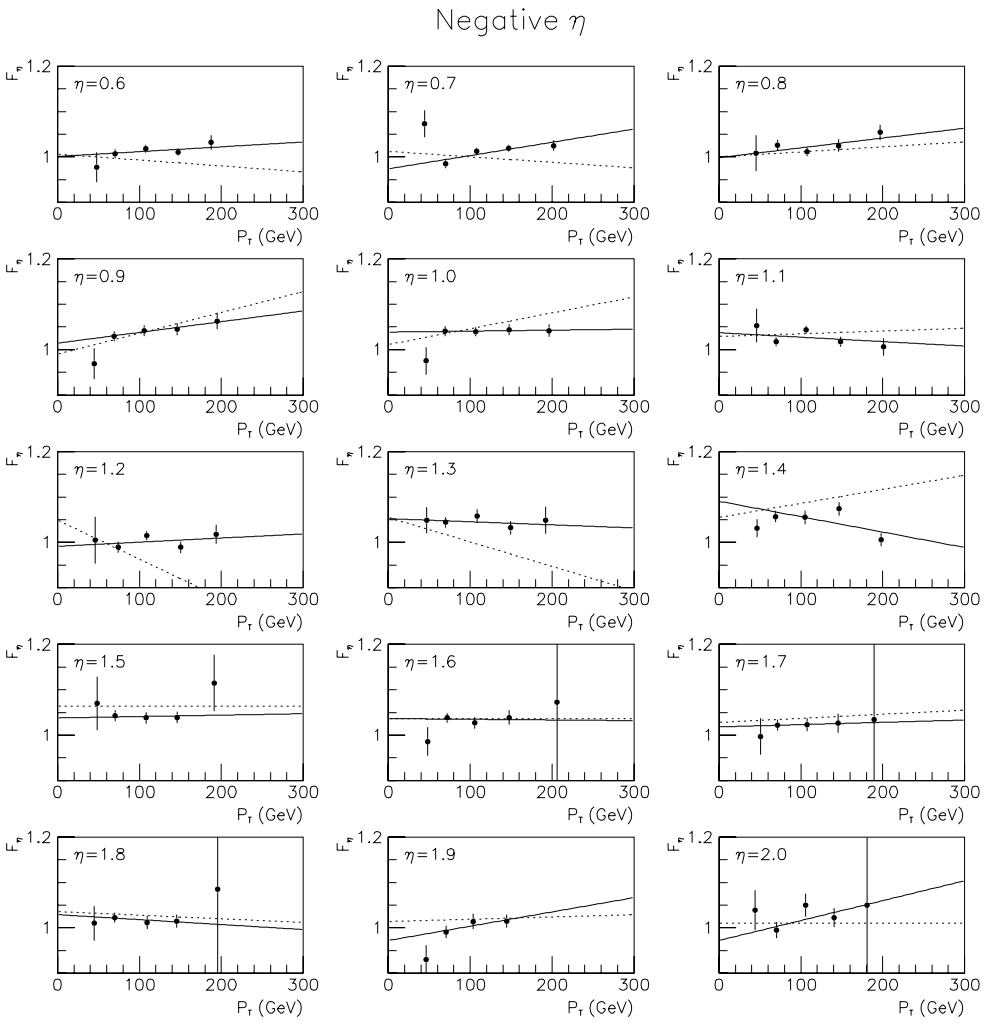

Figure 8.8: Correction factor F_η as a function of central jet P_T for negative η. The solid straight line is a fit to the data. The dotted line is the CAFIX5.1 correction for 0.7 cone jets.

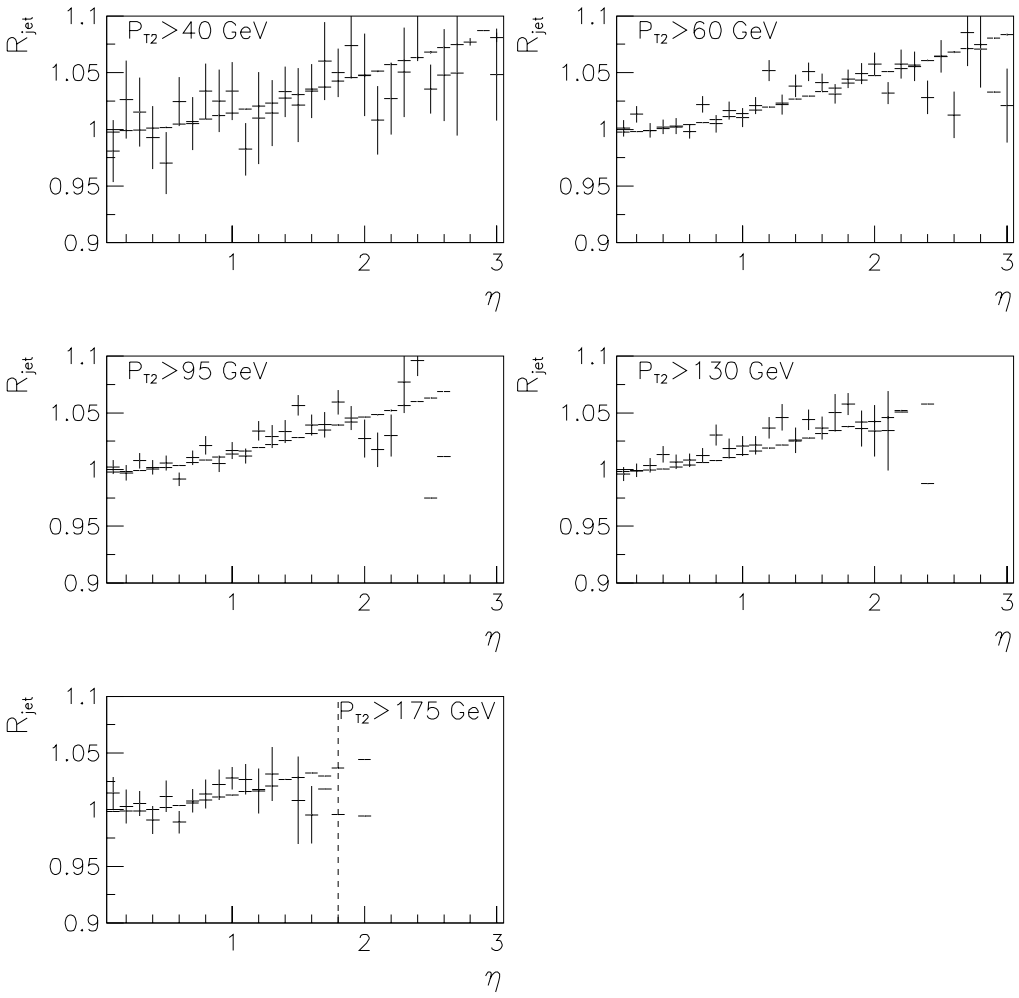

Figure 8.9: Response versus η after η dependent corrections.

dependent factors (cryostat and ICR) using 0.7 cone jets. Therefore, the corrections derived here will have no bearing on R_{jet} versus E'. They can, in principle, effect the R_{jet} versus P_{kt} fit via their effect on the mapping of E' to P_{kt}($k_\perp$ jets are corrected for the offset, cryostat factor, and ICR dependencies prior to mapping). This effect on the fit is negligible as seen in Figure 8.10

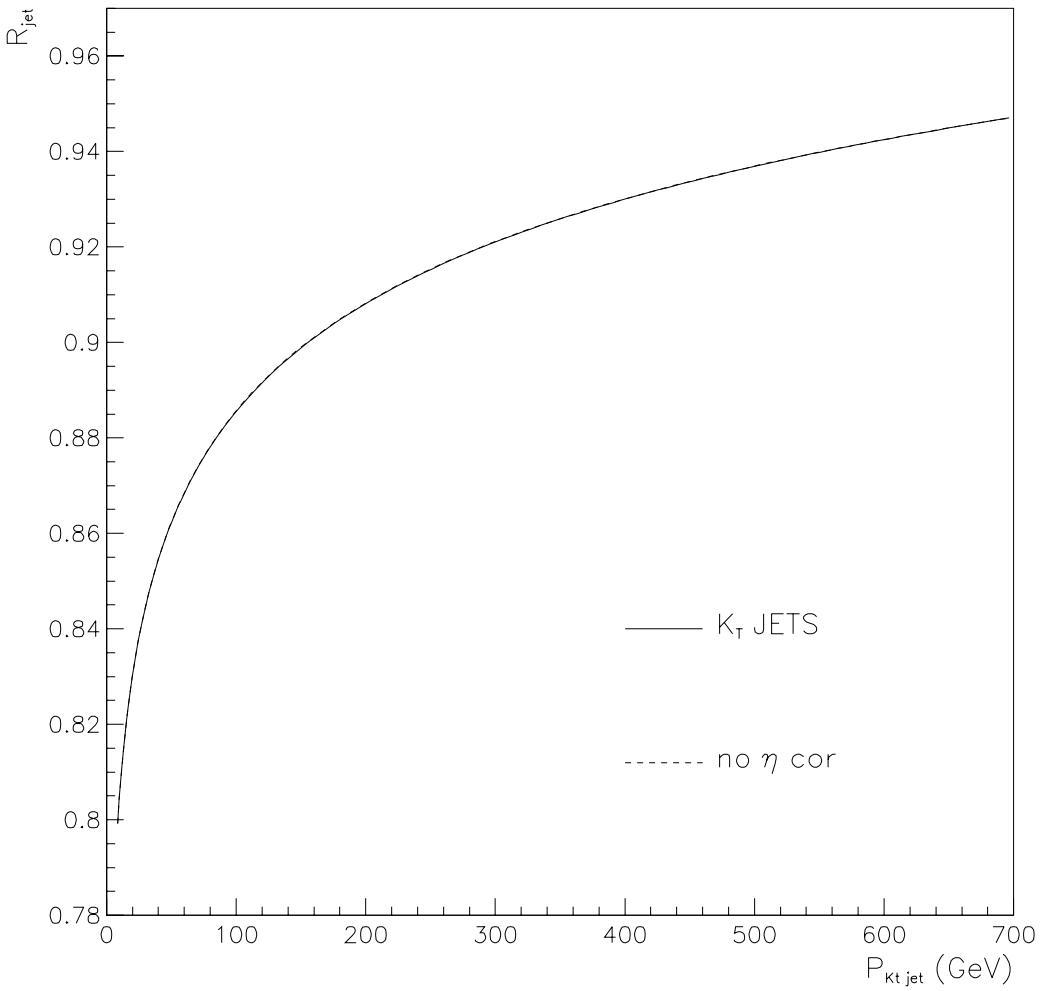

Figure 8.10: Response fit versus jet E with and without the ICR correction. $R_{jet}(E) = a + b \cdot \ln(E) + c \cdot \ln(E)^2$. The two curves are virtually identical.

8.8 The Low E_T Bias

The minimum E_T reconstruction threshold for 0.7 cone jets is 8 GeV. The jet reconstruction efficiency for this threshold does not reach 100% until 20 GeV. This, combined with a steeply falling jet E_T distribution, leads to biases in the jet response measured using the MPF method.

To remove this bias, the jet response was measured as a function of $E_{T\gamma}$ (instead of E') with no jet requirements. The bias is estimated using

$$R_{bias} = \frac{R_{Jet(\geq\ 1\ jet)}}{R_{Jet(no\ jet\ required)}}\ , \tag{8.13}$$

where the numerator is measured as described in Section 8.1 with the jet required to be in the CC. Since the denominator has no jet requirement, the hadronic recoil is unrestricted and may lie in the EC or ICR making the numerator and denominator inconsistent. To reconcile this, R_{bias} is normalized to unity for $E_{T\gamma} > 20$ GeV(where the reconstruction efficiency for jets is 100%).

The jet response, R_{jet}, is corrected in the following way. First, the 0.7 cone jets (in the CC) are corrected by the inverse of R_{bias}. Then, the event missing E_T is corrected for the change in the 0.7 cone jet momentum, and R_{jet} is measured with the corrected $\not\!\!\vec{E}_T$.

The three lowest points in Figure 8.3 have been corrected for this bias. The large error bars reflect the uncertainty determined from a Monte Carlo simulation where the resolutions, efficiency and reconstruction parameters were varied.

8.9 Low P_{kt} Jet Response

In this study, we included $k_\perp$ jets with $P_{Tjet} > 2$ GeV. We hoped to avoid the Low E_T bias described above because this threshold is considerably lower than the 8 GeV threshold used for finding cone jets. Unfortunately, it is difficult to extract a hard 2-to-2 process involving a photon and a jet at low momentum. When the jet response is low, a jet's position resolution is also poor. A jet and a photon resulting from a 2-to-2 process will less likely be found back to back if the jet response is low than if it is high. This is the case for low energy events as demonstrated in Figure 8.11 where $\Delta\phi_{\gamma\ jet}$ ($\Delta\phi_{\gamma\ jet} = |\phi_\gamma| - |\phi_{jet}|$) is shown for low and high momentum $k_\perp$ jets.

In addition to this, we see that for $E_{T\gamma} < 20$ GeV, the 1st, 2nd and 3rd jets appear to have similar P_T distributions making it difficult to differentiate between jets coming from the hard process and spurious jets reconstructed from underlying event and noise. Figure 8.12 shows the P_T distributions of $k_\perp$ jets (excluding $k_\perp$ jets reconstructed from the photon) for a range of $E_{T\gamma}$.

Some attempt was made to pronounce the structure of these events. We tried loosening the back-to-back cut and allowing (in addition to the leading jet) the 2nd or 3rd jet to balance the photon. While this was effective in unbiasing the jet response, it wasn't very useful in achieving the ultimate goal of jet momentum calibration because it also allows events where more than one object balances the photon. In addition, questions are raised as to how to treat jets in such events where it is difficult to discern between a hard interaction and underlying event and noise.

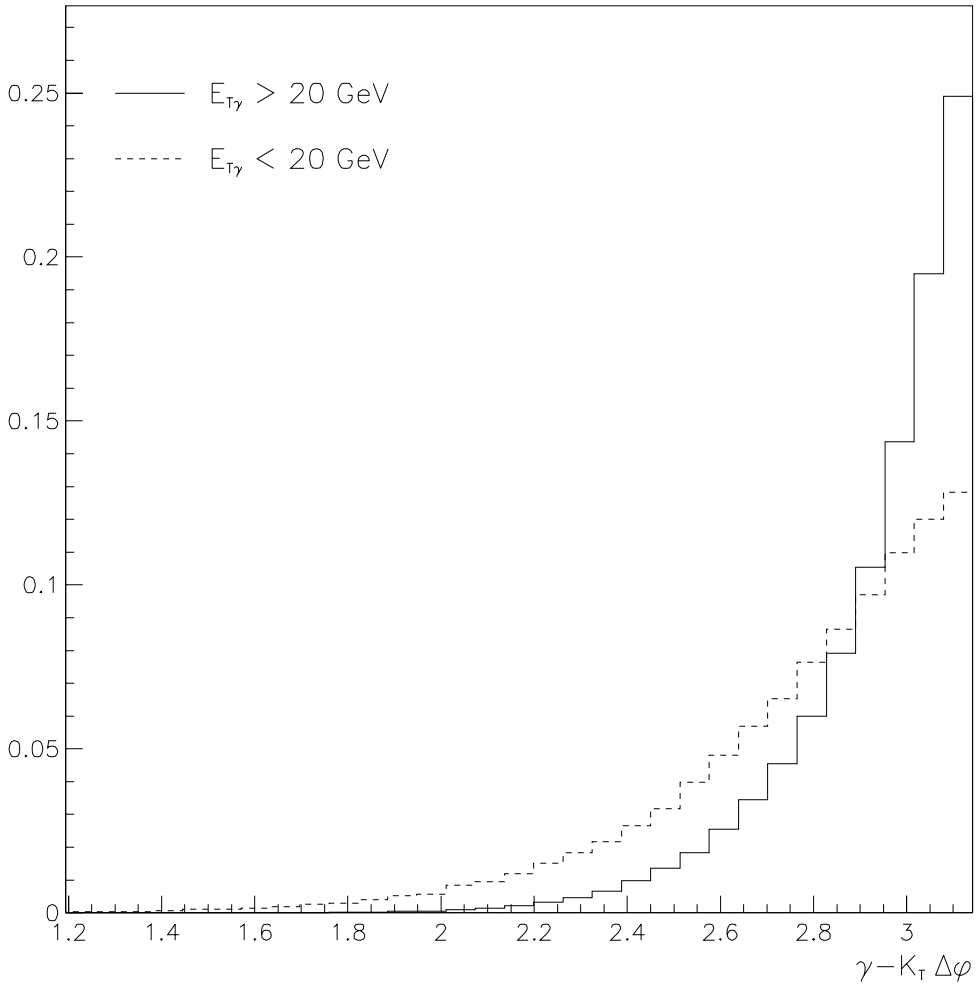

Figure 8.11: $\Delta\phi_{\gamma\ jet}$ normalized distribution for $k_\perp$ jets ($\Delta\phi_{\gamma\ jet} = |\phi_\gamma| - |\phi_{jet}|$).

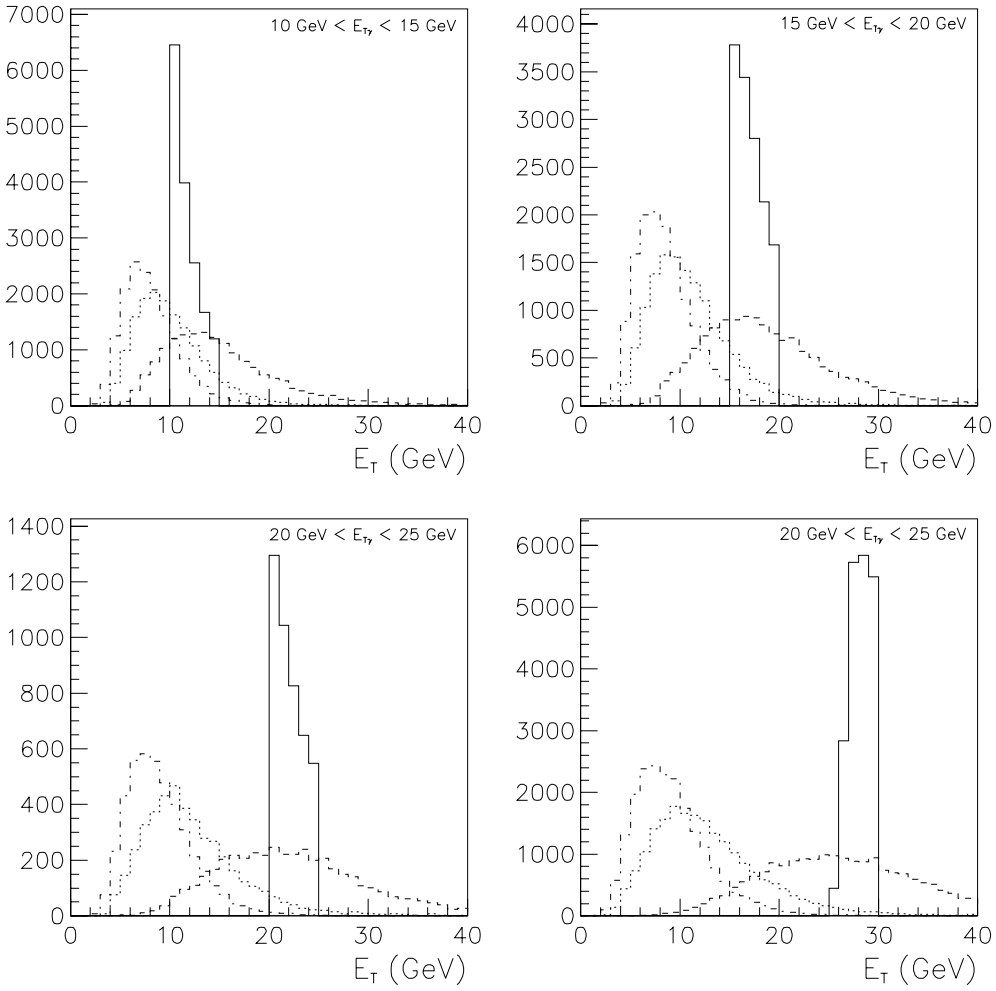

Figure 8.12: E_T distribution of $k_\perp$ jets. Solid lines show $E_{T\gamma}$ distributions and dotted and dashed lines show E_T distributions of the 1st, 2nd and 3rd jets.

So, although we do not have a bias due to the reconstruction threshold, it appears that we do introduce a topology bias at low energy by requiring the leading jet and photon to be back to back. This causes us to reject events where the jet's position and/or momentum is mismeasured due to low jet response and we bias ourselves toward higher jet response.

We do not apply a correction to the low P_T $k_\perp$ jets as is done for cone jets. Unlike the low E_T bias for cone jets, the topology bias is apparent only when we try to measure the response using the MPF method. Because the CAFIX5.1 jet response at low energy was derived using data with no jet requirement (Equation 8.13), it is considered to be free of this topology bias. We use the unbiased jet response derived for CAFIX5.1 and assign an additional error due to the effect of unbiasing. The error bars on the three lowest energy points in Figures 8.3 and 8.13 reflect this error.

The jet response is fit for P_{kt} above 30.0 GeV and, therefore, the low momenta data do not affect the result of the fit. The low momenta data diverge from the extrapolated fit (see Figure 8.13a). To correct for this, we fit the function, $f(x) = 1 + a(x-35)^2$, to the ratio of the extrapolated fit to the low energy data, R_{e-f}/R_{low}. Dividing the extrapolated fit by this function, $R_{e-f}/f(x)$ provides a jet response curve for the low energy data which matches both slope and function at 35 GeV with R_{e-f} (see Figure 8.13b). We match the fits at 35 GeV instead of 30 in order to get a smooth match.

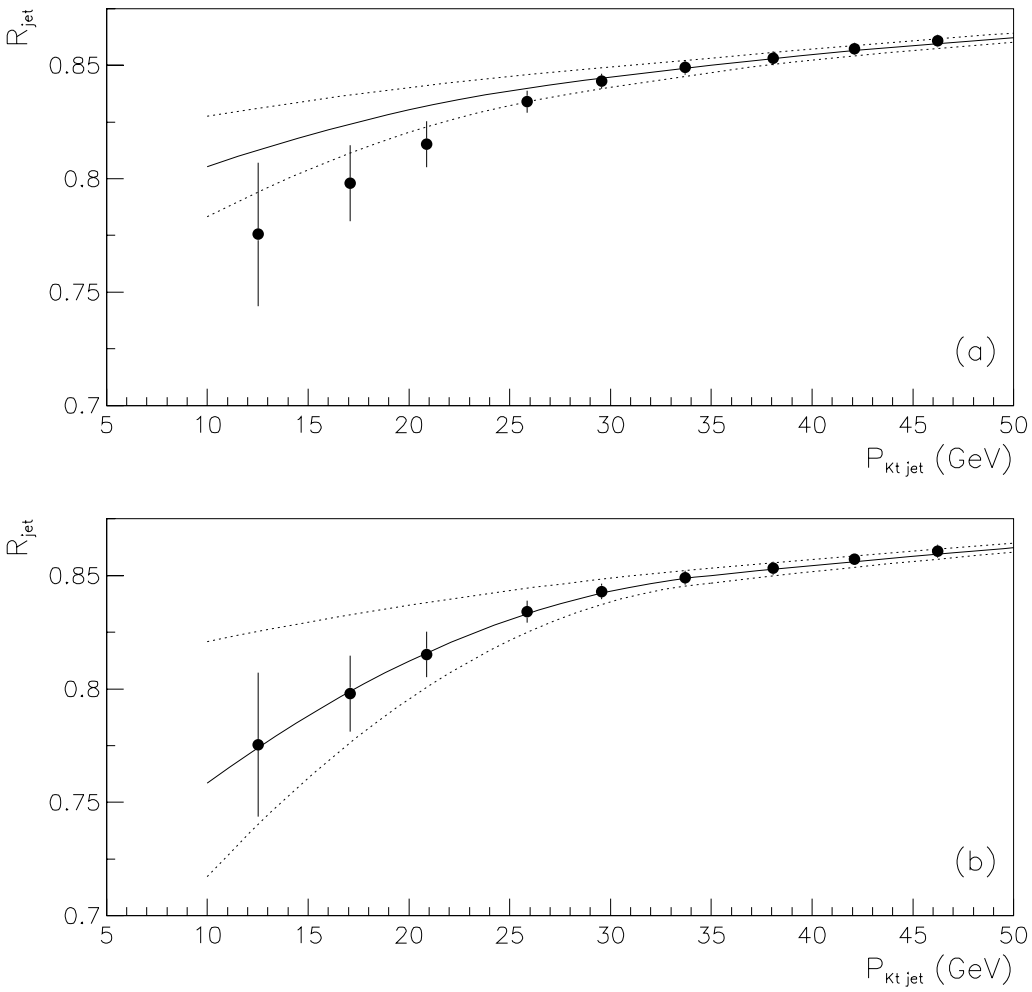

Figure 8.13: Low momentum jet response vs. P_{kt}. (a) The solid line is the extrapolated fit. Dotted lines depict errors on the fit. (b) The solid line is the jet response used to correct jets. The dashed lines show the errors (as a function of P_T).

8.10 The Jet Response Errors

8.10.1 Errors and Correlations of the R_{jet} Fit

To determine an error for the response function, a surface defined by $\chi^2 = \chi^2_{min} + 3.5$ is mapped out in parameter space. For three parameters, this contains a region with a 68% probability for parameter fluctuations [54]. The points lying on this surface are then mapped back onto the jet response versus momentum plane. At a given momentum, the error is determined by the parameter set giving the greatest deviation from nominal jet response. The high and low errors are calculated for 11 points, (10, 20, 35, 50, 75, 100, 150, 200, 300, 400, and 500 GeV). The error is interpolated for energies between these 11 points. The result for the $k_\perp$ jet algorithm is shown in Figure 8.3. The outer band represents the error on the fit to the jet response.

The fit error described above gives the maximum deviation at each P_{kt} value for all the fit parameters within the 68% confidence level. The parameter set that gives this deviation at one value of P_{kt} does not necessarily induce the same effect at another value and it is highly unlikely that one set of parameters will produce either of the error curves shown in Figure 8.3. We do expect, however, that the errors for two points close in P_{kt} will be largely correlated.

To quantify the correlations between different values of P_{kt}, we generate a correlation matrix in the following way.

- We map out a grid in parameter space defining the $\chi^2 \leq \chi^2_{min} + 3.5$ volume.

Each parameter set in this volume defines a response function contained within the bands shown in Figures 8.3.

- The correlations are calculated for an 11 $\times$ 11 matrix. We loop through all the parameter sets in the volume and calculate response at eleven values of P_{kt} (corrected for offset and η dependence) between 10 and 500 GeV. The matrix elements are the standard correlation coefficients, $r(i,j)$, between the responses measured at each energy value. $r(i,j)$ is defined as:

$$r(i,j) = \frac{\sum_{n=1}^{N_{grid}}(R_n(i) - \overline{R(i)})(R_n(j) - \overline{R(j)})}{[\sum_{n=1}^{N_{grid}}(R_n(i) - \overline{R(i)})^2 \sum_{n=1}^{N_{grid}}(R_n(j) - \overline{R(j)})^2]^{\frac{1}{2}}}, \tag{8.14}$$

where N_{grid} is the number of parameter sets in mapped out in the $\chi^2 \leq \chi^2_{min} + 3.5$ volume and $R_n(i)$ is the response for the i^{th} energy bin calculated with the n^{th} parameter set.

The correlation matrix for the jet response fit to $k_\perp$ jets is shown in Table 8.5. Correlations are illustrated graphically in Figure 8.14 where four rows of the matrix are plotted showing the error correlations relative to the errors at 35, 50, 100, and 500 GeV respectively.

8.10.2 Low Momentum Errors

For the error due to the unbiasing of the jet response (the error bars), σ_b, we used the function, $f(x) = a(x-35)^2$, where a is defined such that the error decreases from 3% to 0 from 15 GeV to 35 GeV. This comfortably accomodates the error bars. This is added in quadrature with the errors on the extrapolated fit, σ_{e-f} for the low

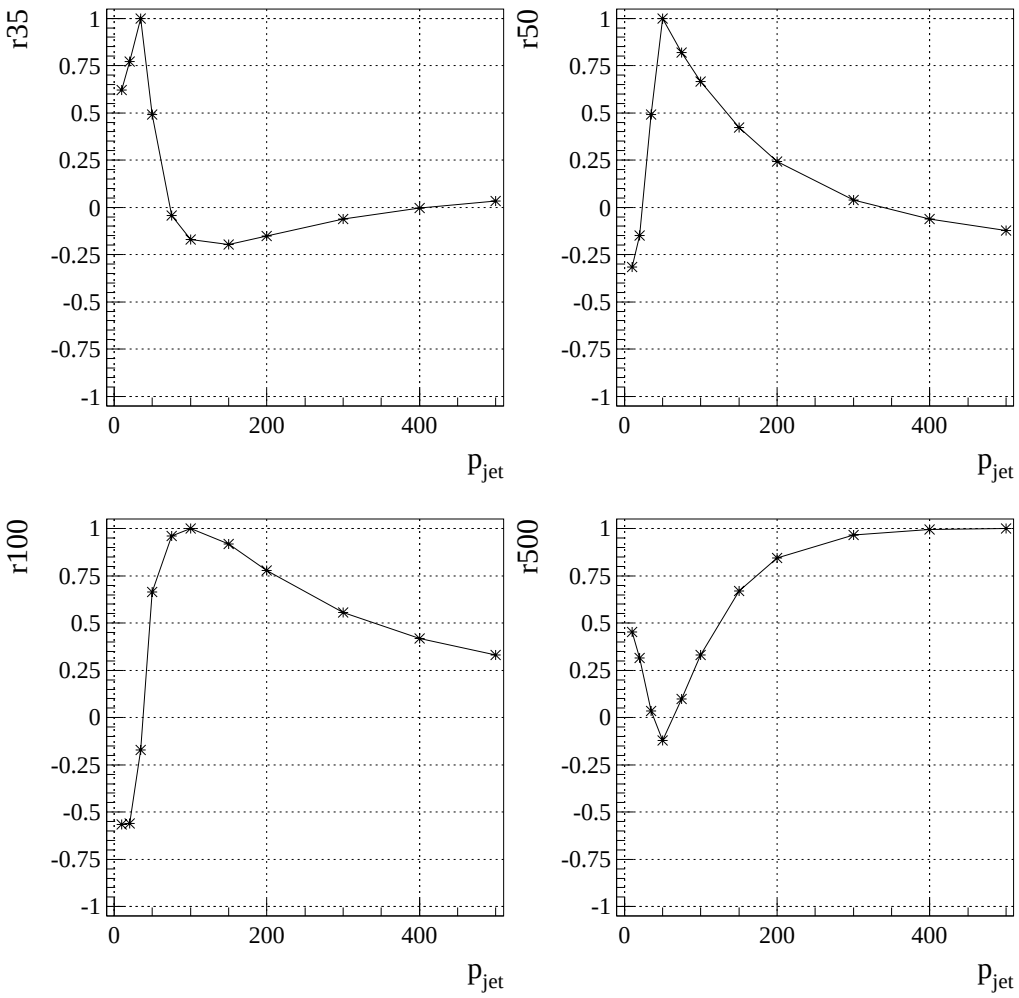

Figure 8.14: Error correlations for $k_\perp$ jet response fit. Error correlations are shown in four slices from the full correlation matrix. The four curves show the point-to-point correlation of fit errors relative to momentum values of 35, 50, 100, and 500 GeV respectively.

Correlations for Fit Error, $k_\perp$ Jets, Reco 12											
P(GeV)	10	20	35	50	75	100	150	200	300	400	500
10	1.00	0.97	0.62	-0.32	-0.63	-0.56	-0.29	-0.06	0.23	0.37	0.45
20	0.97	1.00	0.77	-0.15	-0.57	-0.56	-0.36	-0.16	0.10	0.23	0.31
35	0.62	0.77	1.00	0.49	-0.04	-0.17	-0.20	-0.15	-0.06	0.00	0.03
50	-0.32	-0.15	0.49	1.00	0.82	0.67	0.42	0.24	0.04	-0.06	-0.12
75	-0.63	-0.57	-0.04	0.82	1.00	0.96	0.78	0.59	0.33	0.19	0.10
100	-0.56	-0.56	-0.17	0.67	0.96	1.00	0.92	0.78	0.56	0.42	0.33
150	-0.29	-0.36	-0.20	0.42	0.78	0.92	1.00	0.96	0.84	0.74	0.67
200	-0.06	-0.16	-0.15	0.24	0.59	0.78	0.96	1.00	0.95	0.89	0.84
300	0.23	0.10	-0.06	0.04	0.33	0.56	0.84	0.95	1.00	0.99	0.97
400	0.37	0.23	0.00	-0.06	0.19	0.42	0.74	0.89	0.99	1.00	1.00
500	0.45	0.31	0.03	-0.12	0.10	0.33	0.67	0.84	0.97	1.00	1.00

Table 8.5: Correlation matrix for error band in hadronic jet response correction for $k_\perp$ jets.

error (high in jet P). The high error (high jet P) is the low error added in quadrature with the difference between the extrapolated fit and the actual fit.

$$\begin{aligned} \sigma_{low} &= \sqrt{\sigma_b^2 + \sigma_{e-f}^2} \\ and \quad \sigma_{high} &= \sqrt{\sigma_b^2 + \sigma_{e-f}^2 + \sigma_{diff}^2} \end{aligned} \tag{8.15}$$

The correction to the extrapolated fit is applied as a function of momentum. However, the uncertainty is applied as a function of P_T rather than P to account for forward jets whose momentum may be above 35 GeV but whose P_T may be below 35 GeV.

8.10.3 η Dependent Correction Errors

We apply a 0.6% error on F_{cry}^N and F_{cry}^S. This is due to the 0.5% error on F_{cry} added in quadrature to the 0.3% error on F_{cry}^N/F_{cry}^S. No additional error need be considered given that the DØFIX cryostat factors are known and definite.

η Region	Mean	RMS	N	RMS/$\sqrt{N}$
$\|\eta\|$ <0.5	0.0028	0.0113	25	0.0023
0.5< $\|\eta\|$ <1.0	0.0061	0.0101	25	0.0020
1.0< $\|\eta\|$ <1.5	0.0083	0.0213	25	0.0043
1.5< $\|\eta\|$ <2.0	-.0005	0.0186	24	0.0038
2.0< $\|\eta\|$ <2.5	-.0146	0.0320	18	0.0076
2.5< $\|\eta\|$ <3.0	-.0107	0.0500	11	0.0151

Table 8.6: Residuals from Figures 8.15 nd 8.16.

To measure the accuracy of the ICR correction, we apply the cryostat corrections and the ICR correction and compare R_{meas} to R_{calc}. Figure 8.15 shows the fractional difference. The distribution of these fractional differences is plotted in the 6 η regions shown in Figure 8.16. The mean, rms, number of entries, N, and rms/$\sqrt{N}$ are shown in Table 8.6. The correction is applied in the region for 0.5< $|\eta|$ <2.0. We assign a 1% error to the correction based on these values and introduce an additional η dependent error that turns on at $|\eta|$ =2.5 and increases linearly up to 3% at $|\eta|$ =3.

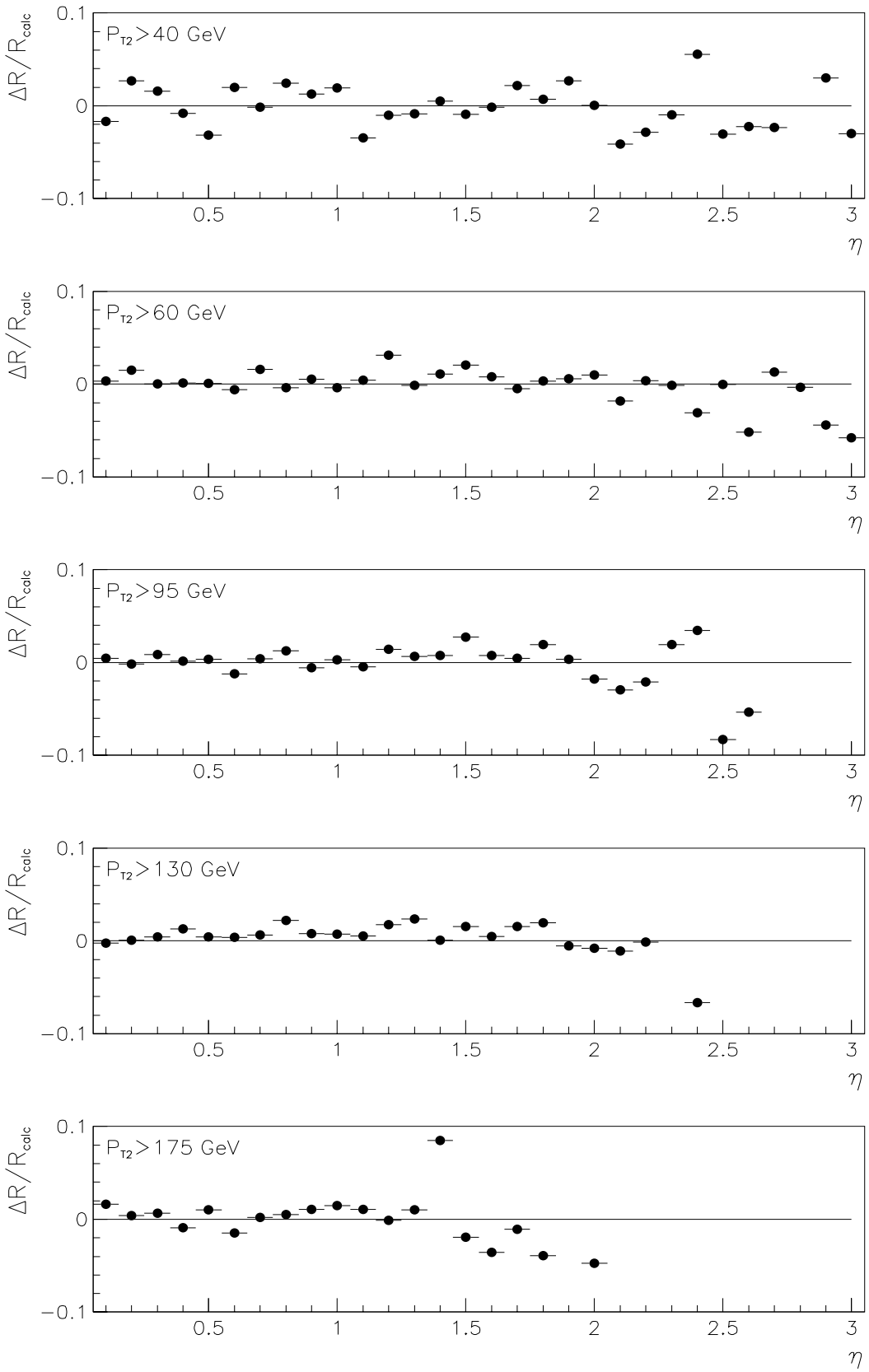

Figure 8.15: The fractional difference between R_{meas} and R_{calc} for partially corrected jets. $\Delta R = (R_{meas} - R_{calc}) \ / \ R_{calc}$.

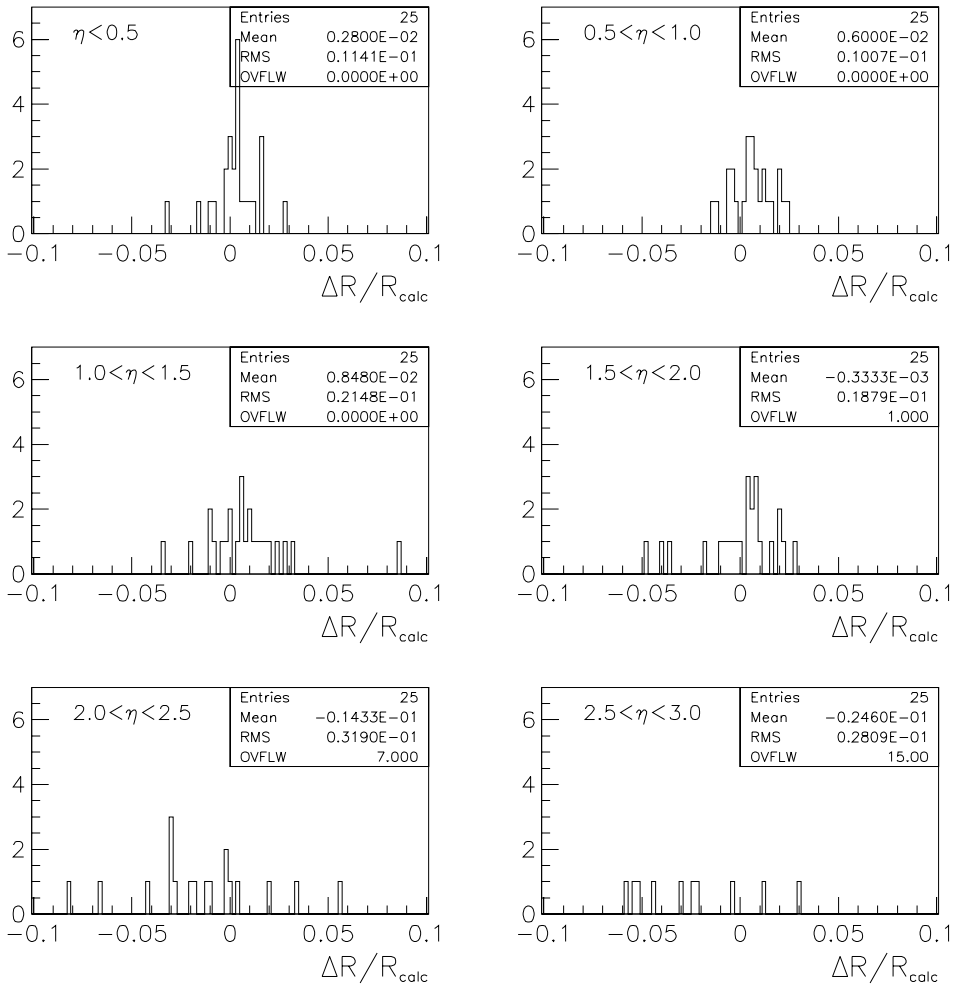

Figure 8.16: The distributions of fractional differences between R_{meas} and R_{calc}.

Chapter 9

$K_\perp$ Jet MPF Closure

The missing transverse energy projection fraction (MPF) method is tested using the Monte Carlo γ-jet events which are processed through a simulation of the DØ detector. $k_\perp$ jets are reconstructed from parton shower, hadrons, and calorimeter information. The photon energy, E_γ found at the calorimeter level is corrected to E_γ prior to detector simulation, and the event $\not\!\!E_T$ is adjusted.

A $k_\perp$jet momentum correction is derived by applying the MPF method to the Monte Carlo calorimeter information. The jet correction is applied to calorimeter level $k_\perp$jet momentum, P_{kt}^{meas}, and the corrected momentum is compared to the nearest $k_\perp$ jet found at the particle level, P_{kt}^{ptcl}. Closure is obtained when the corrected calorimeter jet momentum agrees with the hadronic jet momentum,

$$\frac{P_{kt}^{meas}}{P_{kt}^{ptcl}} = 1 \ . \tag{9.1}$$

The closure test was performed using cone jets and closure was attained within

errors [45, 46]. As a reference we include comparisons to 0.7 cone jets in our analysis. We attain closure in the central region for $k_\perp$ jets, but we see a small excess in the forward region. We attribute this excess to misclustering of energy in calorimeter jets. We are unable to measure this effect in DØ data, but we can estimate the uncertainty.

9.1 The Data

We use Herwig (version 5.7) Monte Carlo γ-jet data generated with underlying event. Monte Carlo data is generated with γ-jet E_T thresholds of 7, 15, 30, 75, 150, 300, 500 and 700 GeV. It is processed through the SHOWERLIB [48] DØ detector simulation and reconstructed using version 12 of the reconstruction package (RECO v12). Then, we reconstruct $k_\perp$ jets as described in Chapter 5 with the requirement that the transverse momentum, P_T, must be above 4 GeV for samples generated with E_T threshold at 7 GeV and above 8 GeV for the rest of the sample.

9.2 Monte Carlo Jet Corrections

9.2.1 Monte Carlo Underlying Event Offset

The Monte Carlo data does not include the effects of noise, pile-up or multiple interactions, but it does include a Monte Carlo physics underlying event. Therefore, we must subtract an offset only for the Monte Carlo underlying event.

The offset due to physics underlying event for $k_\perp$ jets was seen to be approximately

Underlying Event Densities		
	CC	EC
Calorimeter	0.57	0.57
Hadron	0.53	0.50

Table 9.1: Herwig v5.9 underlying event energy density.

30% larger than it was for cone jets. We estimate the offset for $k_\perp$ jets in Monte Carlo data by multiplying a density by the 0.7 cone area and then scaling up by 30%. The measured energy density due to underlying event was measured in HERWIG v5.9 data generated with and without the underlying event present. These densities were derived by measuring the average difference of energy in ϕ rings in the detector (divided by the area in $\eta - \phi$) with and without the presence of underlying event. The physics underlying event in HERWIG versions 5.7 and 5.9 are the same. The underlying event energy densities are shown in Table 9.1.

9.3 Monte Carlo Jet Response

The jet response is measured as described in the previous chapter except we do not apply the ICR correction, F_η, and we only focus on the central ($|\eta| < 0.7$) and forward ($1.8 < |\eta| < 2.5$) regions.

9.3.1 Monte Carlo Cryostat Factor

First, we determine the cryostat factor, $F_{cry} = R_{jet}^{EC}/R_{jet}^{CC}$, for the Monte Carlo data. Figure 9.1 shows the cryostat factors derived using $k_\perp$ and 0.7 cone jets to define E'. $F_{cryo}^{cone} = 1.039 \pm 0.004$ and $F_{cryo}^{k_\perp} = 1.033 \pm 0.004$ agree within statistical errors.

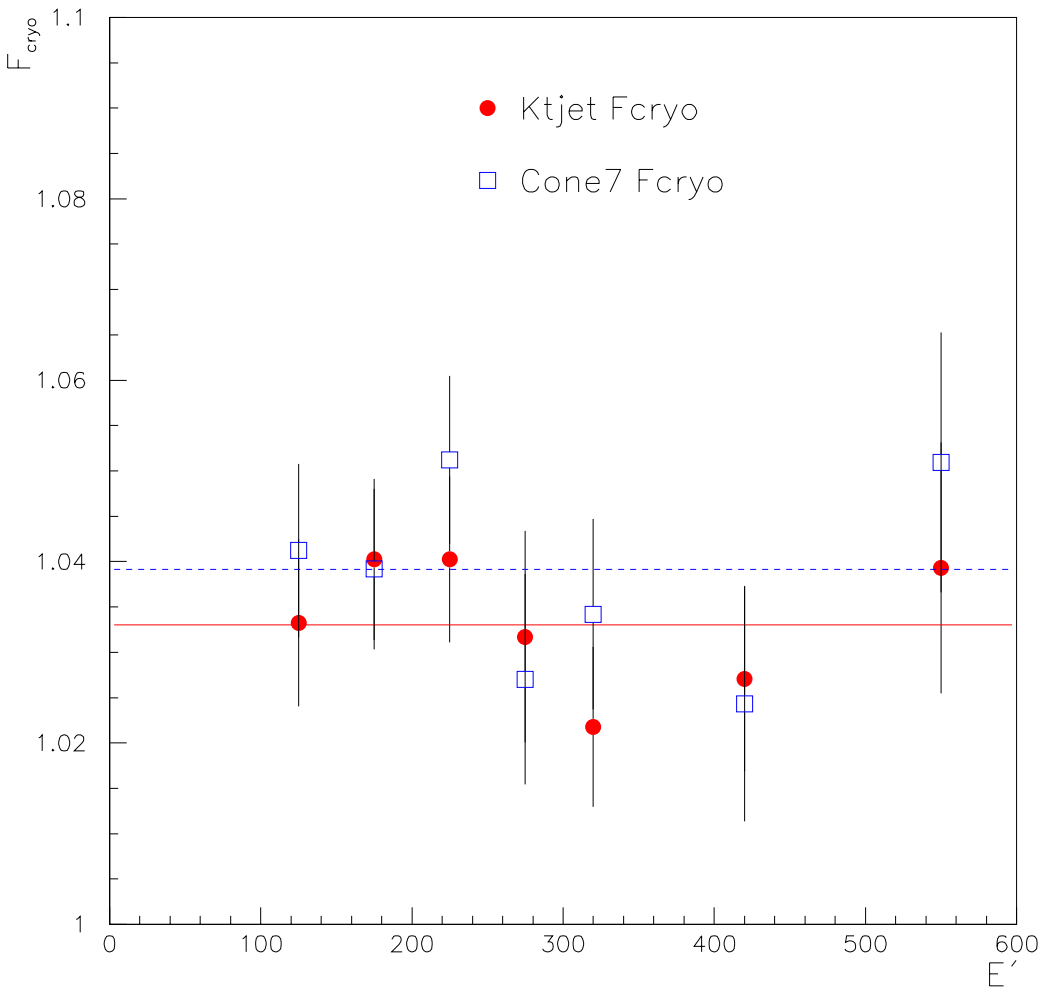

Figure 9.1: Monte Carlo Cryostat Factor. Circles are for $k_\perp$ jets and squares are for cone jets. Solid line is a fit to constant for the $k_\perp$ jet points; dashed line is a fit to constant for the cone jet points. Errors are statistical only.

Algorithm	a	b	c	χ^2/dof
$K_\perp$	0.794 ± 0.013	0.0244 ± 0.0044	-0.0014 ± 0.0004	18.8/16

Table 9.2: Fit parameters for R_{jet} vs. P_{kt} in Monte Carlo data.

9.3.2 Jet Response vs. $k_\perp$ Jet Momentum

The jet response, R_{jet}, is obtained by correcting the EC jets by F_{cryo}, adjusting the event $\not\!\!E_T$ by the change in jet momentum and applying the MPF method described in the previous chapter. The average R_{jet} is measured in bins of E' ranging from 10 to 450 GeV for central jets and 100 to 600 GeV for forward jets. The average $k_\perp$ jet momentum (corrected for the offset and cryostat factor) is also measured in these E' bins. Then, the average R_{jet} values are plotted versus the average P_{kt} values and the functional form,

$$R_{jet}(E) = a + b \cdot ln(E) + c \cdot ln^2(E) \ , \tag{9.2}$$

is fit to this data (Figure 9.2. The results of the fit are shown in Table 9.2.

9.4 Monte Carlo Closure

We apply the corrections described above to $k_\perp$ jets reconstructed from the Monte Carlo calorimeter information. First we subtract the offset from P_{kt} then we divide by the Monte Carlo cryostat factor and R_{jet}. We match the calorimeter (meas) and particle (ptcl) jets to within a distance of 1.0 in $\eta - \phi$ space. Figure 9.3 shows the ratio of the corrected calorimeter jet momentum, P_{kt}^{meas}, to the corresponding

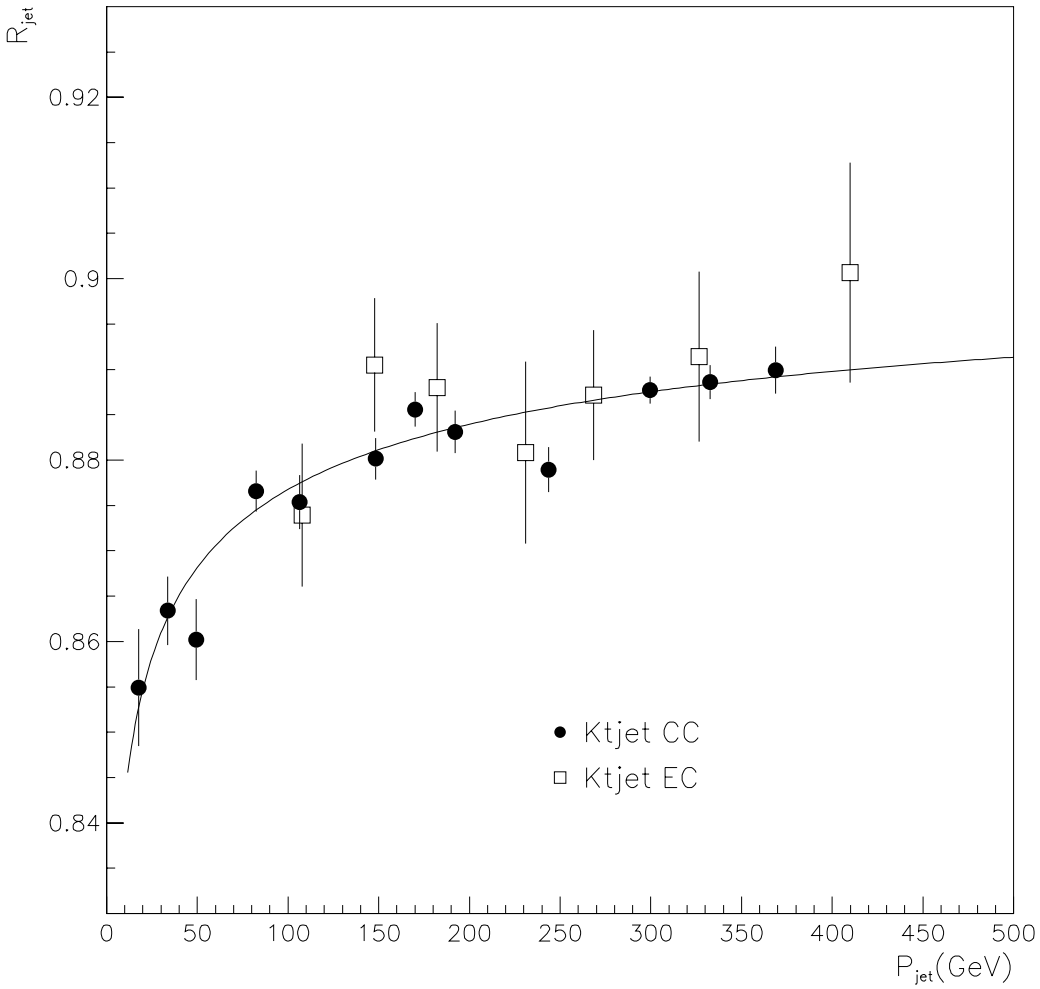

Figure 9.2: R_{jet} vs. P_{kt}in Monte Carlo data. Circles represent CC jets and squares represent EC jets.

particle jet momentum, P_{kt}^{ptcl}, for calorimeter jets in the CC, $|\eta_{meas}| < 0.7$. The average closure is determined by a constant fit and found to be 1.002 ± 0.001

Figure 9.4 shows the ratio of the corrected calorimeter jet momentum, P_{kt}^{meas}, to the corresponding particle jet momentum, P_{kt}^{ptcl}, for calorimeter jets in the EC, $1.8 < |\eta_{meas}| < 2.5$. The average closure is found to be 1.015 ± 0.003. No out of cone showering correction, R_{cone}, was applied to cone jets and this can easily explain the deficiency in Figure 9.4.

It is arguable whether the deviation from unity of the closure ratios (0.2% in the CC and 1.5% in the EC) is significant, and there is no evidence of further excess going farther forward as is shown in Figure 9.5.

The most plausible explanation we have for the small excess in the forward region is that it is due to *misclustering*, energy incorrectly transferred from one jet to another due to calorimeter showering. We have no direct way of determining this effect from data. It is reasonable to expect, however, that misclustering should be a second order effect compared with the *out-of-cone* showering losses observed in the case of cone jets. This is because misclustering would only occur when two or more jets are close to each other and by using vector summed momentum instead of scalar summed energy, the jet P_T contribution from the fraction of the shower at the edge of a jet is greatly reduced.

As a result of this study, we assign an error of 1% in the CC, $|\eta|$ <1.0, increasing linearly to 1.5% at $|\eta|$ >2.0, and then to 5% at η=3.0. Above this the error remains flat at 5% (see Figure 9.6).

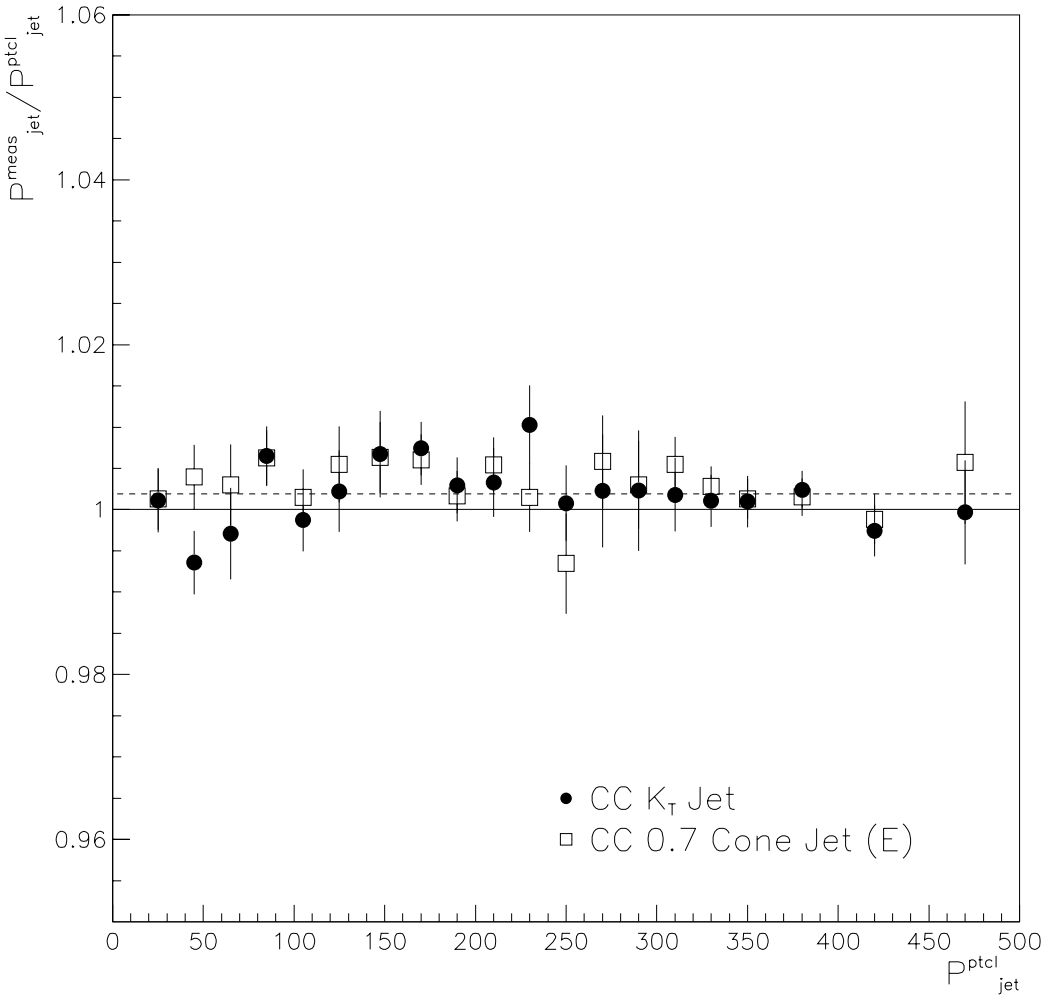

Figure 9.3: Monte Carlo Closure in CC. The ratio of the corrected calorimeter jet momentum to the corresponding particle jet momentum in the central region. Circles are for $k_\perp$ jets and squares are for cone jets. Energy is compared for cone jets. The dashed line is a constant fit to the $k_\perp$ jet closure.

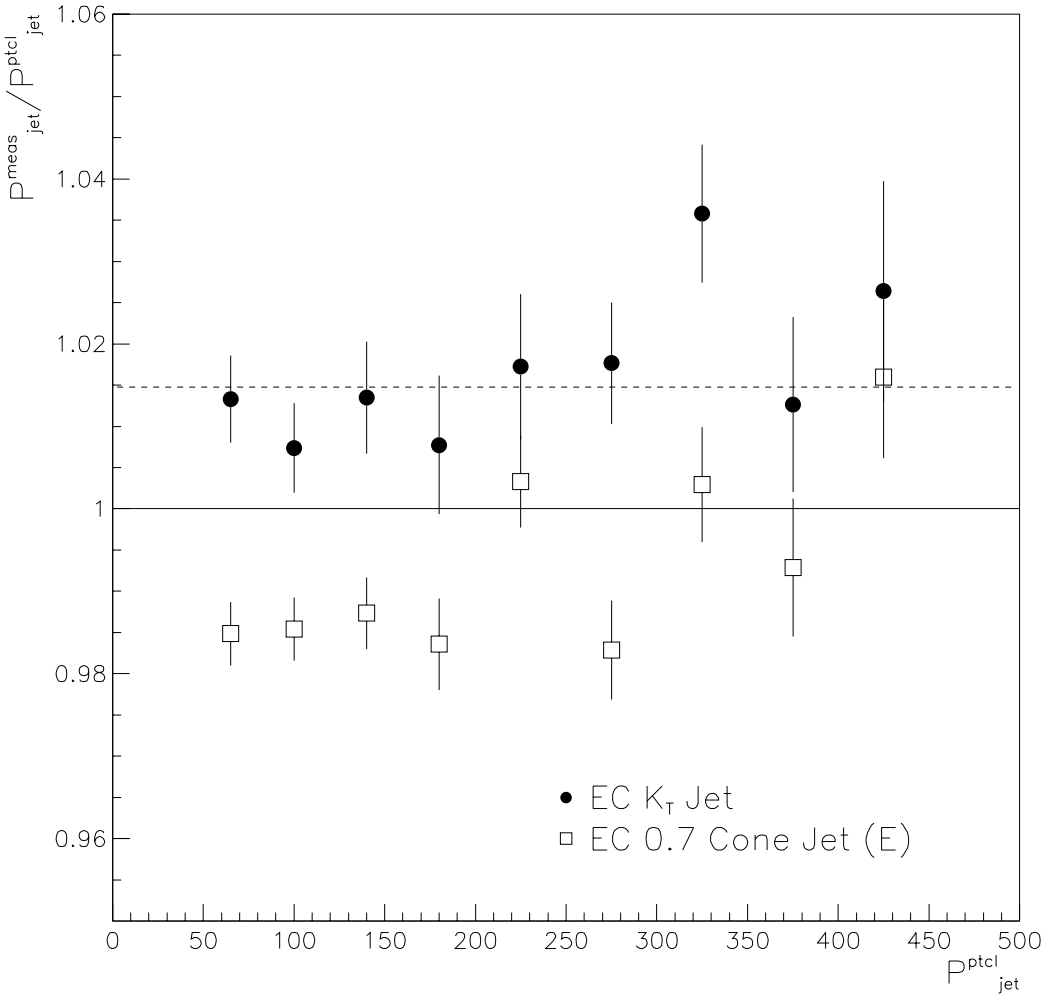

Figure 9.4: Monte Carlo Closure in EC. The ratio of the corrected calorimeter jet energy to the corresponding particle jet energy in the forward region. Circles are for $k_\perp$ jets and squares are for cone jets. The dashed line is a constant fit to the $k_\perp$ jet closure.

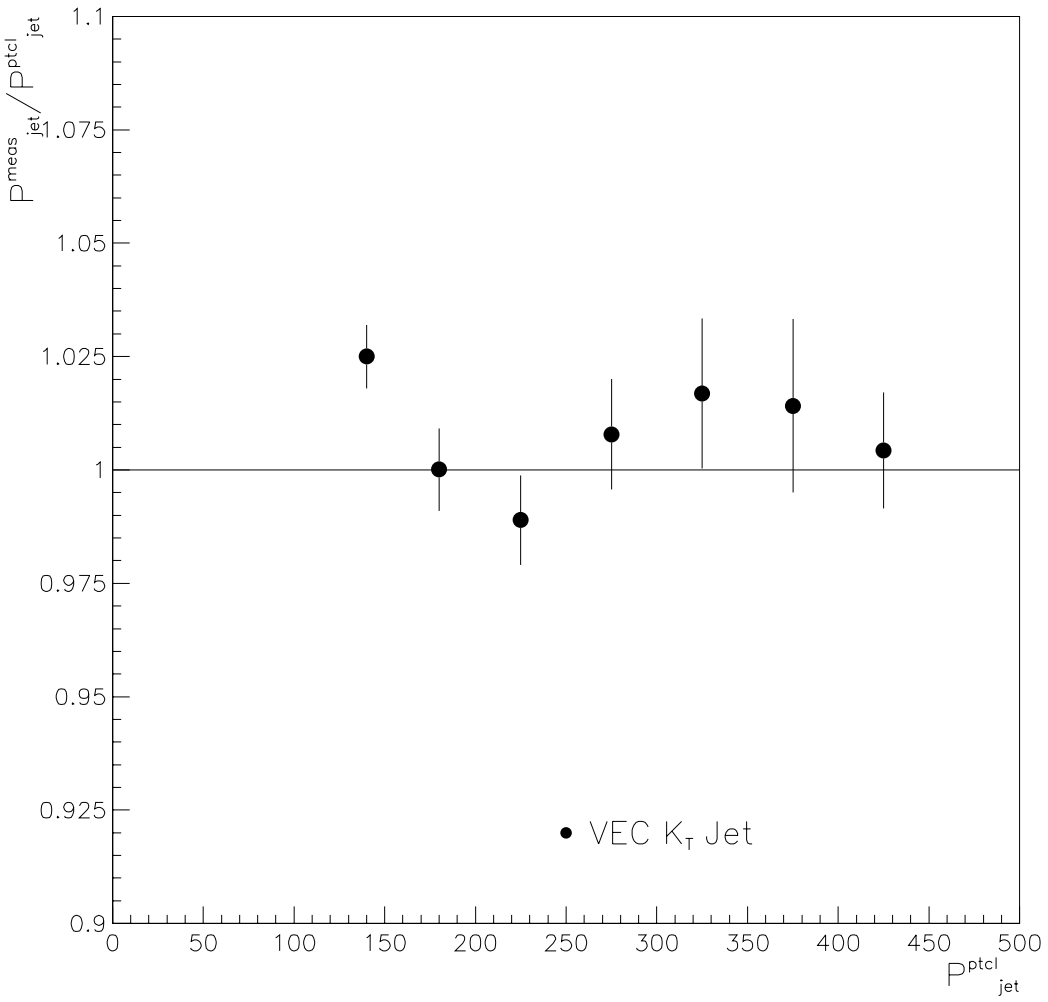

Figure 9.5: Monte Carlo Closure in EC. The ratio of the corrected calorimeter jet energy to the corresponding particle jet energy in the far forward region, VEC, defined by $2.5 < |\eta_{meas}| < 3.5$.

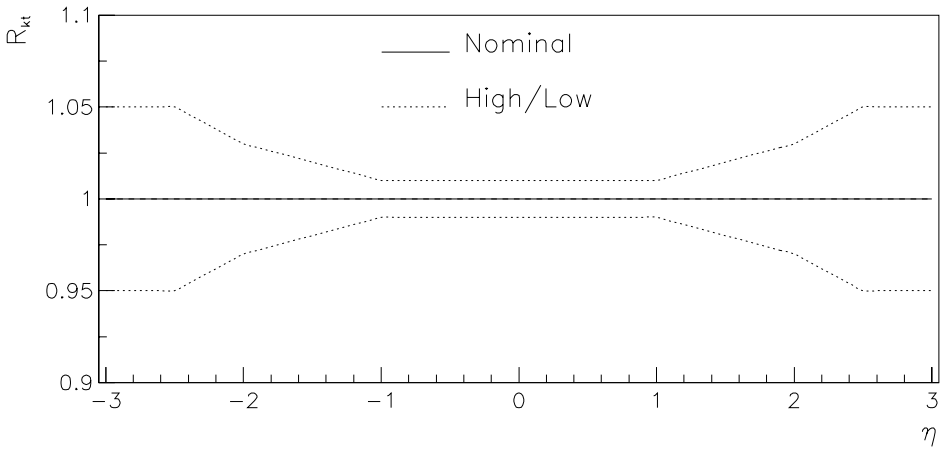

Figure 9.6: $k_\perp$ algorithm dependent correction, R_{kt}. Errors are shown as dotted lines.

Chapter 10

$k_\perp$ Momentum Calibration Summary

To recapitulate, the method for correcting $k_\perp$ jet momentum uses the following relation

$$P_{jet}^{ptcl} = \frac{P_{jet}^{meas} - E_O(\eta, \mathcal{L}, P_T)}{R_{jet}(\eta, P)} \,, \tag{10.1}$$

The calibration is an average correction, integrated over all jet quantities except energy and pseudorapidity. Jets pointing to φ cracks, or with average characteristics different from those in the γ-jet sample, may need a different correction.

The correction is accurate for $k_\perp$ jets with P_T >15 GeV and $|\eta|$ <3. The poor knowledge of the calibration in the range P_T <15 GeV is taken into account with a rapidly increasing error below this threshold.

The calibration is based on Run Ib data taken in $p\bar{p}$ collisions at $\sqrt{s} = 1.8$ TeV.

- **Offset:** the total offset, $E_O(\eta, \mathcal{L})$ has contributions from physics underlying

event, O_{ue} and an offset due to uranium noise and pile-up, O_{zb}. O_{ue} and O_{zb} were derived from a sample of Monte Carlo events with DØ data events overlayed. O_{ue} is parameterized as a function of η. Above $|\eta|$ >1.0, we apply a correction based on the η dependence of the CAFIX5.1 correction but normalized in the central region to our result. O_{zb} is parameterized as a function of η, $\mathcal{L}$, and P_T. For $|\eta|$ >1.0, we apply a correction based on the η dependence of the sample generated at 30< P_T <50 GeVat $\mathcal{L} = 5 \times 10^{30} pb^{-1} sec^{-1}$ but normalized in the central region as a function of $\mathcal{L}$ and P_T.

- **Response (η dependence):** the cryostat factor is adjusted for the DØFIX corrections, F^N_{cry}=0.986±0.006 and F^S_{cry}=0.977±0.006. The ICR η dependent correction was derived using jet-jet data. It is applied to η bins in units of 0.1 and parametrized as a function of P_T in each bin. We assign a 1% error to the correction based on these values and introduce an additional η dependent error that turns on at $|\eta|$ =2.5 and increases linearly up to a 3% at $|\eta|$ =3.

- **Response (energy dependence):** the CAFIX5.1 jet response as a function of E' was taken and multiplied by the DØFIX CC factor of 1.0496 to accommodate this correction in the $k_\perp$ jet data. E' was mapped to $k_\perp$ jet P and the jet response is fit as a function of $k_\perp$ jet P above 30 GeV. Below 35 GeV jet momentum, there is an additional correction to accommodate the deviation from the extrapolated fit. Below 35 GeV jet P_T, there is an additional error to account for the uncertainty in the jet response (see Figure 8.13b).

- **Misclustering:** No correction is applied, but an error is assigned to accommodate misclustering of energy.

- **Monte Carlo:** The correction is derived from a HERWIG sample processed through SHOWERLIB and reconstructed with RECO V12. At present, there is no correction for variations in the ICR region.

10.1 Summary Plots of Corrections and Errors

In this section we provide some summary plots to illustrate the size of the jet corrections and errors as a function of jet P_T and pseudorapidity. For the following plots, luminosity was set to 5×10^{30} cm^{-1}sec^{-1}. Figures 10.1 - 10.3 show the correction and errors as a function of $k_\perp$ jet P_T for 3 different η regions. In the η=1.2 plots, Figure 10.2, the EM, CH, FH, and ICR fractions were taken as averages of values found in DØ jet data. The fluctuations at large energies are due to low statistics in narrow P_T bins. Figures 10.4 and 10.5 show the full correction and errors as a function of η. Here also, the EM, CH, FH, and ICR fractions are taken as averages of values found in data.

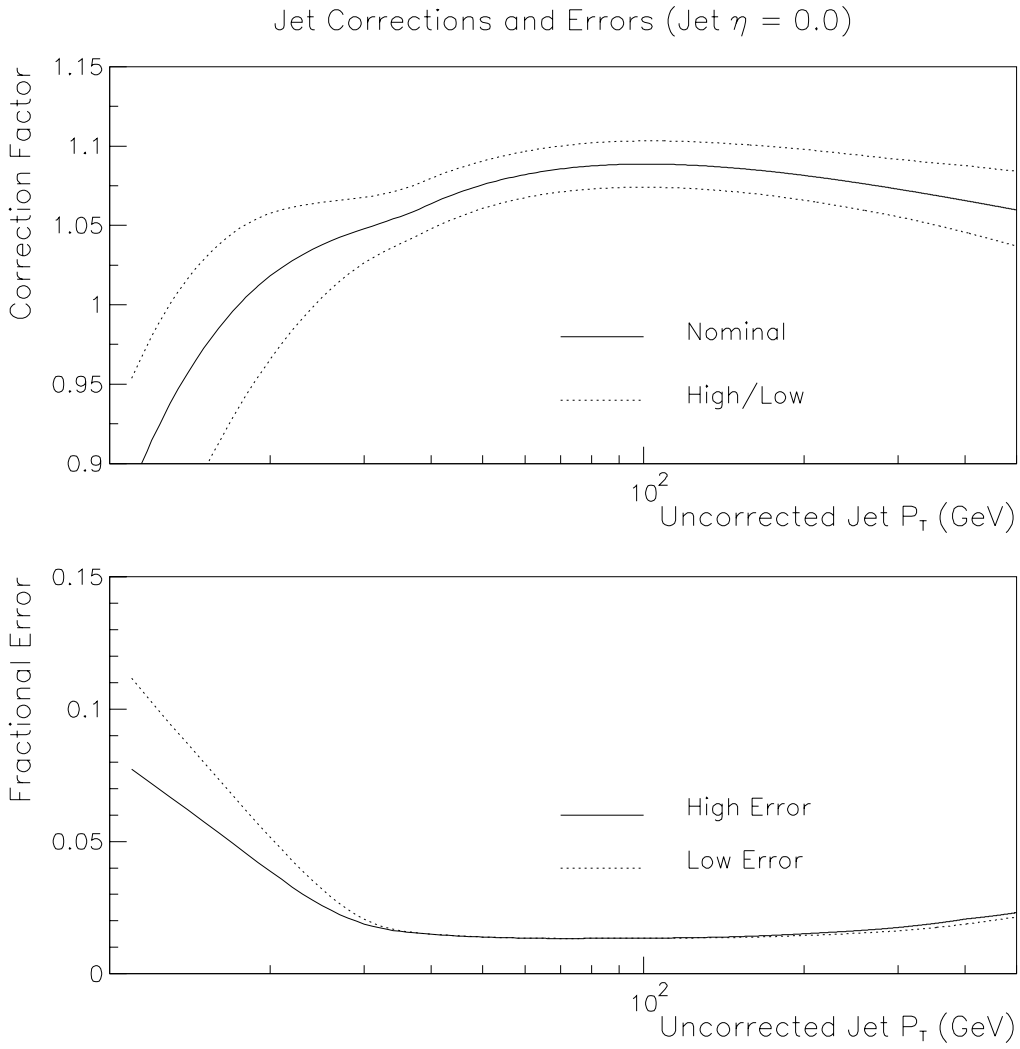

Figure 10.1: Corrections and Errors for η_{Ktjet} =0.0. Top: Nominal, high, and low correction factors. Bottom: high and low fractional errors.

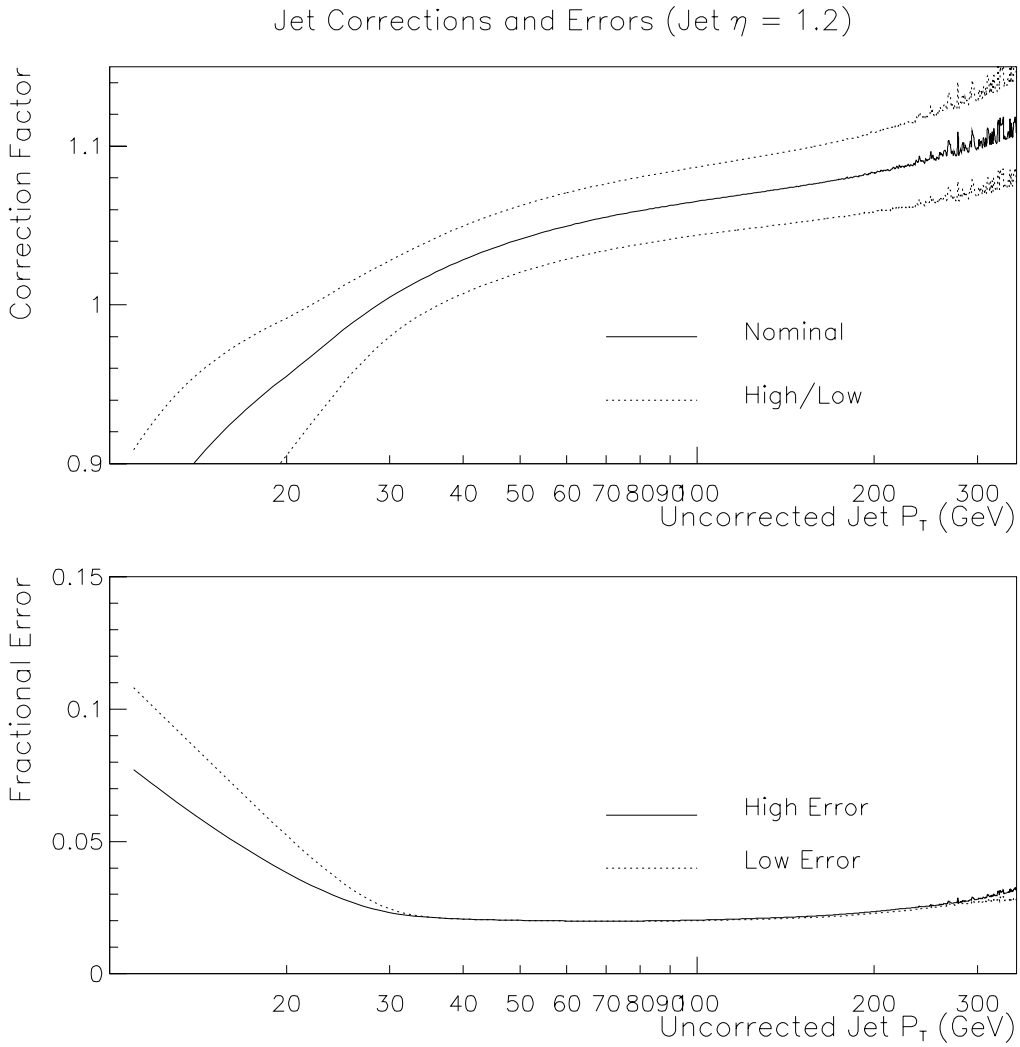

Figure 10.2: Corrections and Errors for η_{Ktjet} =1.2. Top: Nominal, high, and low correction factors. Bottom: high and low fractional errors.

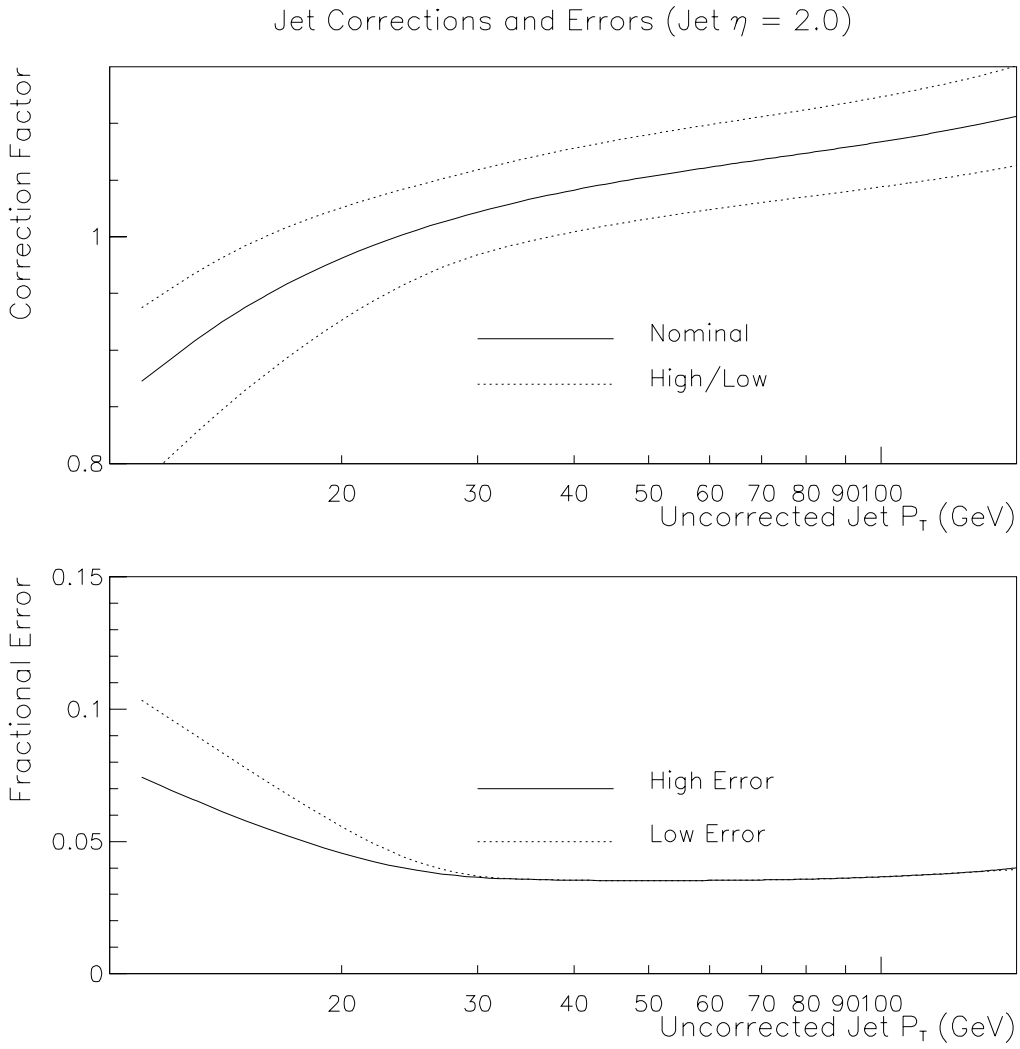

Figure 10.3: Corrections and Errors for η_{Ktjet} =2.0. Top: Nominal, high, and low correction factors. Bottom: high and low fractional errors.

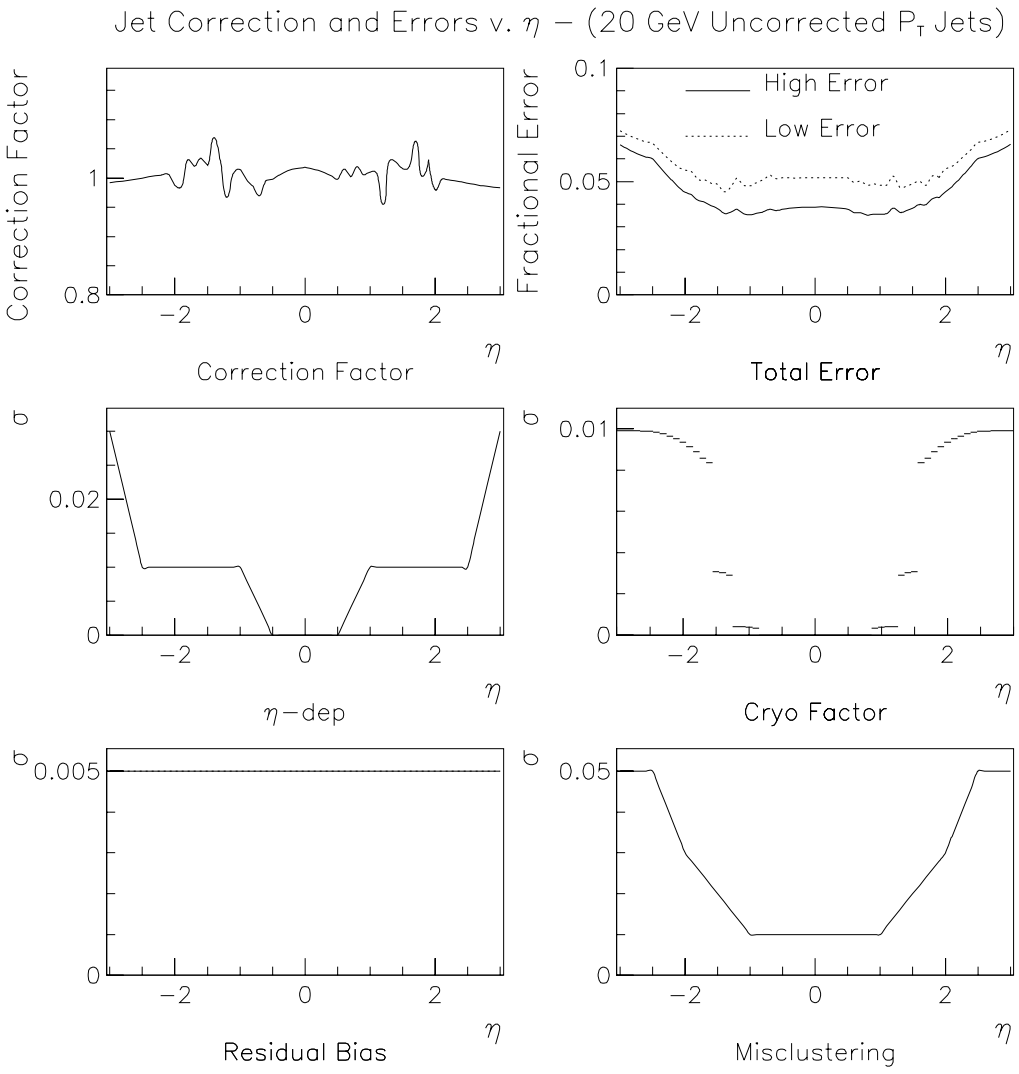

Figure 10.4: Corrections and Errors versus η_{Ktjet}, $k_\perp$ Jet P_T = 20 GeV. The total correction and error are both shown as well as the eta dependence of several individual components of the jet scale error.

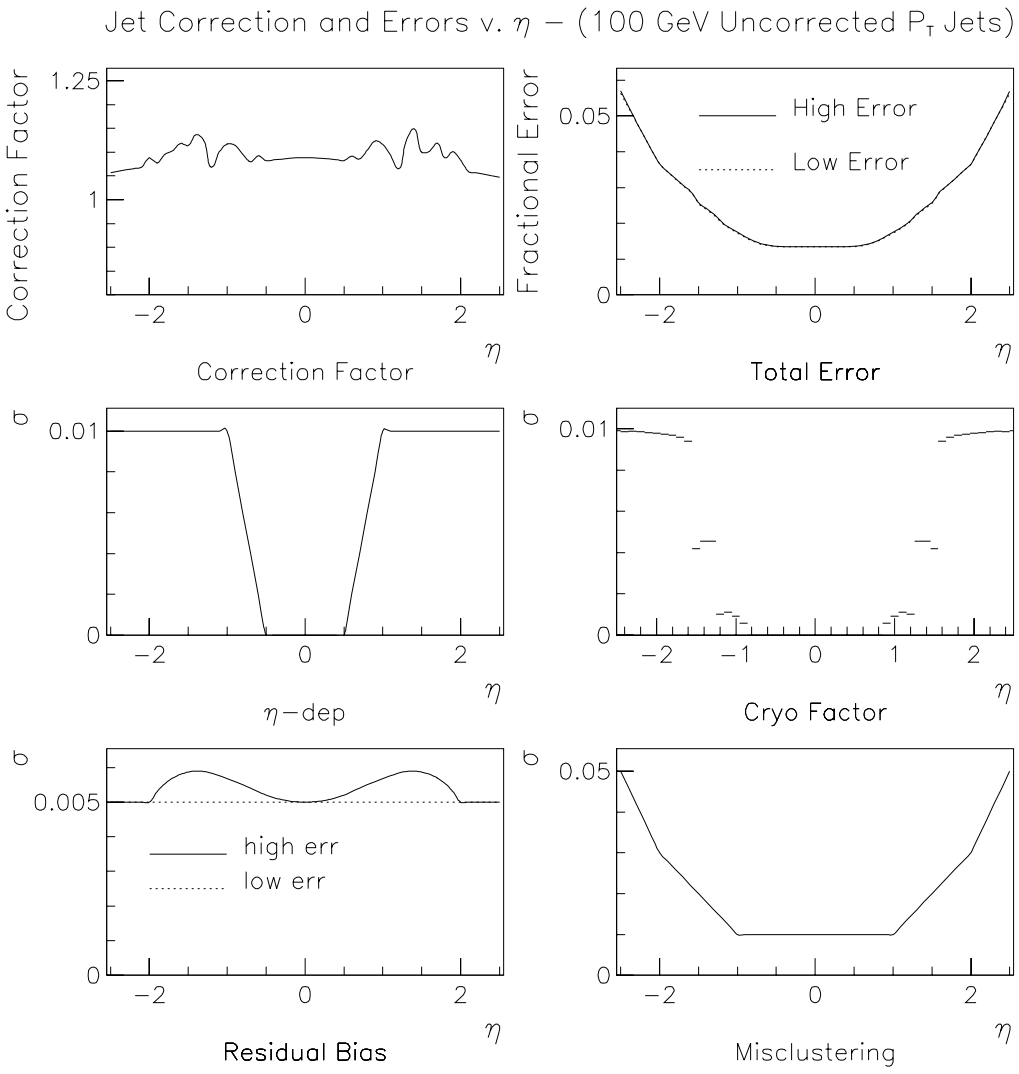

Figure 10.5: Corrections and Errors versus η_{Ktjet}, $k_\perp$ Jet P_T = 100 GeV. The total correction and error are both shown as well as the eta dependence of several individual components of the jet scale error.

Chapter 11

R_{32} Preliminary Results

Now that we have calibrated the $k_\perp$ jet momentum, it is possible to make a very preliminary experimental measurement of R_{32} using the $k_\perp$ jet algorithm. Shown in Figure 11.1 is a measurement of R_{32} as a function of H_{T3} using DØ data. Jets are corrected for the momentum scale, and the errors reflect statistical uncertainty only. H_{T3} is defined as the sum of the P_T of the 3 highest P_T $k_\perp$ jets in an event,

$$H_{T3} = \sum_{i=1}^{3} P_{Ti} \ . \tag{11.1}$$

The number of jets in a given event is equal to the number of $k_\perp$ jets with $P_{Ti} > f_{cut} \times H_{T3}$. R_{32} is measured as the ratio of events with 3 or more jets to events with 2 or more jets,

$$R_{32} = \frac{\sigma^{\geq 3\ jets}}{\sigma^{\geq 2\ jets}} \ . \tag{11.2}$$

Because we choose f_{cut} to avoid cases where only one jet passes the cut, virtually all events have at least 2 jets. So R_{32} can also be thought of as the fraction of events

with 3 or more jets.

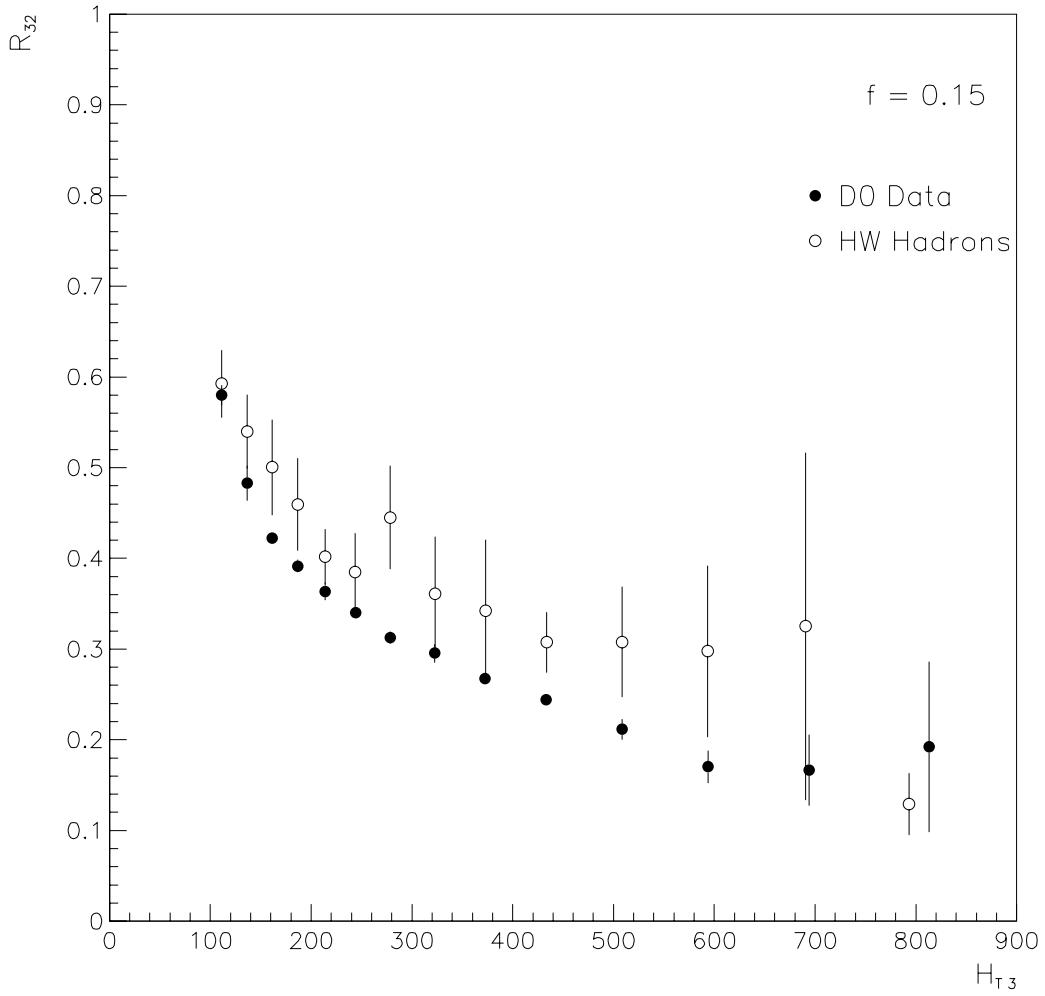

Figure 11.1: R_{32}, vs. H_{T3}. Errors are statistical only. Errors in Monte Carlo Data are the weighted statistical errors.

At this time, we have not made a comparison to an $\mathcal{O}\alpha_s^3$ calculation. For comparison, the R_{32} is measured using Herwig Monte Carlo data (version 5.8) at the hadron level. This is the same sample of events used to determine $f_{cut} = 0.15$ in Chapter 5. The Herwig data are consistently higher than the DØ data. However, no systematic studies (other than the momentum calibration) have been performed on the DØ data. So at this point, it is extremely difficult to draw any conclusions.

Appendix A

Photon and Jet Triggers

A.1 Photon Triggers

The photon triggers we use were designed for direct photon measurements and span the E_T range from 6 GeV through 60 GeV. At Level 1 (the hardware trigger), all photon triggers require at least one calorimeter trigger tower (0.2×0.2 in $\eta \times \phi$) to have E_T above some threshold. The thresholds used for various triggers are shown in Table A.1. When an event passes a level 1 trigger, a list of towers satisfying the level 1 criteria is sent to the Level 2 framework for further analysis.

The Level 2 software triggers have different requirements, but they all share the same algorithm to identify photon candidates [56]. The algorithm begins by identifying the most energetic cell in the 3rd layer of the EM calorimeter in a tower that passed the level 1 threshold. The E_T in the cells within $\Delta\eta \times \Delta\phi = 0.3 \times 0.3$ is summed in the EM and FH1 (1st layer of the fine hadronic calorimeter). To determine whether or not this is a desirable photon candidate, the following criteria

Trigger Name	Level 1 Threshold (GeV)	Level 2 Threshold (GeV)
GAM_6_ISO_GAM	2.5	6.0
GAM_14_ISO_GAM	7.0	14.0
GAM_20_ISO_GAM	7.0	20.0
EM1_GIS	14.0	25.0
EM1_GIS_HIGH	14.0	40.0
EM1_ESC	14.0	60.0

Table A.1: Triggers used in the photon event selection. Additional E_T cuts are applied offline.

are imposed on this cluster:

- The E_T of the candidate cluster must be above the thresholds shown in Table A.1.

- The hadronic energy of the cluster (contained in FH1) must be less than 10% of the total energy.

- The energy deposited in the EM3 layer must be between 10 and 90 percent of the total.

- The shower shape of the cluster in the EM3 layer is required to be consistent with electron shower shapes in test beam data. This is measured by taking the difference between the radial moments in 0.5×0.5 and 0.3×0.3 windows around the axis of the cluster. The difference is required to be below some value which varies as a function of η.

- A cut, f_{iso}, is made to ensure that the photon is isolated from other activity,

$$\frac{E^{r=.4} - E^{cluster}}{E^{cluster}} < f_{iso} \ , \tag{A.1}$$

where $E^{r=.4}$ denotes the energy contained in a cone of radius .4 ($\eta - \phi$ space). $f_{iso} = 15\%$ for all level 2 filters except GAM_6_ISO_GAM where it is set to 30%

A.2 Jet Triggers

The inclusive jet triggers were designed to accept events with 1 or more jets with jet E_T above some threshold. At Level 1 (the hardware trigger), there are two types of jet triggers. One type requires a trigger tower (0.2×0.2 in $\eta \times \phi$) to have E_T above some threshold. The other type requires a *large tile* (0.8×1.6 in $\eta \times \phi$ or 4×8 in trigger towers) to be above some E_T threshold. All of the triggers used in this thesis required the second type (large tiles) except for the JET_MIN trigger which requires a trigger tower. The thresholds used for various triggers are shown in Table A.2. When an event passes a level 1 trigger, a *hot tower* list is sent to the Level 2 framework for further analysis. For JET_MIN, the hot towers are simply all the trigger towers with $E_T > 3$ GeV. For the large tile type triggers, the hot towers are the E_T weighted centers of the large tiles with $E_T > 6$ GeV.

Below is a brief overview of the workings of the level 2 jet finder software package, L2JETS, which identifies jet candidates.

1. L2JETS receives a hot tower list from the Level 1. The hot tower list is a list

Trigger Name	Level 1 Threshold (GeV)	Level 2 Threshold (GeV)
JET_MIN	3.0	20.0
JET_30	15.0	30.0
JET_50	25.0	50.0
JET_85	35.0	85.0
JET_MAX	35.0	115.0

Table A.2: Triggers used in jet event selection. JET_MIN required a trigger tower (versus a large tile) at level 1. Additional E_T cuts are applied offline.

of 'candidate' trigger towers. In run 1b, there were two types of candidates: those from trigger tower ($0.2\eta \times 0.2\phi$) type triggers and those from large tile ($0.8\eta \times 1.6\phi$ or 4×8 trigger towers) type triggers. The trigger tower candidates are simply trigger towers whose total (EM + Hadronic) E_T is greater than some set of 'seed' thresholds The position of a large tile candidate is the trigger tower($0.2\eta \times 0.2\phi$) corresponding to the E_T weighted center of a large tile($0.8\eta \times 1.6\phi$) whose total E_T is greater than the seed threshold. These 'seed' thresholds are not to be confused with the thresholds necessary to pass the level 1 trigger (i.e. JET_30 requires 1 large tile with $E_T > 15$ GeV and the level 2 seed requirement is large tile $E_T > 6$ GeV). The hot tower list is ordered in E_T.

2. The filters are considered in the order in which they appear in the trigger list. For a given level 2 filter, the seed candidates in the hot tower list are considered for this particular filter. A $1.4\eta \times 1.4\phi$ box is drawn around the seed tower and the E_T weighted center of this box will become the level 2 jet center.

3. All calorimeter towers ($.1\eta \times .1\phi$) within .7 of the L2 jet center that are not flagged as used in a previous jet are summed in E_T, EM E_T and the $\eta - \phi$

RMS size is found.

4. If the E_T of the calorimeter tower sum is above the level 2 threshold (see Table A.2), the event passes and all trigger towers and calorimeter towers within .7 of the L2 jet center are flagged as used.

5. Return to step 2. At any point, if the trigger tower considered has been flagged as used, the L2 jet it is associated with is considered. If this L2 jet E_T is above threshold, the event passes.

Appendix B

Cone Jet Offset Comparison

The offsets for the cone algorithm implemented in CAFIX5.1 were derived using density contributions multiplied by the area (in $\eta - \phi$ space) of the cone jets. The densities were measured using the same data samples we overlayed on the Monte Carlo data. We study the offset in cone jets, with the aim of understanding our method, and to cross-check the results against the offset densities of CAFIX5.1. We calculate the densities D_{ue} and D_{zb} as $D = O/1.5$, where 1.5 is the jet area in $\eta - \phi$ space for an $R = 0.7$ cone and O is the offset (O_{ue} or O_{zb}) as measured using the method described in Chapter 7.

Here we will use the same notation as is used for $k_\perp$ jets in Chapter 7, but we will be referring to cone jets reconstructed with $\mathcal{R}$ =0.7 instead of $k_\perp$ jets.

xx 0.7 cone jet E_T in Monte Carlo with no overlay.

$m0$ 0.7 cone jet E_T in Monte Carlo with MB overlay.

zn 0.7 cone jet E_T in Monte Carlo with ZBnoLØ overlay.

zL 0.7 cone jet E_T in Monte Carlo with ZB overlay at luminosity $\mathcal{L} = L \times 10^{30}\text{cm}^{-2}\text{sec}^{-1}$ (e.g. z5 for $\mathcal{L} = 5 \times 10^{30}\text{cm}^{-2}\text{sec}^{-1}$).

B.1 Smeared Versus Unsmeared Quantities

Figure B.1 shows the result for O_{zb} obtained by two different methods:

1. for the two leading jets in sample $z5$ with 30 GeV$<E_T<$50 GeV, we find the corresponding jet in xx and take the E_T difference.

2. same as above but starting with the two leading jets in xx, and then finding the corresponding ones in $z5$.

Although we would like to select our jets by placing cuts on the sample with overlayed noise, $z5$, method (1) is wrong because it artificially selects upwards fluctuations in the offset, which smear jets from the $E_{xx} < 30$ into the $E_{z5} > 30$ region, while rejecting the corresponding downwards fluctuations, from $E_{xx} > 30$ into $E_{z5} < 30$. Method (2) does not suffer from this bias because we cut on xx jets, which are not subject to fluctuations in overlayed noise.

It is not however clear that Method (2) is the one we want. By selecting xx jets with 30 GeV$<E_T<$50 GeV, we are calculating the average additional energy added to a jet generated in this range. We will call it the "unsmeared" offset. On the other hand, by selecting $z5$ jets with 30 GeV$<E_T<$50 GeV, we obtain the average offset for the jets actually found in this energy range. When we take into account the E_T dependence of the spectrum, we realize that this "smeared" offset will be much larger

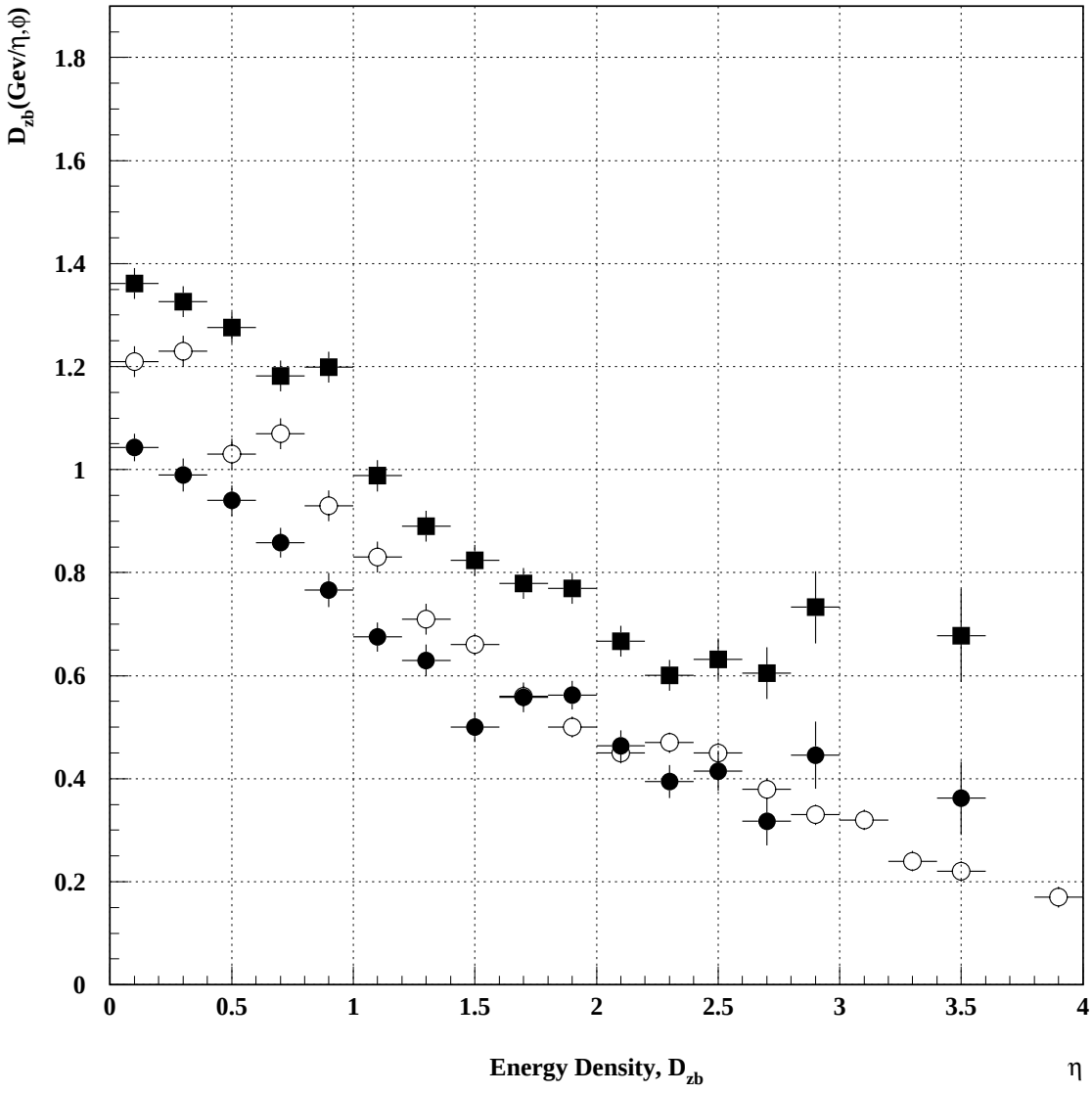

Figure B.1: The 0.7 cone jet offset density, D_{zb}, as obtained by selecting the leading jets either in the $z5$ (full boxes) or in the xx sample (full circles). The open circles are from CAFIX 5.1.

because many more jets are fluctuations with a positive offset from below 30 GeV, than fluctuations with a negative offset from above 50 GeV. A proper representation of the physical E_T spectrum is thus essential.

If we want to calculate offsets by placing cuts on the noise overlayed $z5$ jets, we need to weigh the generated jets to suit our physical needs. Figure 7.4 shows the E_T distribution of the reconstructed $k_\perp$ jets without noise. In order to calculate the "unsmeared" offset, weights have to be chosen so that the distribution of generated jets without noise is flat. The resulting offsets are shown in Figure B.2 together with those calculated using the unbiased Method (2) above, with cuts on the xx jets (and no event weighing). The results are very similar indicating that we understand the effect of weighting, and that a flat distribution of generated jets does yield the unsmeared offsets. This is an important cross-check of the method, before we weigh jets to the physical E_T dependence for the smeared case.

Figure B.3 gives the results for the smeared offset. The procedure is identical to the unsmeared case in Figure B.2, but now we weigh the events to get an ${E_T}^{-5}$ dependence instead of a flat one. The steeply falling ${E_T}^{-5}$ dependence results in the offsets being much higher. For a given smeared, z5, jet E_T there is more contribution from low E_T unsmeared, xx, jets than from high E_T unsmeared jets. Thus, the offset, $O^5_{zb} = z5 - xx$, (and density) will tend to be larger than in the case of a flat E_T distribution.

There remains to be discussed whether smeared or unsmeared offsets should be used as the correction. Note that the approach followed in CAFIX5.1 corresponds to unsmeared offsets, as they are obtained by subtracting energy densities in towers,

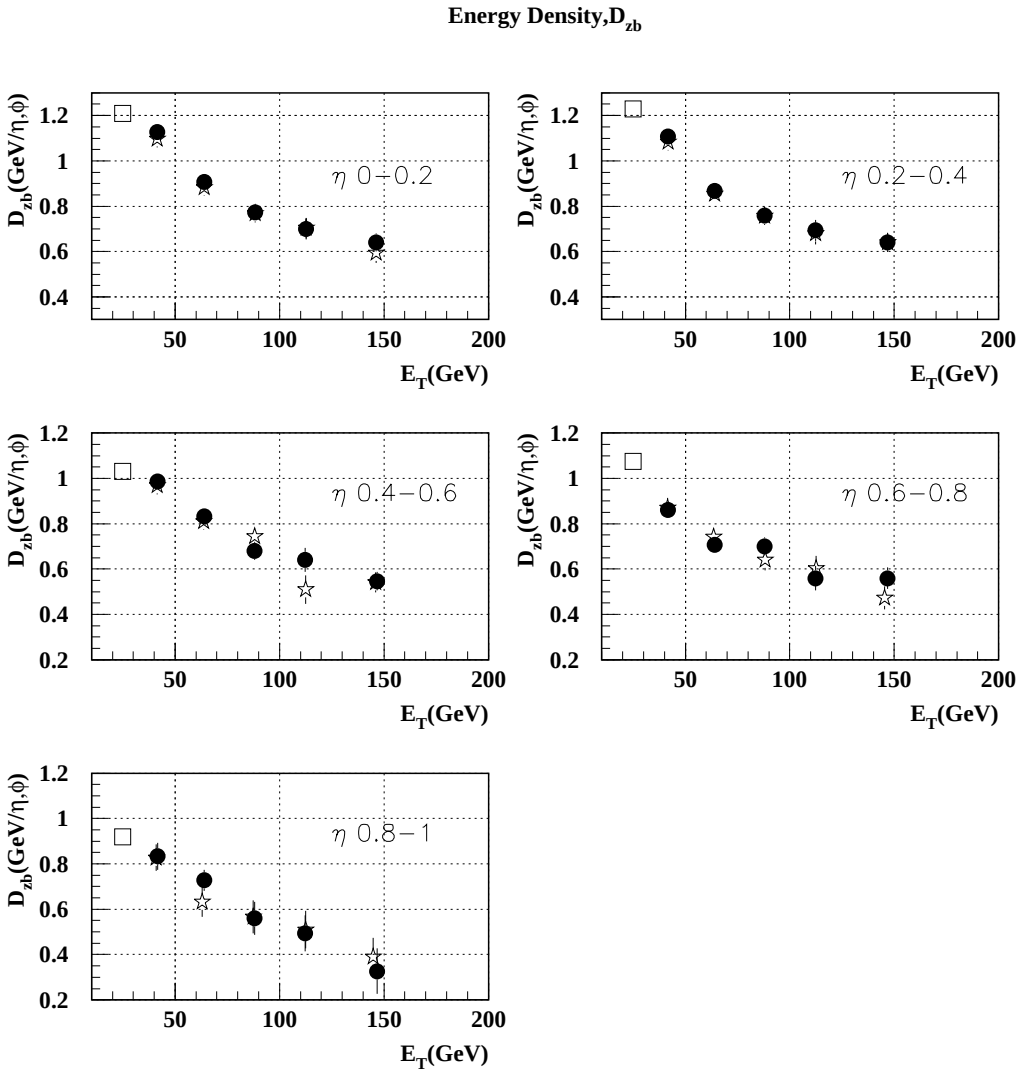

Figure B.2: Unsmeared D_{zb} offset vs. E_T in five η ranges for 0.7 cone jets. The cut in E_T is applied either to the raw xx jets (stars), or to $z5$ jets (full circles) weighed to a flat distribution in E_T . The result from CAFIX5.1 (open box) is shown for comparison on the left, but no E_T is associated with it.

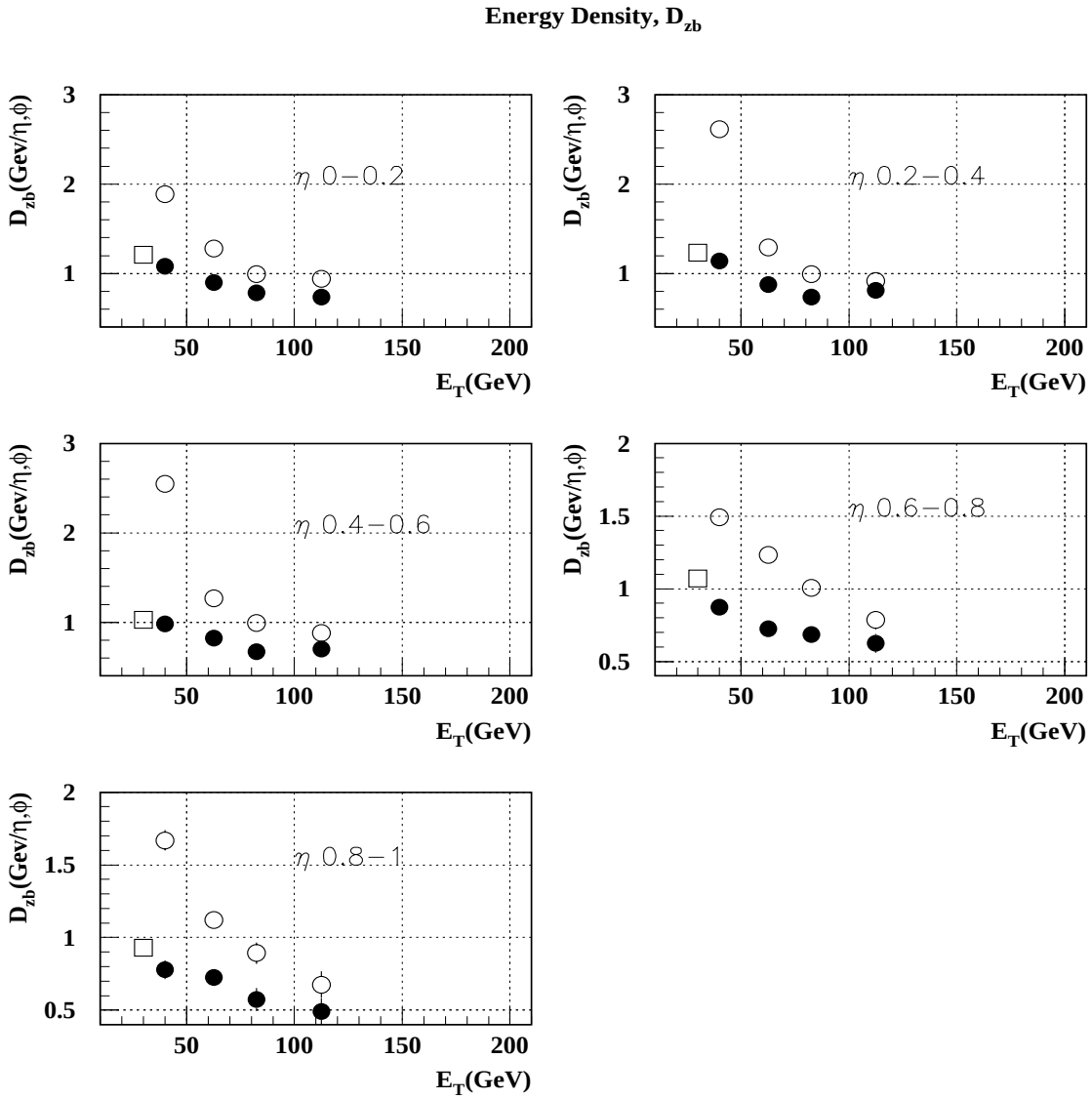

Figure B.3: The smeared (open circles) and unsmeared (full circles) D_{zb} offset for 0.7 cone jets. Both sets of points differ only by the weight assigned to the generated jets. The open box shows for reference the result from the JES D0Note.

without reference to jets. To the extent that the resolution correction is performed at a later stage in physical analyses, we will focus on this note on the unsmeared offset. This method provides an interesting alternative to studying the effect of smearing, and the possibility remains open for further studies with the smeared offset.

For the case of the underlying event, obtained as $O_{ue} = m0 - zn$, we select the two leading jets in xx, find the associated jets in $m0$ and zn, and perform the E_T subtraction, which again corresponds to the unsmeared offset. Then the offset, O_{ue} is divided by the cone jet area, 1.5, to obtain the density, D_{ue}.

B.2 Dependence of the Offset on E_T

We have studied the E_T dependence of D_{zb} and D_{ue} for the unsmeared case, as it allows comparison with the CAFIX5.1 results.

Figure B.4 shows our results for D_{ue} as a function of 0.7 cone jet E_T for several jet η bins in the central region. There appears to be no E_T dependence and the values are consistent with those shown in [45].

Figure B.2 shows our results for D_{zb} ($\mathcal{L} = 5 \times 10^{30}\text{cm}^{-2}\text{sec}^{-1}$) as a function of 0.7 cone jet E_T for several jet η bins in the central region. It is somewhat surprising to see a large drop with E_T for D_{zb}, while not for the underlying event, D_{ue}. This can be explained if the occupancy (the fraction of readout cells in a jet) increases with energy. In this case, the noise contribution goes down because the relative importance of zero suppression diminishes. Fig B.5 shows the occupancy as a function of eta for various E_T bins. This is consistent with occupancies measured

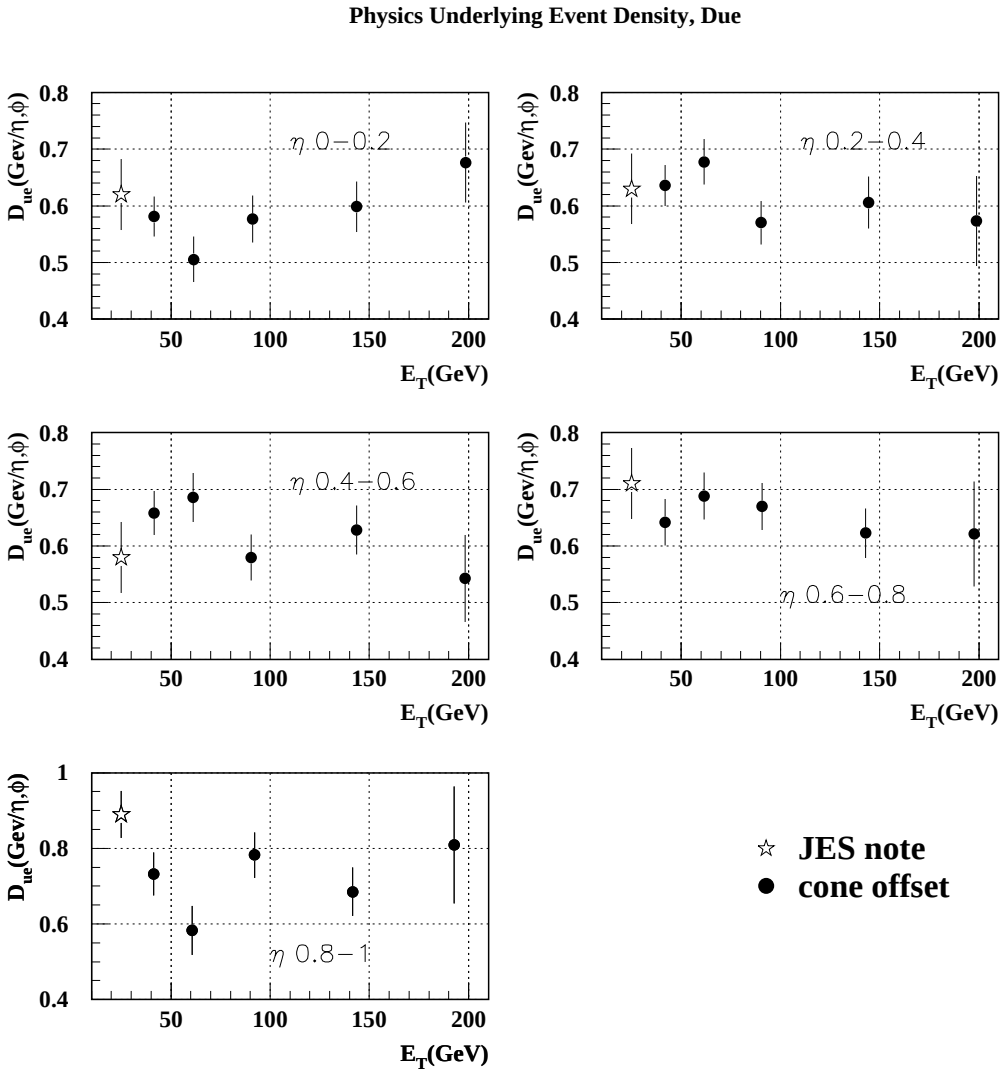

Figure B.4: Dependence of D_{ue} on E_T for cone jets. The result from CAFIX5.1 is shown for reference

in MB data jets (Figure 7.5) and Monte Carlo with MB overlay (Figure 7.6).

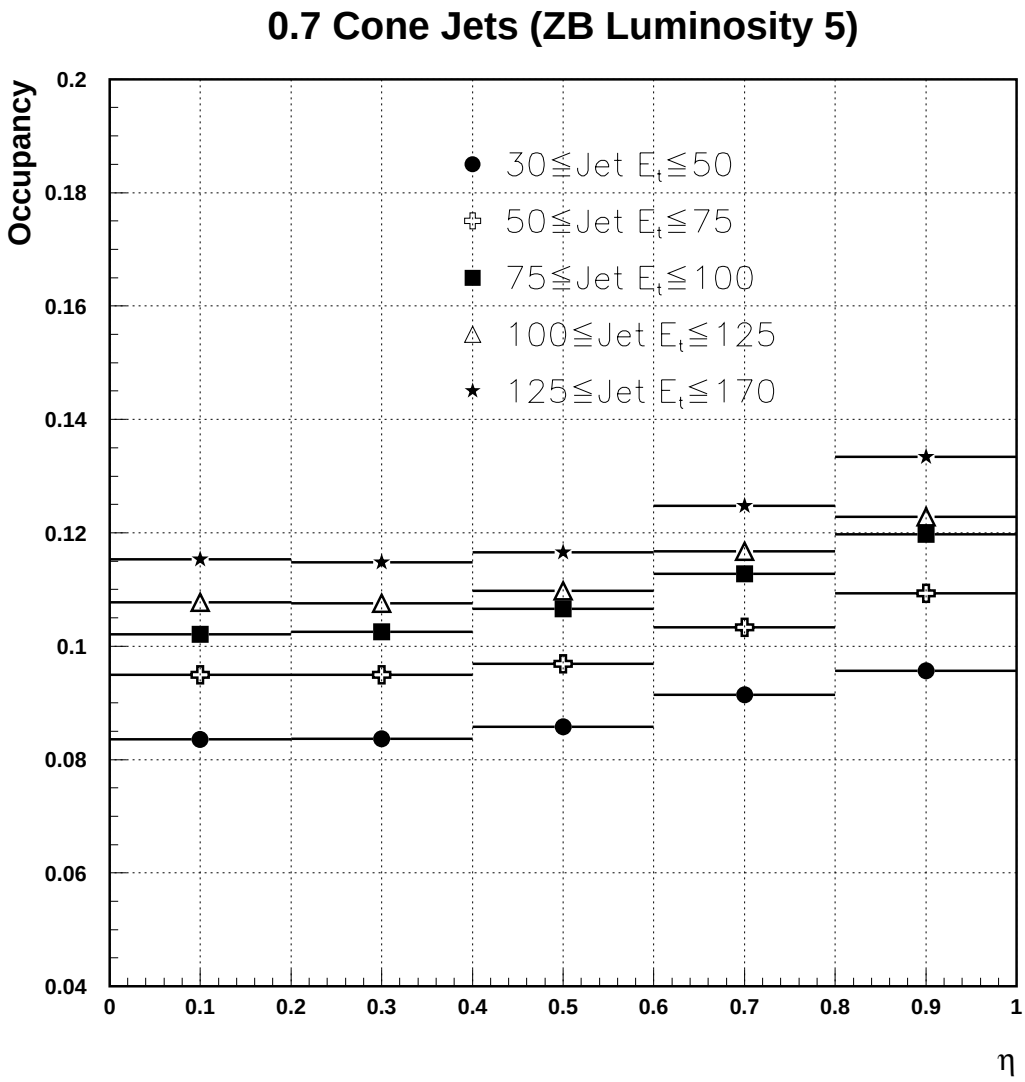

Figure B.5: Jet energy dependence of occupancy for zero bias luminosity 5 and $R = 0.7$ cone jets.

In CAFIX5.1, the E_T density contribution of the zero suppression cut within a jet, δ_{jet}, was related to the density contribution in ZB data, δ_{ZB}, by

$$\delta_{jet} = \delta_{ZB} \frac{F_{ZB}}{F_{jet}}, \tag{B.1}$$

where F_{ZB} and F_{jet} are the corresponding occupancy factors for ZB data and jets

respectively. In CAFIX5.1, the occupancies were assumed to be constant as a function of jet E_T . Figure B.5 shows the occupancy in the central region on a much smaller scale than is shown in [45] and one can see some dependence on E_T . This E_T dependence can only account for 30% of the drop in Figure B.2. The relation in Equation B.1 is empirical and it was checked only for low E_T jets. Although we believe our measurement to be more accurate than the empirical formula, the remaining 70% will be taken as a systematic error to account for the discrepancy.

In CAFIX5.1, the offset is extracted from zbias events and corrected for the occupancy in a jet environment assuming no change in the average energy of an occupied cell. This assumption is probably correct between a zbias event and a low energy jet, but only approximate as the energy of the jet increases.

If there were no zero suppression, one would certainly expect no E_T dependence in the offset for 0.7 cone jets. Because the area in $\eta - \phi$ space is fixed for cone jets, the contribution should be the same regardless of jet E_T . Because zero suppression truncates both positive and negative energies and the noise is not gaussian, it is difficult to assess its effects.

This is not the case for D_{ue}, because the underlying event energy addition is *a*lways positive. Figures B.6 and B.7 show the energy densities for $m0$-xx and zn-xx. Both have noise contribution and do show a drop with E_T . The underlying event contribution, D_{ue} (shown in Figure B.4), is the difference of these two, $m0$-zn, and, therefore, the noise contribution (including zero suppression effects) cancel. Therefore, it is reasonable that D_{ue} is E_T independent.

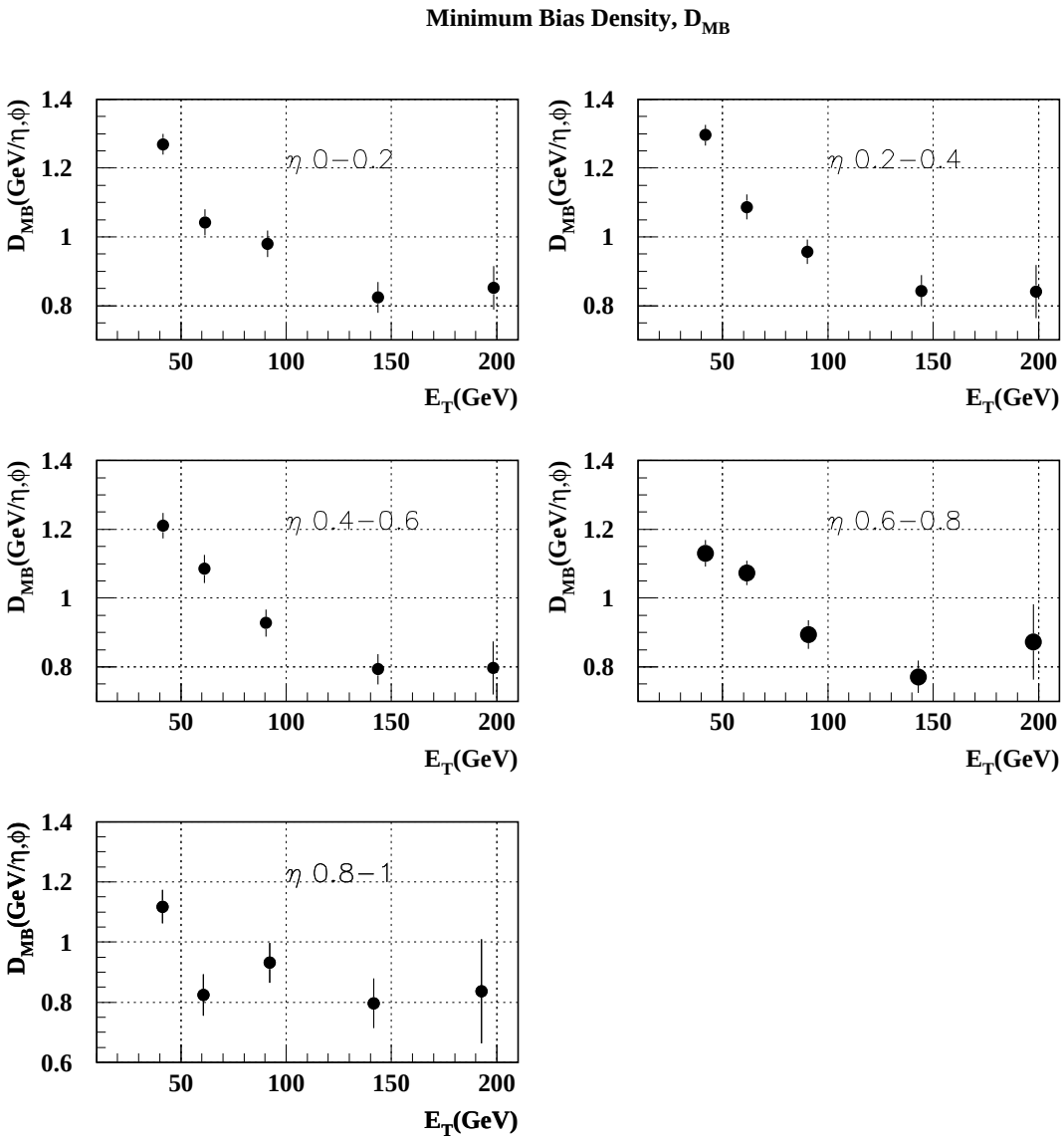

Figure B.6: Dependence of $m0$-xx on E_T for cone jets

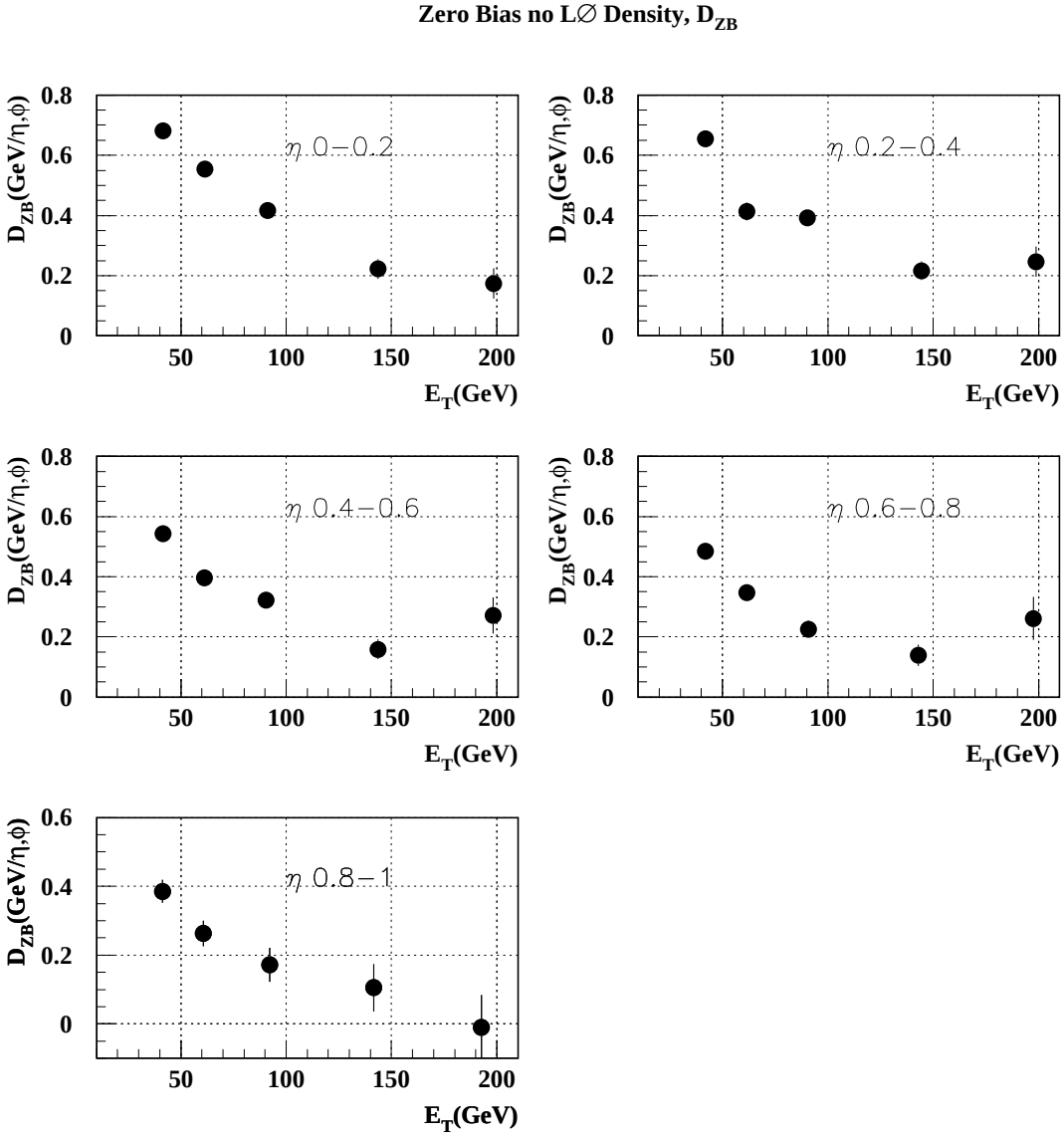

Figure B.7: Dependence of zb-xx on E_T for cone jets. The dependence is the same as in the previous figure, and cancels when getting D_{ue} by taking the difference

B.3 Dependence of the Offset on Luminosity

We have studied the luminosity dependence of the unsmeared offset for 0.7 cone jets due to noise, pile-up and mulitiple interactions. Figure B.8 shows D_{zb} as a function of jet η for several luminosities. We use low E_T jets for this study ($30<E_T<50$) to compare with CAFIX5.1. The agreement between our values and CAFIX5.1 is excellent in this E_T range.

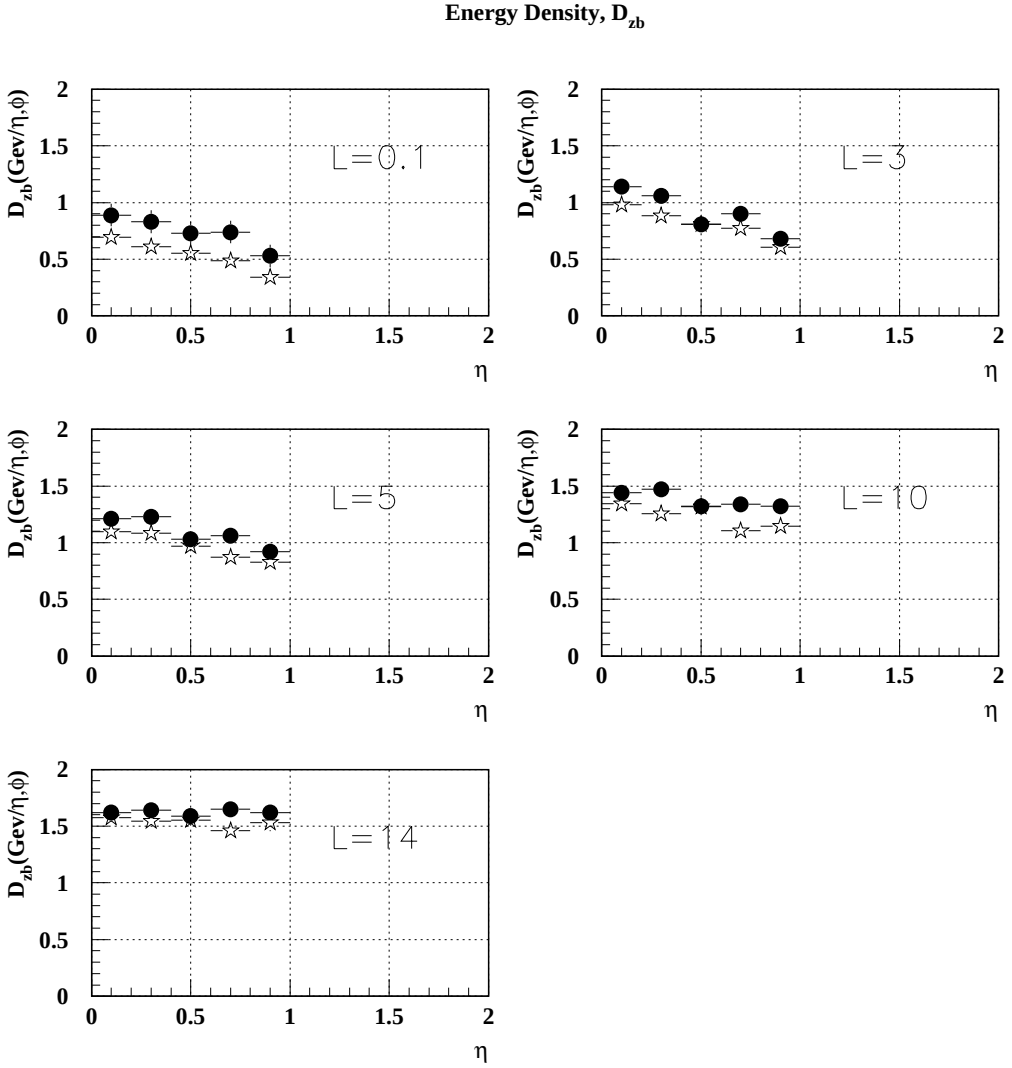

Figure B.8: The unsmeared offset D_{zb} (stars) at different luminosities for $30<E_T<50$ Gev jets (our result depends on jet energy). Full circles are from CAFIX5.1, for comparison.

Appendix C

Showering Effects on the Jet Response

The MPF method uses balance of transverse momentum, P_T, (not energy) to measure the jet response of the detector. Therefore, the correction should be applied to momentum. If there were no showering effects in the calorimeter, the correction for energy and momentum would be identical. However, we can think of at least two mechanisms that make this not so. In either case, the MPF method should give us the correct momentum jet response.

First, a jet of particles (not massless) showers in the calorimeter. The particles in the center of the shower (1 in Figure C.1a) tend to have more energy than the particles around the perimeter of the shower (2 and 3). Particles with higher energy have a better response, and, therefore the particle response is higher in the center than at the edges ($R_1 > R_2, R_3$). Because the response is not uniform over the entire shower and because mpf uses P_T balance (not E_T), we will tend to under correct

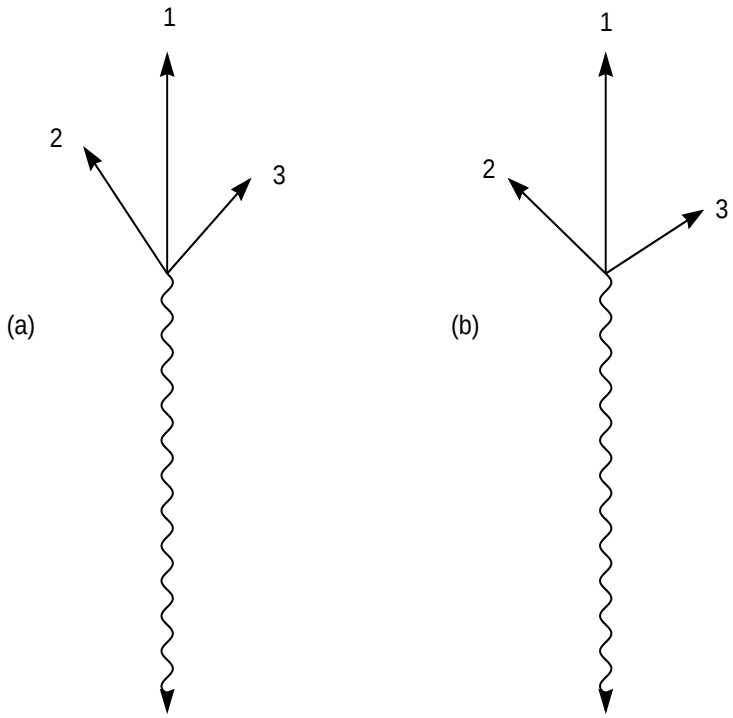

Figure C.1: Showering effects in the MPF method. (a) A photon is balanced by three particles, 1, 2, and 3, in the transverse plane. $E_1 > E_2, E_3$ and $R_1 > R_2, R_3$. (b) The 2nd and 3rd particles are deflected away from the jet axis in the calorimeter.

Energy using the MPF method. If the response were uniform over the shower, the energy and momentum correction would be identical. This leads to undercorrection when correcting energy using MPF. But the momentum is correctly corrected.

To illustrate this, Figure C.1a depicts a simple event where a photon is balanced by a jet of 3 particles in the transverse plane. Particle 1 lies along the jet axis which is back to back with the photon. Let us assume the 3 particles are massless (i.e. $E = P$) and the event takes place in the transverse plane (i.e. $E_T = E$). Then, the particle jet's energy can be written as

$$E_{ptcl} = E_1 + E_2 + E_3 \ , \tag{C.1}$$

and the momentum is given by

$$P_{ptcl} = E_\gamma = E_1 + E_2 cos\theta_{12} + E_3 cos\theta_{13} \ . \tag{C.2}$$

Given particle responses of $R_1 > R_2, R_3$, the measured jet quantities are given by

$$E_{meas} = R_1 E_1 + R_2 E_2 + R_3 E_3 \tag{C.3}$$

and

$$P_{meas} = R_1 E_1 + R_2 E_2 cos\theta_{12} + R_3 E_3 cos\theta_{13} \ . \tag{C.4}$$

The ratio of measured to particle jet quantities is the true energy/momentum response for the jet. If the particle response is uniform over the jet, $R = R_1 = R_2 = R_3$, the energy and momentum jet response would be identical, R.

The MPF jet response is given by

$$R_{mpf} = 1 + MPF \quad where \quad MPF = \frac{\vec{\not{E}}_T \cdot \hat{n}_\gamma}{E_{T\gamma}} \ . \tag{C.5}$$

Substituting for the event $\vec{\not{E}}_T$,

$$\vec{\not{E}}_T = -\left(R_1\vec{P}_1 + R_2\vec{P}_2 + R_3\vec{P}_3 + \vec{P}_\gamma\right) \ , \tag{C.6}$$

yields

$$\begin{aligned} R_{mpf} &= \frac{R_1E_1 + R_2E_2cos\theta_{12} + R_3E_3cos\theta_{13}}{E_\gamma} \\ R_{mpf} &= R_P = \frac{P_{meas}}{P_{ptcl}} \ . \end{aligned} \tag{C.7}$$

The jet response derived using the MPF method is identical to the true momentum jet response.

For the energy jet response, let us assume particles 2 and 3 have equal response, $R_2 = R_3 = R$ and $R_1 = R + \epsilon$. Then the energy and momentum jet response will be

$$\begin{aligned} R_E &= \frac{\epsilon E_1}{E_{ptcl}} + R \\ and \quad R_P &= \frac{\epsilon E_1}{P_{ptcl}} + R \end{aligned} \tag{C.8}$$

Since $E_{ptcl} > P_{ptcl}$, the energy jet response will be less than the momentum jet response ($R_E < R_P = R_{mpf}$). Thus, jets will be undercorrected in energy using R_{mpf}.

The second mechanism which would make the energy jet response unequal to the

momentum jet response occurs when particles get deflected in the detector and the detector absorbs the recoil such that the recoil is not measured in the calorimeter. The net result is a wider jet at the calorimeter level than at the particle level. This is essentially the mechanism described in [55]. This means that the measured $E_{meas} - P_{meas}$ is greater than the true $E_{ptcl} - P_{ptcl}$. Therefore, the energy of the jet needs less correction than the momentum. Since the MPF method measures the momentum jet response, the energy will be over corrected using MPF method. But again, the momentum is correctly corrected.

Figure C.1b shows an example of this where a photon is balanced by 3 showered particles in the transverse plane. The true E and P are the same as above (Equations C.1 and C.2. The measured E is also the same (Equation C.3). In this scenario, the angles between 1 and 2, and 1 and 3, θ_{13}, are larger than in the previous example ($\theta_{12}^{meas} > \theta_{12}^{true}$ and $\theta_{13}^{meas} > \theta_{13}^{true}$). Therefore, the measured P will be less than it was in the previous example.

A similar exercise will also show that $R_{mpf} = R_P$ and that $R_E > R_P$. In this case, jets will be overcorrected in energy using R_{mpf}. And again, R_{mpf} gives us the correct jet momentum response.

Both these showering effects come into play with cone jets because they use scalar sum Et. Because we use vector sum momentum for kt jets, we should not be affected by these biases. We do use Snowmass recombination in the preclustering, however, so there may be a small effect. This is discussed in section 9.4.

References

[1] V. Weisskopf, *Physics in the Twentieth Century: Selected Essays*, MIT Press, (1972).

[2] http://pdg.lbl.gov/cpep/history/quantumt.html (1999).

[3] http://pdg.lbl.gov/cpep/history/smtt.html (1999).

[4] A. Einstein, *Annalen Phys.***17** 891 (1905).

[5] R. A. Millikan, *Phys. Rev.***7** 18 (1916).

[6] M. Gell-Mann, *Phys. Lett.* **8**, 214 (1964).

[7] G. Zweig, CERN Report 8419/Th 412 (1964).

[8] Aubert *et al.*, *Phys. Rev. Lett.* **33** 1404 (1974).

[9] Augustine *et al.*, *Phys. Rev. Lett.***33** 1406 (1974).

[10] S. Abachi *et al.*, *Phys. Rev. Lett.* **74** 2632 (1995).

[11] C. Cowan and F. Reines, *Phys. Rev.* **39** 273 (1959).

[12] C. Anderson and S. Neddermeyer, *Phys. Rev.* **51** 884 (1937).

[13] Perl *et al.*, *Phys. Rev. Lett.* **35** 1489 (1975).

[14] Danby *et al.*, *Phys. Rev. Lett.* **9** 36 (1962).

[15] Particle Data Group, C. Caso *et al.*, *Euro. Phys. Jour.* **C3** (1998).

[16] D. Griffiths, *Introduction to Elementary Particles*, John Wiley and Sons, (1987).

[17] P. Renton, *Electroweak Interactions*, Cambridge University Press, (1990).

[18] M. Kaku, *Quantum Field Theory*, Oxford University Press, Inc., (1993).

[19] D. Barger, J. N. Phillips, *Collider Physics*, Addison-Wesley Publishing Company, Inc., (1987, 1997).

[20] R. Ellis, W. Stirling, B. Webber, *QCD and Collider Physics*, Cambridge University Press (1996).

[21] R. Brock *et al.*, *Rev. Mod. Phys.* **67** 157 (1995).

[22] Buras, A. J., *Rev. Mod. Phys.* **52**, 199 (1980).

[23] W. Giele, E. Glover, and D. Kosower, *Phys. Rev. Lett.* **73**, 2019 (1994).

[24] G. Marchesini *et al.*, *Comput. Phys. Commun.* **67**, 465 (1992).

[25] G. Marchesini *et al.*, hep-ph/9607393 (1996).

[26] D. Buskulie *et al.*, *Phys. Lett.***B307** 209 (1993).

[27] J. Thompson, *Introduction to Colliding Beams at Fermilab*, FERMILAB-TM-1909 (1994).

[28] S. Abachi *et al.*, *Nucl. Instr. and Meth.* **A338** 185 (1994).

[29] Detoeuf *et al.*, *Nucl. Instr. and Meth.* **A279** 310 (1989).

[30] D. Pizzuto, Ph.D. Thesis, SUNY Stony Brook (unpublished) (1989).

[31] S. Rajagopalan, Ph.D. Thesis, Northwestern University (unpublished) (1992).

[32] J. Bantly *et al.*, DØ internal note 1996 (unpublished) (1993).

[33] M. Abolins *et al.*, *Nucl. Instr. and Meth.* **A289** 543 (1990).

[34] J. Linnemann *et al.*, *Proceedings of DPF'92* 1641 (1993).

[35] S. Abachi *et al.*, *Nucl. Instr. and Meth.* **A324** 53 (1993).

[36] N. Hadley, *Cone Algorithm for Jet Finding*, DØ Internal Note #904.

[37] W. Bartel *et al.*, *Zeit. Phys.***C33** 23 (1986).

[38] S. Bethke *et al.*, *Phys. Lett.***213B** 235 (1988).

[39] S. Catani *et al.*, *Phys. Lett.* **B269** 432 (1991).

[40] S. Catani *et al.*, *Nucl. Phys.* **B406** 187 (1993).

[41] S. Ellis, D. Soper, *Phys. Rev.*, **D48** 3160 (1993).

[42] B. Abbott, G. Watts, *The KTCL Bank* DØ Internal Note #3006 (1996).

[43] R. Astur *et al.*, *QCD Physics With The $k_\perp$ Jet Algorithm* DØ Internal Note #2163 (1994).

[44] C.-P. Yuan, M. Seymour, independent private communication.

[45] B. Abbott *et al.*, *Jet Energy Scale at DØ* DØ Internal Note #3287 (1997).

[46] B. Abbott *et al.*, *Nucl. Instr. and Meth.***A424** 352 (1999).

[47] A. Goussiou, J. Krane, *Jet Energy Scale at DØ for* $\sqrt{s}$ *= 630 GeV* DØ Internal Note #3288 (1997).

[48] A. Jonckheere, J. Womersley, R. Raja, *Shower Libraries for DØ GEANT Monte Carlo* DØ Internal Note #650 (1987).

[49] K. Frame *et al.*, *Trigger Efficiencies for Run 1B Inclusive Jet Triggers* DØ Internal Note # 3178 (1996).

[50] K. Frame *et al.*, *Features and Bug of L2JETS and ESUM Bank* DØ Internal Note # 3165 (1996).

[51] G. Diloreto, Ph.D. Thesis, Michigan State University (unpublished) (1998).

[52] R. Snihur, DØ Internal Communication DØNews #6166 (1998).

[53] D. Chakraborty, DØ Internal Communication DØNews #3750 (1995).

[54] F. James, *MINUIT Function Minimization and Error Analysis* CERN Program Library Long Writeup, Version 94.1 (1994).

[55] A. Goussiou, *New Showering Correction For the Jet Energy Scale at DØ*, DØ Internal Note #3606 (1998).

[56] J. McKinley, J. Linnemann, *Description of the Level 2 Electromagnetic Filter Algorithm and Study of the Effects of Shower Generation Method, Zero Suppression, and Event Generation Method on the Level 2 Electromagnetic Filter for DØ*, DØ Internal Note #1354 (1992).

[57] S. Fahey, Ph.D. Thesis, Michigan State University (unpublished) (1995).

[58] S. Jerger, Ph.D. Thesis, Michigan State University (unpublished) (1997).

[59] E. Flattum, Ph.D. Thesis, Michigan State University (unpublished) (1996).

[60] K. Hahn, Ph.D. Thesis, University of Rochester (unpublished) (1998).